

CHARACTERISATION OF THE HAIB PORPHYRY COPPER DEPOSIT, SOUTHERN NAMIBIA, USING HYPERSPECTRAL AND RADIOMETRIC DATASETS

ADEPARIOYE, PHILLIP ADEGBOYEGA
March, 2016

SUPERVISORS:
Dr. F. J. A. van Ruitenbeek
Prof. dr. F. D. van der Meer



CHARACTERISATION OF THE HAIB PORPHYRY COPPER DEPOSIT, SOUTHERN NAMIBIA, USING HYPERSENSPECTRAL AND RADIOMETRIC DATASETS

ADEPARIOYE, PHILLIP ADEGBOYEGA
Enschede, The Netherlands, March, 2016

Thesis submitted to the Faculty of Geo-Information Science and Earth Observation of the University of Twente in partial fulfilment of the requirements for the degree of Master of Science in Geo-information Science and Earth Observation.

Specialization: Applied Earth Sciences – Earth Resources Exploration

SUPERVISORS:

Dr. F. J. A. van Ruitenbeek
Prof. dr. F. D. van der Meer

THESIS ASSESSMENT BOARD:

Dr. M. van der Meijde (Chair)
Dr. F. Kuehn (External Examiner, Federal Institute for Geosciences and Natural Resources, BGR, Germany)

DISCLAIMER

This document describes work undertaken as part of a programme of study at the Faculty of Geo-Information Science and Earth Observation of the University of Twente. All views and opinions expressed therein remain the sole responsibility of the author, and do not necessarily represent those of the Faculty.

ABSTRACT

The challenge of using potassic alteration to understand the configuration of the Proterozoic porphyry copper deposit of the Haib is as a result of the pervasive potassium concentration in the different lithological units. This is further compounded by the mineral assemblages associated with the potassic alteration zone not having an easily recognisable absorption features in the SWIR region of the electromagnetic spectrum. This research attempts to study the alteration systems associated with the Haib porphyry copper deposit and carry out a characterisation using the hyperspectral and radiometric datasets. The evidence of diverse compositional variation is so pronounced in all the detected endmembers. This was demonstrated by the shift in the wavelength positions of the deepest absorption features diagnostic of these alteration minerals. The study area is characterised by two different categories of illite minerals based on their crystallinity, the illite I and the illite II; the illite I exhibits high crystallinity as its AlOH feature near 2200nm displays significant sharpness while the H₂O feature near 1900nm becomes shallow; the illite II is classified as the low crystallinity type forming four (4) classes of variably mixed minerals: the Illite-Carbonate-Smectite (ICS), Illite-Smectite (IS), Illite-Smectite-Carbonate (ISC) and the Illite tending to Phengite (ItP). The incorporation and significance of the water feature at 1900nm in the illite II class points to a low temperature of formation while the illite I is of a higher temperature. The process of weathering seems to be quite effective at this point. The illite I is observed to be more associated with the sericite alteration zone while the low crystallinity illite II is found more in the Cu mineralisation zone. Another class of alteration minerals associated with the Cu mineralisation zone is the smectite group which is complexly mixed with the illite II. It formed three (3) classes of alteration minerals: the Smectite-Carbonate-Illite (SCI), Smectite-Illite (SI) and Smectite-Illite-Carbonate (SIC) minerals. The exposure of the argillic alteration minerals over the mineralisation zone is a typical reflection of the complex geological processes of tectonism and magmatic intrusion that has tremendously influence the Haib environment. Although the radioelement data was not able to analytically produce an anomalous distribution for the area, it highlighted the supergene Cu mineralisation zone and revealed a paleo-water table which enhanced a reconstruction of the geologic environment.

ACKNOWLEDGEMENTS

I most sincerely appreciate NUFFIC for sponsoring me for this Masters programme under the scheme name NFP. After successfully completing this programme, I truly believe the main aim of “linking knowledge worldwide” is being achieved by the organisation.

I am indebted to my supervisors, Dr. F. J. A. van Ruitenbeek and Prof. dr. F. D. van der Meer for the professional supports I received during this research. Your guidance, criticisms and openness to me are highly appreciated and commendable.

The readily available assistance and technical supports from my Course Coordinator, Ir. B.G.C.M. Krol, dr. H.M.A. van der Werff, dr. C.A. Hecker and other lecturers in the AES Department can never be forgotten.

The following institutions and individuals are further recognised for making the datasets and their services available during the planning and field work phase:

- Dr. Gabi Schneider, (Director, Geological Survey of Namibia, GSN)
- Ms. Anna Nguno, (Deputy Director, GSN)
- Dr. Titus Nortin (Geophysicist, GSN)
- Mr. Ewereth Muvangua (Chief Geologist, GSN)
- Mr. Michael Haimbodi (Geologist)
- Lady Paulina (Spectral Evolution Laboratory Technologist)
- Lady Taimi (Geochemist)

The Director-General, Nigerian Geological Survey Agency (NGSA), Mr. Nwegbu A. Ndubuisi is highly recognised for approving my study leave in the Netherlands.

I thank the Pastorate of the Redeemed Christian Church of God (RCCG), Amazing Grace Sanctuary parish, Enschede, Netherlands for the moral support meted out to me. Pastor Nelson Adelesi, Pastor Donald Ajibola, Dr. and Mrs. Ugo, Sister Abigail, Sister Tina Rosenburg, Mummy Queen, Chief Obasuyi and all the brethren in the church. The Provincial Pastor of the RCCG, Netherlands Mission is also appreciated for his fatherly prayers.

I strongly acknowledge all my international friends and colleagues for every collaborative session and accomplished missions. Kudos to you all.

Above all these, I give Glory to the Most High God and my Saviour Jesus Christ who kept and preserved me and my family all through the duration of the programme.

TABLE OF CONTENTS

Abstract	i
Acknowledgement	ii
Table of contents	iii
List of figures	v
List of tables	vii
1. Chapter one	9
1.1. Introduction	9
1.2. Research problem	9
1.3. Characterisation of Phanerozoic porphyry copper	10
1.4. Characterisation of Proterozoic porphyry copper	10
1.5. Research objectives	10
1.5.1. General objective	10
1.5.2. Specific objectives	11
1.6. Research questions	11
1.7. Datasets	11
1.8. Organisation of thesis	11
2. Chapter two	12
2.1. Literature review	12
2.1.1. Study area	12
2.2. Geology of Haib	13
2.2.1. Extrusive rocks	14
2.2.2. Intrusive rocks	14
2.2.3. Minor intrusive phases	14
2.3. Classification of the Haib host rock	15
2.4. Geochronological dating	15
3. Chapter three	16
3.1. Methodology and instrumentation	16
4. Chapter four	19
4.1. Hyperspectral data and result presentation	19
4.1.1. Introduction	19
4.2. Colour compositing in the visible/NIR range	20
4.3. Alteration minerals in porphyry Cu systems	22
4.4. Wavelength mapping	23
4.5. Empirical analytical approach	25
4.5.1. Spectral hourglass analytical method	25
4.5.2. Field and laboratory data acquisition	25
4.6. Spectral angle mapper	26
4.7. Linear spectral unmixing	27
4.8. Comparison of SAM with EnGeoMAP	29
4.9. The alteration mineralogy against the geology	29
4.10. Field reflectance data	31
4.10.1. Processing stage	31
4.11. Result from field reflectance data	32
4.12. Compositional variations detection from the field acquired spectra	33

4.13.	Coverage of spectra datasets.....	34
4.14.	Graphical analysis of the field spectra.....	36
4.15.	Geochemistry	36
4.16.	Metamorphic grade	40
5.	Chapter five	41
5.1.	Radiometric data and result presentation	41
5.1.1.	Introduction.....	41
5.2.	Geochemistry of radioelements	41
5.3.	Methodology	42
5.3.1.	Data presentation and enhancement	43
5.3.2.	Data integration.....	48
5.3.3.	Data interpretation and result synthesis.....	52
6.	Chapter six.....	53
6.1.	Validation.....	53
6.2.	Hyperspectral data.....	53
6.3.	Radiometric data.....	55
6.4.	Inferences.....	56
7.	Chapter seven.....	57
7.1.	Discussion of results	57
7.2.	Conclusions	57
7.3.	Recommendations	58
	List of references	59
	Appendix.....	62

LIST OF FIGURES

Figure 1. The location map and geology of study area (after Blignault, 1972).	12
Figure 2. The digital elevation model of the study area.....	13
Figure 3. (a) The spectral evolution device (b) the Niton XL 3t Gold+ XRF device (c) a display of rock sample in the laboratory for XRF measurements (d) XRF measurement setup at the Geological Survey of Namibia (Geochemical Laboratory).....	17
Figure 4. The flowchart for the research work.....	18
Figure 5. The position of SWIR in the electromagnetic spectrum (after G-Mex vol. 1).	19
Figure 6. ASTER image (a) 4:6:8 Colour composite (b) Decorrelation stretching applied on the composite image.....	20
Figure 7. Colour composite with wavelength values of bands (a) True colour composite (b) False colour composite.....	21
Figure 8. The Lowell and Guilbert 1970 Model.	22
Figure 9. A wavelength map as produced with the Hyppy software with ranges (a) 2.19 – 2.23 μm (b) 2.28 – 2.36 μm	24
Figure 10. Procedural steps deployed on the HyMap data.	25
Figure 11. SAM HyMap Classification (a) The mineral map of the Haib (b) Rule image settings (c) Spectra signatures.	26
Figure 12. LSU Outputs images (a)-(g) abundance fraction (h) RMS image.	28
Figure 13. EnGeoMap 2.0 mineral map output.....	29
Figure 14. Mineral map on the geology (at 75% transparency).....	30
Figure 15. Blocks A and B subset view of the mineral map over geology.....	31
Figure 16. A typical field spectra (a) noisy (b) after correction.	32
Figure 17. The wavelength position shift pattern in the alteration minerals acquired from the field spectra (a) – (n).....	35
Figure 18. Wavelength position shift range against alteration minerals.....	37
Figure 19. Potassium concentration across alteration zones.	38
Figure 20. Thorium concentration across alteration zones.	38
Figure 21. Uranium concentration across alteration zones.....	39
Figure 22. Iron concentration across alteration zones.	39
Figure 23. Copper concentration across alteration zones.....	40
Figure 24. The conventional four (4) spectral windows and photopeaks used in airborne gamma-ray spectrometer.	41
Figure 25. Flow chart on the radiometric data methodology.	42
Figure 26. Ternary image draped with the geological boundary of the study area.....	43
Figure 27. Potassium concentration distribution across study area.	43
Figure 28. Variation in potassium across geology.	45
Figure 29. Variation of thorium across geology.	45
Figure 30. Variation of uranium across geology.....	46
Figure 31. Stacked profiles orienting from north-south of study area (a) Potassium airborne gamma data concentration variation along flight line 374320 (cross section A-B in figure 5.4) (b) Thorium concentration (c) Uranium concentration (d) topographical relief.	47
Figure 32. The non-correlation relationship between Cu and K.	48
Figure 33. A log plot of Cu vs K concentrations showing all samples within the mineralisation zone.	49
Figure 34. XRF Concentration plot using graduated circles (a) for Copper (b) for Potassium.....	50
Figure 35. The rose diagram showing the dominating NW-SE structural trend in the Haib.	51
Figure 36. Geological structures and orientations (a) fractures randomly distributed with respect to alterations at L01 (b) Dextral fault displacement at L01 (c) Sinistral fault displacement at L05 (d) Jointing (healed with reddish brown minerals) at L02 (e) Fractures and joints in a sericitised rock exposure at L15.	52
Figure 37. Field reflectance sampling points against HyMap (SAM) output.	54
Figure 38. Graph showing the correlation relationship between the K concentration values as obtained from both the XRF and the airborne gamma ray data.	55
Figure 39. Field observation (a) inferred paleo-water table in yellow dash line (b) supergene Cu	

enrichment.....	56
Figure 40. The newly reconstructed alteration model of the Haib.....	57

LIST OF TABLES

Table 1. Endmembers generated from the Hyperspectral data.	28
Table 2. List of alteration minerals detected from the field samples.	33
Table 3. Summary of field alteration minerals with respect to their locations.	36
Table 4. Zonal statistical summary result on the airborne gamma ray data concentration of potassium in the rock units.	44
Table 5. Variation in the concentration of the Copper with respect to Potassium over the mineralisation zone.	49
Table 6. K concentration values from airborne gamma ray and XRF.	56

1. CHAPTER ONE

1.1. Introduction

Porphyry copper deposits of the world have been categorised on the basis of their geomorphology, tectonic setting and alteration mineralisation patterns associated with the system. The Lowell and Guilbert model has been widely used as a guide in the search and investigation for porphyry occurrences. Although other models are applied such as the diorite model, the most appropriate model for the Haib region is the Lowell and Guilbert type, otherwise known as the quartz-monzonite model. This is based on the similarity in the intrusion, alteration and mineralisation types observed in the geological system (Pirajno, 2008). A typical setting that best describes the porphyry copper system is shown in Appendix I (John et al., 2010).

Most of the porphyry copper deposits of the world have been known to be geologically associated with the Mesozoic – Tertiary ages (Sillitoe, 2010; Guilbert and Park, 1986). And globally, they have always been the main sources of about 60% of the world copper and 100% of molybdenum (Sinclair, 2007). Only few records on the emplacement and concentrated of porphyry copper through Precambrian times are known (Kesler and Wilkinson, 2007). One of such is the type-deposit occurring in the Haib region, now widely known to be of the Proterozoic age, the oldest of its kind (Minnitt, 1986) even though not producing at the moment .

The earth's most widespread ore deposit and important source of copper is the porphyry copper (Robb, 2009). Although other sources of copper include the Iron Oxide Copper Gold (IOCGs), skarns, polymetallic replacement, polymetallic veins and high sulphidation epithermal deposits, the giants are the porphyry Cu and the IOCGs (John et al., 2010). One major characteristic of this type of deposit is the potential to host a wide distribution of mineralisation types such as the chalcopyrite, molybdenite, bornite and disseminated sulphides (Sillitoe, 2010). A deposit such as this becomes very valuable when it sufficiently concentrate in an accessible portion of the earth and extractable at a profit (Robb, 2009).

Over the years, numerous researches have been conducted towards the exploration and exploitation of the porphyry copper deposit of the world. The present global demand for the resource and drastic increase in the population has culminated in a widespread interest (Lusty and Gunn, 2015). The critical role the development of this mineral resource alongside its associated mineralisation would play in the economy of Namibia, being a developing country cannot be underestimated, most especially with challenges of high rate of unemployment, poverty, infrastructural decay, etc.

1.2. Research problem

The distinctive occurrence of potassic alteration which has been used in characterizing the Phanerozoic-type porphyry Cu proves non-applicable in the Haib. This is simply due to the excessive K content in both the sub-alkaline and surrounding rocks (Barr and Reid, 1993). The two greenschist facies episodes regionally characterising the study area could possibly have led to the enrichment in K⁺ cation (Barr and Reid, 1993). The advantage of surface compositional information extraction with the hyperspectral data (Meer and Jong, 2003) will not reveal the K alteration minerals due to the absence of absorption features. This research is meant to bring about the understanding of the Haib porphyry Cu mineralisation with respect to the alteration mineralogy using hyperspectral and radioelement datasets.

Mapping the alteration zones with the intention of delineating the K-alteration halo using the two datasets is solely to delineate clearly the K-alteration associated with Cu mineralisation in the study area. This will be related with the Lowell-Guilbert model to measure the actual similarity or extent of deviation from the model.

1.3. Characterisation of Phanerozoic porphyry copper

The Mesozoic – Tertiary porphyry copper system has been successfully characterised based on the potassic alteration associated with it. This complies with the classic Lowell-Guilbert model which is widely used in characterizing porphyry copper systems. It clearly depicts the relationship of the porphyry system with hydrothermal alteration zones, as having a central potassic rich-core and concentrically surrounded by the phyllic and then propylitic alteration zones respectively. The mineralisation is found sandwiched between the Potassic and phyllic alteration zones. Argillic alteration could also be found between phyllic and propylitic alteration zones.

1.4. Characterisation of Proterozoic porphyry copper

One peculiar feature that distinct the Proterozoic Haib porphyry copper system from the Phanerozoic type is the impossibility of using potassic alteration as a characterisation tool. This is due to the fact that the host rock exhibits high K-content, hence, making it difficult to distinguish the K-alteration associated with the Haib deposit.

The Haib was described using two different scales, the regional and local. On the regional scale, the Haib tends to conform with the Lowell-Guilbert model while on the local scale, there is a reversal with respect to the model, in which the phyllic alteration overprints the earlier potassic assemblages, thus, resulting in K-alteration increase with depth (Minnitt, 1986).

According to literature, the Precambrian porphyry copper deposit seems not to be well represented when compared to the number of deposits of the Mesozoic to Tertiary age (Sinclair, 2007). This is because only a few Precambrian porphyry copper deposits are known all over the world. Even though the Haib copper ore system also exhibits similar characteristics of a porphyry system such as large tonnage, low grade and extensive hydrothermal alterations to mention but a few (Sillitoe, 2010; Berger et al, 2008) there is a view that the Precambrian porphyry type is of lesser tonnage than the younger ones, hence cannot be productive (Nironen and Csongradi, 1984). The associated mineralogical assemblage tend to typify a porphyry system (Beane and Bodnar, 1995).

Porphyry copper is typically found associated with arcs above subduction zones or volcanic arcs and occurring in arcs on active continental crust. It is known to be accompanied by alterations that can span extensively either vertically or horizontally across study area (Patrick, 2007; Minnitt, 1986). This pattern of alteration variation has been confirmed in the Haib region (Minnitt, 1986). Minerals that have been formed initially are variably altered and spatially distributed across terrane (Titley, 1982). Hydrothermal alteration mineral assemblages are widely used as searching tool for porphyry copper deposits (Holliday and Cooke, 2007).

1.5. Research Objectives

1.5.1. General Objective

The overall objective of this research is to characterise the Proterozoic porphyry copper deposit of the

Haib region, southern Namibia by studying and analysing the alteration mineralogy with respect to the K-rich rocks. This is meant to be achieved by using the hyperspectral and radiometric datasets.

1.5.2 Specific objectives

In order to accomplish the aforementioned objective, focusing on the under-listed specific objectives are priorities for this research:

1. To produce a mineralogical map of the study area using the hyperspectral data;
2. To relate the underlying geology of the terrane with the mineralogical map;
3. To produce a radioelement distribution map with respect to the average radioelement content in rocks using radiometric data;
4. To integrate the mineralogical map with the radioelement distribution map to improve K-alteration differentiation;
5. To match the pattern of geological structures with the mineralisation;
6. To attempt the detection of the effects of regional metamorphism in the terrane based on mineral assemblage.

1.6. Research questions

1. What minerals are found associated with the study area?
2. Is it possible to categorize these minerals into alteration zones?
3. How do these minerals relate with the geology of the terrane? Any association? Do the radioelements display any anomalous values in the rock units?
4. How does the mineralogical map vary from the radioelement distribution map?
5. Is there any correlation between geological structures and the mineralisation?
6. Is there any noticeable association between the mineralogical distribution and metamorphism in the study area?

1.7. Datasets

- i) HyMap dataset (hyperspectral): 126 bands, 5m resolution
- ii) Airborne gamma ray: High sensitivity 256 channels, Sampling interval 90m, Flight height 80m
- iii) Geological map: Scale 1:50,000
- iv) ASTER
- v) SRTM
- vi) Landsat 8
- vii) Topographic map

1.8. Organisation of Thesis

This thesis work is sectioned into seven (7) chapters.

- Chapter 1 basically highlights the research problem, overall objectives and research questions;
- Chapter 2 describes the study area and summaries the geological setting associated with it;
- Chapter 3 reviews on the methodology and instrumentation used in executing the research work;
- Chapter 4 introduces the hyperspectral and field spectral datasets and their output results;
- Chapter 5 emphasizes on the radiometric data and sample readings alongside their results;
- Chapter 6 validates the two datasets and incorporates the field data too;
- Chapter 7 discusses results and draws out the conclusions and recommendations for this work.

2. CHAPTER TWO

2.1. Literature review

2.1.1. Study area

The Haib study area occupies about 135 sq. Km and is bounded by longitudes 17° 46' 34.39" – 17° 56' 27.79" E of the prime meridian and latitudes 28° 40' 48.09" – 28° 45' 25.92" S of the equator (Figure 1). The Haib lies within the rugged terrain of Richtersveld province which is in southern Namibia and approximately 5km from the Haib – Orange River confluence, hence close to the South African border. The surface relief is related with the geology using the SRTM digital elevation model (Figure 2) while the drainage pattern associated with it is further revealed in the topographic expression (Appendix II).

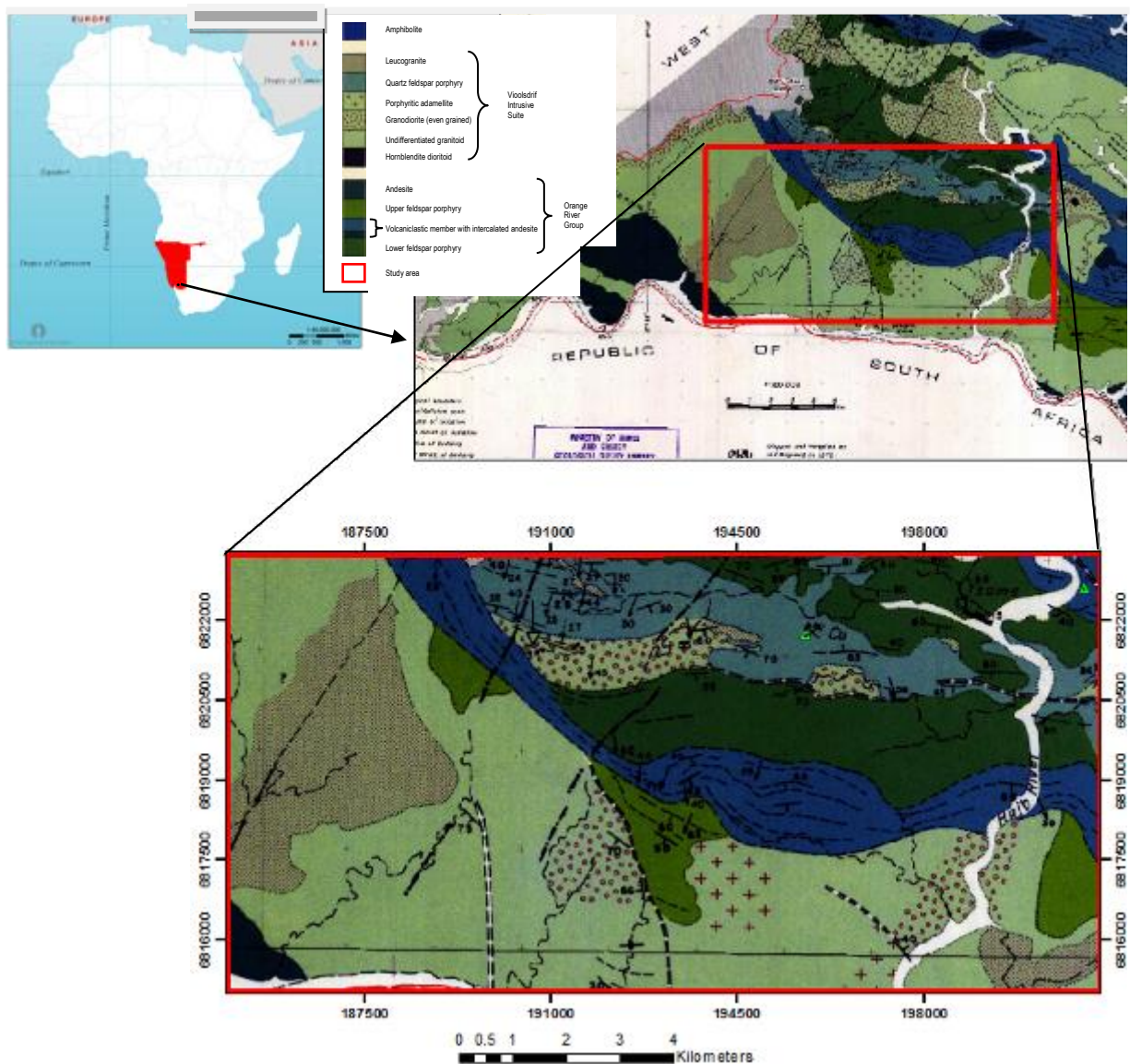


Figure 1. The location map and geology of study area (after BIGNAULT, 1972).

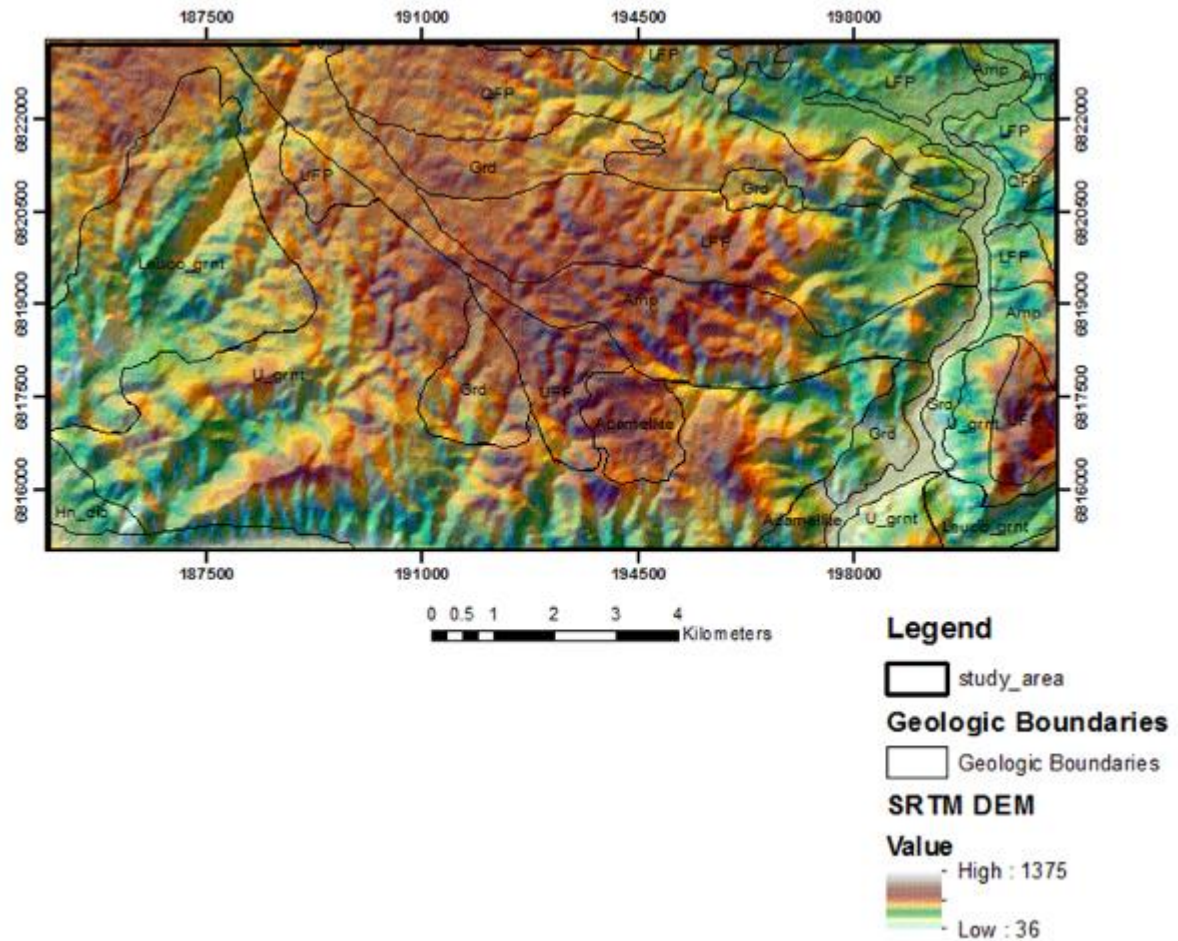


Figure 2. The digital elevation model of the study area.

2.2. Geology of the Haib

Haib occurs within the Namaqua-Natal belt, forming part of the Richtersveld province in southern Namibia. The geology of the terrane is characterised by the Orange River Group (ORG), Violsdrift Intrusive Suite (VIS), Richtersveld Intrusive Suite (RIS) and sedimentary units (Frick and Strauss, 1987). The ORG is the oldest rock units in the terrane and is divided into the basal Tsams Formation, and the overlying Nous Formation, the former being the only volcanic rocks present; it includes the metabasic and metafelsic lavas in the vicinity of the Haib copper prospect. The volcanic flows of intermediate to acid tuffs, metamorphosed tuff, agglomerate, sandstone, chert, schists, mafic flows and tuff comprise the central and uppermost units, respectively. The Feldspar Porphyry (FP) which consists of undifferentiated porphyritic dacites and andesites is part of this group (Barr and Reid, 1993; Minnitt, 1986). The intrusion of the VIS into the ORG resulted in large xenoliths. The metavolcanic rocks have been dated to be ~ 2.0 Ga (Reid, 1979) while the VIS has been categorised under the granodioritic ~ 1.9 Ga (Barton, 1983) and granitic phases ~ 1.7 Ga (Reid, 1982). The Haib Quartz Feldspar Porphyry (QFP) is a minor portion of the VIS that hosts the mineralisation (Barr and Reid, 1993) although the FP also hosts mineralisation (Minnitt, 1986). The RIS eventually intrudes into the ORG and VIS producing rocks like syenite and alkali-granite (De Villiers and Sohng, 1975) and at a date of $\sim 0.92 \pm 0.03$ Ga (Allsopp et. al, 1979). The three groups of lithologic units are overlain by the sediments of the Gariep complex (Frick and Strauss, 1987). The variety of igneous rocks found in the terrane range from ultramafic to felsic. The violsdrif suite comprises of basic – ultrabasic complexes, diorite, tonalite, granodiorite, adamellite, quartz-feldspar

porphyry and leucogranite which were emplaced during two main phases of intrusive activities. Diorite, tonalite and granodiorite were intruded approximately 1960 ± 30 Ma ago, while the adamellite and leucogranite were emplaced 150 Ma later, according to the Rb-Sr radiometric ages determined for these rocks by (Reid, 1977).

2.2.1. Extrusive rocks

The extrusive rocks that characterise the Haib study area are summarised below:

- i) **The Feldspar Porphyry (FP)** – This rock unit is intercalated with lenses of acid volcanics and represents the lowermost stratigraphic unit in the terrane while mafic quartz-feldspar porphyry lava, mafic volcanics and rhyolite overlie it. It is divided into the Lower FP (LFP) and the Upper FP (UFP). The FP is a simplified term used in describing undifferentiated porphyritic dacites and andesites which predominate in the vicinity of the Haib prospect. The massive lavas are greenish grey, consisting of sericitized and saussuritized plagioclase euhedral in a fine-grained matrix of quartz-feldspar-biotite grains.
- ii) **The acid volcanics** – These are sheets, yellowish and lenses of acidic volcanics interlayered near the base of the feldspar porphyry. They are leucocratic tuffs which are locally reworked and consist predominantly of quartz, sericite and pyrite (Minnitt, 1986).

2.2.2. Intrusive rocks

This group of rocks came after the FP and acid volcanics.

- i) **The granodiorite** - being part of the Vioolsdrif suite, it occurred in most areas and formed the plateaux to the northern region of the study area. The texture varies from medium to coarse-grained, and composed of quartz, plagioclase, K-feldspar, biotite, sericite and epidote. It also includes saussuritized hornblende and minute amounts of zircon, sphene, rutile, leucoxene, and opaque minerals.
- ii) **Adamellite** - describes the generally foliated, K-feldspar phenocryst-bearing granodiorite and are richer in alkali-feldspar and silica than granodiorites.
- iii) **Leucogranite** – this is the most recent member of the Vioolsdrif suite which evolved as bosses and vein-like intrusives; the intrusives are fine-grained and more altered than the plug-like bodies of the leucogranite. It is composed of alkali-feldspar, plagioclase and quartz with chlorite or biotite being present in minor amounts.
- iv) **The Haib porphyry stock** - is composed of quartz-feldspar porphyry (QFP) that intrudes adjacent granites and volcanics. It aligns in a north west – south east direction, reported to be measuring about 11 by 3 km and having a broad width at the mineralisation area. It tends to wedge out towards both the eastern and western direction of the ore zone (Minnitt, 1986).

2.2.3. Minor intrusive phases

Several of this type of rock units has been found within the study area.

- i) **Leucocratic quartz-feldspar porphyry** intrudes the Haib porphyry stock. There are two types of quartz-feldspar porphyry; both displaying gradational and sharp contact relationships. The leucocratic type has undergone potassic and sericitic alteration. The overprinting of the potassic alteration by weak sericitic alteration is observed in this unit.
- ii) **Quartz diorite** describes the weakly sericitized FP which shows inclusions of QFP, that is associated with the zone of mineralisation. Observations of potassic and sericitic alteration of the quartz diorite confirmed that it intruded before potassic alteration, being the earliest phase of silicate alteration.

2.3. Classification of the Haib host rock

Since early 1930s, the “Calc-alkaline” series of rocks have been defined on the basis of “alkaline-lime index” which is obtained by combining $(\text{Na}_2\text{O}+\text{K}_2\text{O})$ versus SiO_2 and CaO versus SiO_2 plots. It has been noted that there is no standardized definition for the “Calc-alkaline” rock type (Middlemost, 1985). In current usage, it has been defined as a rock having high concentrations of CaO with respect to alkalis when compared with alkaline igneous rocks (Kearey, 1993). Using the geochemical classification scheme, the Total-Alkalies-Silica (TAS) diagram classified both the “tholeiitic” and “calc-alkaline” series under “subalkaline” (Wilkinson, 1968). Although another school of thought stated that the “subalkaline” can be further categorised into high alumina/calc-alkaline and a low-K tholeiitic series which corresponds to the subalkaline and low-K subalkaline classes (Middlemost, 1975). However, the plotting of calc-alkaline series on the TAS diagram is inaccurate because neither Al_2O_3 nor CaO are present as plotting parameters (Sheth et al, 2002).

Several investigations have been conducted in the Haib region towards understanding the geological system as it relates to the ore deposit. Authors have generally described the host rock as “Calc-alkaline” a term which has been used to define rocks related to island-arcs or subduction zone rocks that range from basalt to rhyolite; or intermediate rocks that fall within low-K and high-K series (Wilson, 1996). The complexity of classifying rocks with the term “Calc-alkaline” has warranted its elimination by the International Union of Geological Sciences (IUGS) sub-commission on Systematics on Igneous Rocks (Le Bas, 2000; Le Bas et al, 1986). This is simply due to the limitation of the geochemical discrimination diagrams in properly classifying the rock suite. Sub-alkaline has long been adopted by IUGS (Sheth et al., 2002).

2.4. Geochronological dating

The inception of geochronological dating methods has generated impressive geological age models and assisted in understanding more about complex geological processes that produced both magmatic and mineralisation emplacements. For instance, molybdenite and sulfide ore deposits in other regions of the world have been dated using Re-Os isotopes analysis (Stein et al, 2001). The dating of polyphased mineralizing events has been done with the Re-Os and U-Pb isotopes (Wilson et al, 2007; Rohrlach and Loucks, 2005; Richards et al, 1999). The dating of the rocks in the Haib has been well documented (Reid, 1977), events between the mafic and felsic endmembers of Violsdrif Intrusive Suite (VIS) intruding the Orange River Group (ORG) seems unclear. It was also pointed out that the Rb-Sr isotopes used in dating the mineralisation was not precise. The vast scientific work in the area of geochronometry has greatly modelled the Precambrian Haib porphyry copper ore deposit using isotopic elements with distinctive geochemical and nuclear properties to date rocks and minerals, study rock-water interactions, magmatic processes, etc (Baskaran, 2011).

Generally, evidence of low grade metamorphism was recorded in the periods ~ 1.20 to ~ 1.04 Ga while high grade metamorphism was not detected (Eglington, 2006). Although the tectono-magmatic and metallogenic evolution dated late Kibaran orogeny (~ 1.1 Ga), high grade metamorphism remain undocumented (Thomas et al, 1994). At the peak of metamorphism, a penetrative regional fabric which appeared dominant was created (Eglington, 2006); although regional fabrics do not control localisation of deposits (Sillitoe, 1993), the local lineament distribution pattern as it affects the mineralisation in the area was not revealed. The spatial relationship that this structural fabric has with metamorphism is not included.

3. CHAPTER THREE

3.1. Methodology and Instrumentation

The procedures deployed in this research can be categorised into six (6) stages. The supporting flowchart is shown in figure 4 below.

a) **Input of datasets** – This research project commenced with the collection of relevant and easily available datasets meant to aid in its effective execution. Since the porphyry copper system has been known to be associated with hydrothermal alterations, the ASTER 468 False Colour Composite (FCC) was used as a reconnaissance tool to highlight the silicate alteration zones in the study area. This assisted in planning for the field work stage as it guided in the positioning of target sample points. The SRTM DEM (Figure 2) revealed the topographic terrain and its accessibility limitations. The extraction of lineaments was done with the Landsat 8 (Appendix II). The incorporation of the radioelement and hyperspectral datasets as the main characterisation tools in this research is an advance approach in addressing the scientific questions.

b) **Pre-field Analysis** – The crosstalk correction was done on the ASTER data to check for signal leakage from band 4 sensor to other detectors (Aleks and Oliver, 2004). This was followed by the surface reflectance calculation using the Fast Line-of-Sight Atmospheric Analysis of Spectral Hypercubes (FLAASH) tool in ENVI 5.1. The final correction step was done with the band maths. The Minimum Noise Fraction (MNF) and Pixel Purity Index (PPI) tools were used to reduce the noise in the image and calculate the purest endmembers respectively. Five endmembers were initially derived with the ASTER data and the spatial distribution of the alterations was also viewed.

The Shuttle Radar Topographic Mission (SRTM) of 30m resolution coverage was downloaded from the earthexplorer.usgs.gov website. Also the Landsat 8 was obtained through the USGS website. The Landsat 8 was pan-sharpened to a 15m resolution image with ENVI before being processed in the PCI Geomatica for lineament extraction.

The Oasis montaj 8.4 was used to georeferenced the radiometric data and produce the ternary image. This showed similarities in the lithological boundaries. The Potassium concentration distribution across the entire study area was also created from the database platform. Profiles from uranium and thorium were also created for comparison and further analysis of the result.

The four (4) Hyperspectral image scenes (16-19) covering the study area were mosaicked together before applying geometric correction using the .glt file extension to produce one raster image. A subset of the image was done to avoid long processing time due to the size of the data. The FLAASH and band maths tools was then applied to calculate the surface reflectance. The HypPy Python software was then used to plot the minimum wavelength map between 2.1 – 2.4 μm .

c) **Sampling** – The field mapping phase of this research entailed the GPS tracking and collection of rock samples that represent silicate alterations in the study area. Photographs of alterations and samples were also captured alongside geological features of interest. Prominent feature orientations were measured and compared with base map pattern. Textural variations in rock samples/exposures were noted. Elevation values at each sample location were also recorded. The Spectral Evolution device was used to acquire spectral measurements from the 33 samples collected (Figure 3a). The device saved the signatures in a .sed file extension format which was further compiled with the spectral library builder tool in ENVI.

Subsequent measurements by the Niton XL 3t Gold+ was also done for the XRF (Figure 3b-d).

- d) **Validation** – The essence of this stage is to compare the results obtained from the measurements carried out on the field samples with the remotely sensed output (hyperspectral and radiometrics). The laboratory measurements in the form of reflectance and XRF data were compiled independently and applied appropriately. The endmembers generated from the mineral map via the hyperspectral were compared with those generated with the spectral device while the radioelement concentrations from the XRF were related with the airborne gamma data.
- e) **Integration** – The complementarity of result outputs from the different datasets is to aid in the interpretation of the final result. This will enable the answering of all the research questions pertaining to this work. The output of the mineral map from the hyperspectral data after undergoing validation with the field spectra, will be related with the geology; this in turn will be related with the radiometric after going through validation with the XRF data. Other datasets as they pertain to this work are fully incorporated for logical interpretation purposes.
- f) **Interpretation** – This stage is meant to derive a reasonable conclusion from the integration of all the analytical results as obtained from the available datasets deployed in this research.



Figure 3. (a) The spectral evolution device (b) the Niton XL 3t Gold+ XRF device (c) a display of rock samples in the laboratory for XRF measurements (d) XRF measurement setup at the Geological Survey of Namibia (Geochemical Laboratory).

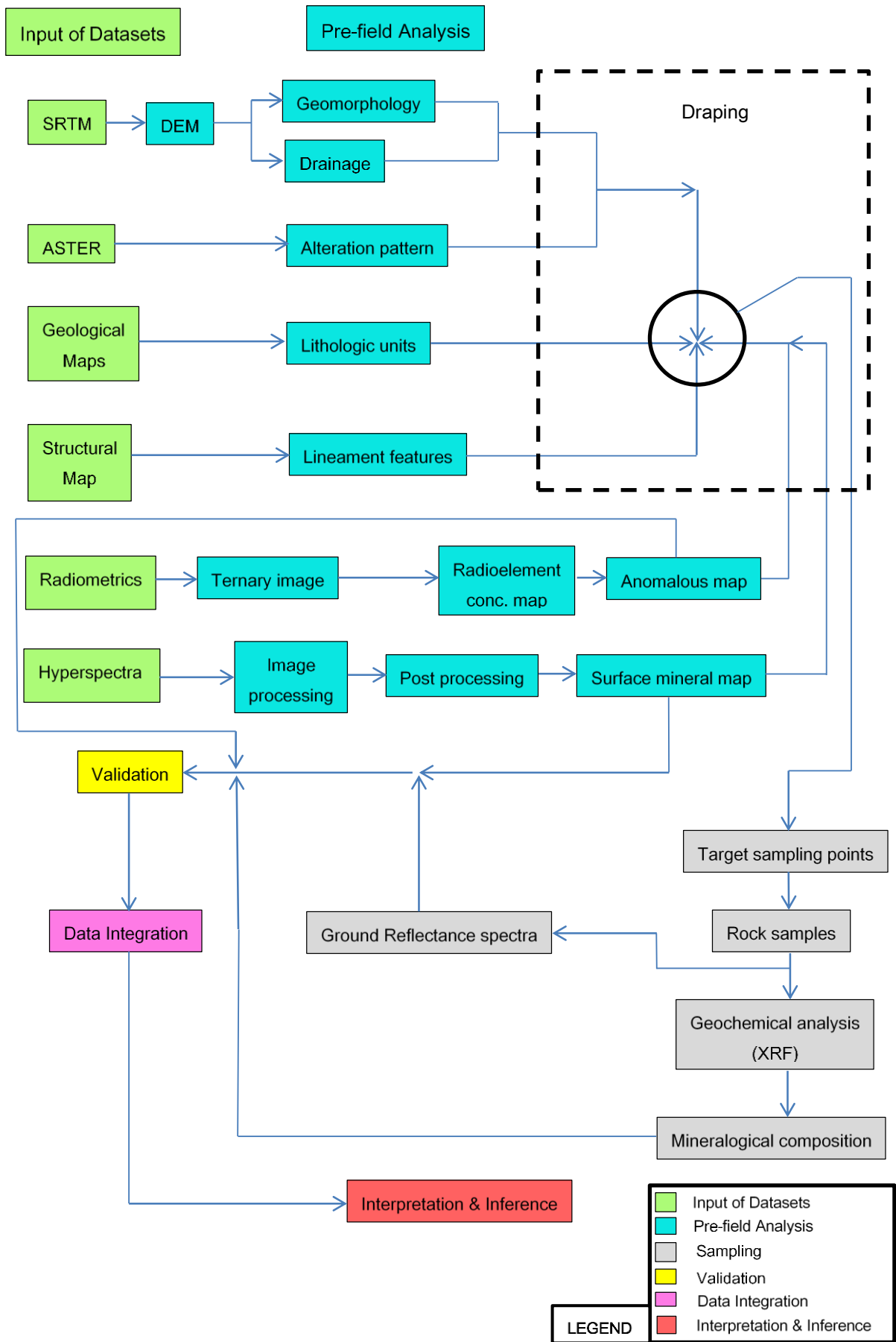


Figure 4. The flowchart for the research work.

4. CHAPTER FOUR

4.1. Hyperspectral data and result presentation

4.1.1. Introduction

The irradiation from sunlight plays a fundamental role in reflectance measurement within the wavelength range 0.4 – 2.5 μm . The resulting effect of the interaction of light with most materials lead to molecular vibrations as energy is absorbed into the molecular structure. This has produced significant interpretation results on materials chemical composition detection from reflectance data. In other words, typical spectrum that best describes the chemical content of most materials is revealed within this wavelength position range. The spectral position of SWIR within the electromagnetic spectrum is shown (Figure 5). This advancement in spectroscopic sensor technology has made possible the ability to map compositional information from the earth surface. Although the Advance Space Thermal Emission and Reflectance Radiometer (ASTER) served as a reconnaissance tool in locating target zones within the study area, it was not able to uniquely distinct variations in mineralogical compositional. The bands 468 False Colour Composite (FCC) categorically revealed the alteration status of the study area (Figure 6a) (ASTER, 2001). This was further enhanced by decorrelation stretching (Figure 6b). The superiority of the hyperspectral imaging over the multispectral is extremely overwhelming (Kruse, 1994). Since most imaging applications are more pronounced in the 0.4 to 14 μm spectrum region, a progression into the Short Wavelength Infrared (SWIR) range highlights the relevance of this wavelength range in this research (Salisbury, 1998). The characteristic spectra of most minerals are based on their wavelength absorption positions in the 2.1 – 2.4 μm SWIR region of the electromagnetic spectrum (van Ruitenbeek et al., 2013). These descriptive features are best defined as harmonics of the fundamental absorption features in the mid-infrared region. The spectral signatures displayed by several minerals in the SWIR reflect the molecular vibrations which tend to characterise them distinctly after interaction with light energy.

The chemical bonds that exists between combination groups such as Al-OH, Mg-OH, Fe-OH, hydroxyl, water, carbonate and ammonia variably highlights and differentiates some important silicate minerals (Sasha et al., 1997). These features are found near 1.4 μm (OH and water), 1.9 μm (water), 2.20 μm (AlOH), 2.25 μm (FeOH) and 2.23 μm (MgOH). The class of minerals prone to exhibiting these feature traits include the phyllosilicates, hydroxylated silicates, sulphates, carbonates and ammonium minerals (van Ruitenbeek et al., 2013).

This aspect of the research is solely aimed at accurately identifying features that can be appropriated as characteristic minerals associated with the study area. The expertise of deploying the right image analytical tool comes into play in other to achieve the most desirable result.

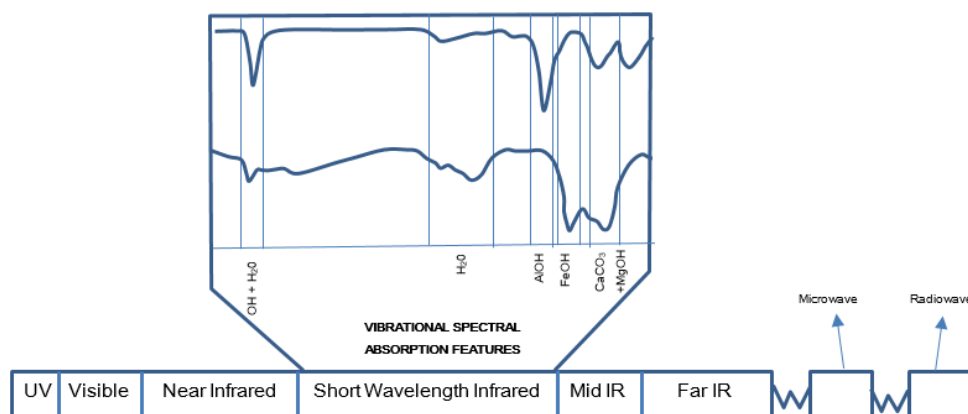


Figure 5. The position of SWIR in the electromagnetic spectrum (after G-Mex vol. 1).

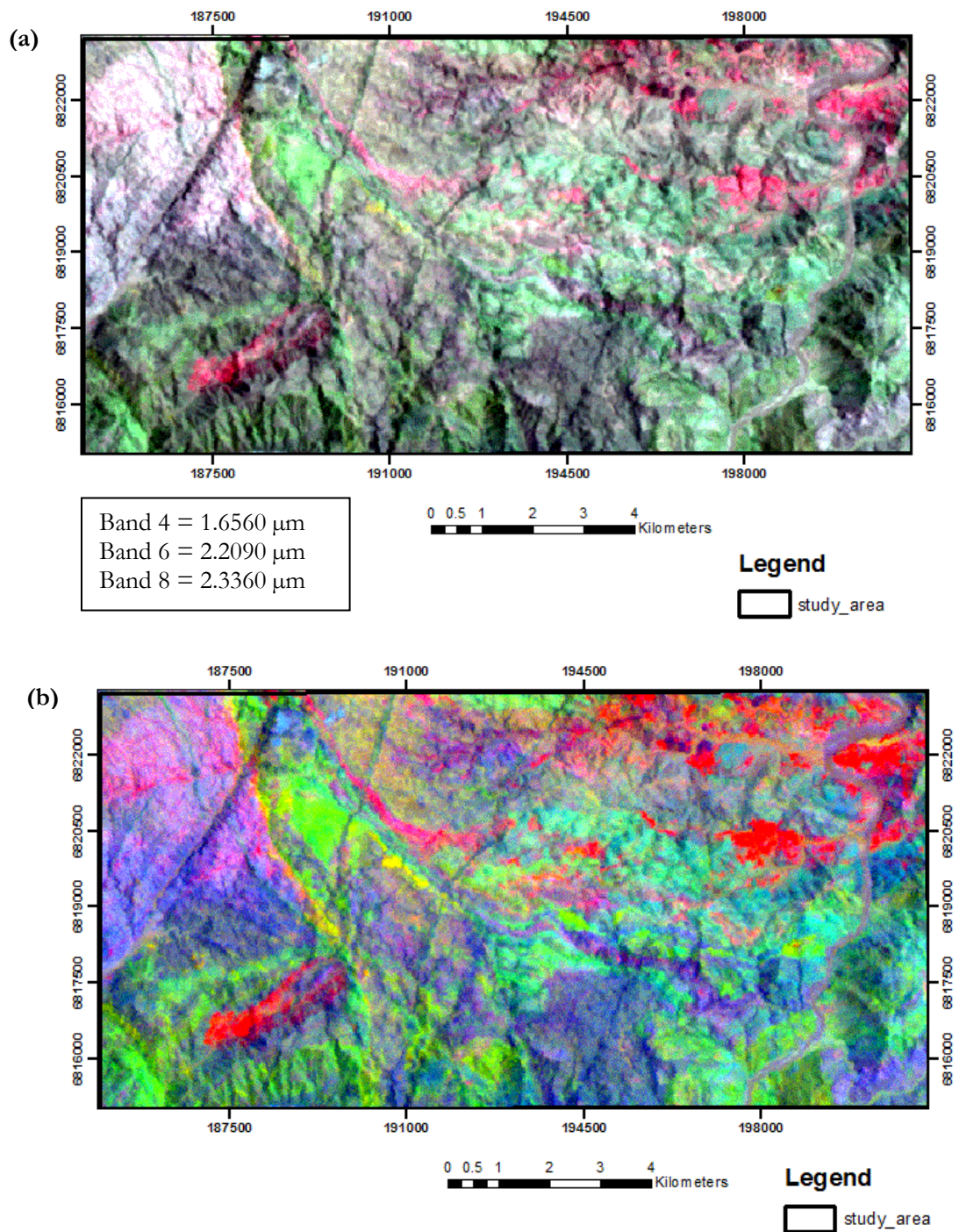


Figure 6. ASTER image (a) 4:6:8 Colour composite (b) Decorrelation stretching applied on the composite image.

4.2. Colour compositing in the Visible/NIR range

The surficial expression of features was studied using the Hyperspectral reflectance band combinations 14, 8, and 2 for a True Colour Composite (TCC) and bands 28, 14 and 8 for False Colour Composite (FCC) (Figure 7a and b respectively). The TCC band 14 revealed partly soil-covered rocks with little to no vegetation, weathered appearance (brown-reddish brown) variably dissected by drainage channels and

creek. Bands 8 and 2 reveals the phyllosilicate rich areas having the highest reflectance (whitish). The FCC band 28 reveals vegetation as red pixelations, this further confirms the aridity of the area. Bands 14 and 8 reveals the colour range of soils and rock exposures with no vegetation varying from white to green and brown (Figure 7b).

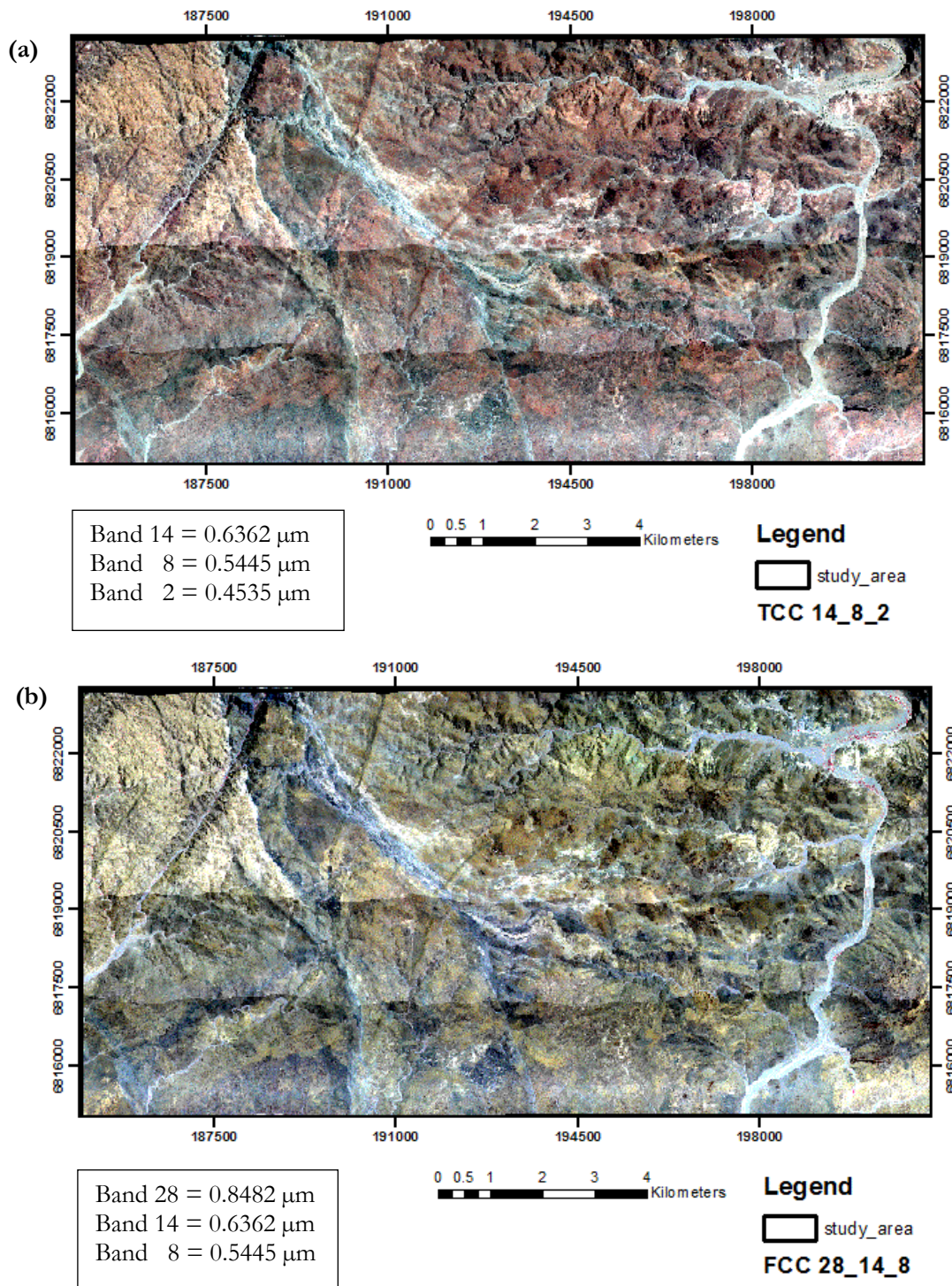


Figure 7. Colour composite with wavelength values of bands (a) True colour composite (b) False colour composite.

4.3. Alteration minerals in porphyry Cu systems

One significant attribute that best qualifies the porphyry Cu system is that large volumes of rocks are variably altered. This is always distinguishably observed on the surface representing different mineral assemblages typical to the system. Apparently, these alteration zones are complexly distributed and have been described based on their spatial relationship with the metallization. These vast volumes of rocks revealing differential extents of alteration resulted from diverse hydrothermal fluid circulations in the permeable layers. The important contributions of microfractures and fractures to the convective circulation of fluids cannot be underestimated. The most widely used systematic classification of porphyry copper in the world is the “Lowell and Guilbert” model (Beane and Bodnar, 1995). This is adopted in this research to underscore the characterisation of the Haib porphyry system by observing surface mineralogical variations. This model simply summarises the alteration silicates as zoned from the centre rich in biotite, K-feldspar and magnetite, otherwise known as the potassic alteration zone; next is the phyllic alteration, dominated by sericite and pyrite, being the most easily noticed alteration type; the argillic alteration zone consisting of montmorillonite and Illite; followed by the propylitic alteration comprising of epidote, chlorite and calcite minerals (Figure 8). According to the paragenetic sequence model, the Cu mineralisation is known to be occurring between the potassic and the phyllic alteration zones.

Most of the mineral assemblages have distinctive absorption features in the SWIR region of the electromagnetic spectrum with the exception of biotite, k-feldspar and magnetite (potassic alteration), which are impossible to detect with remote sensing technique.

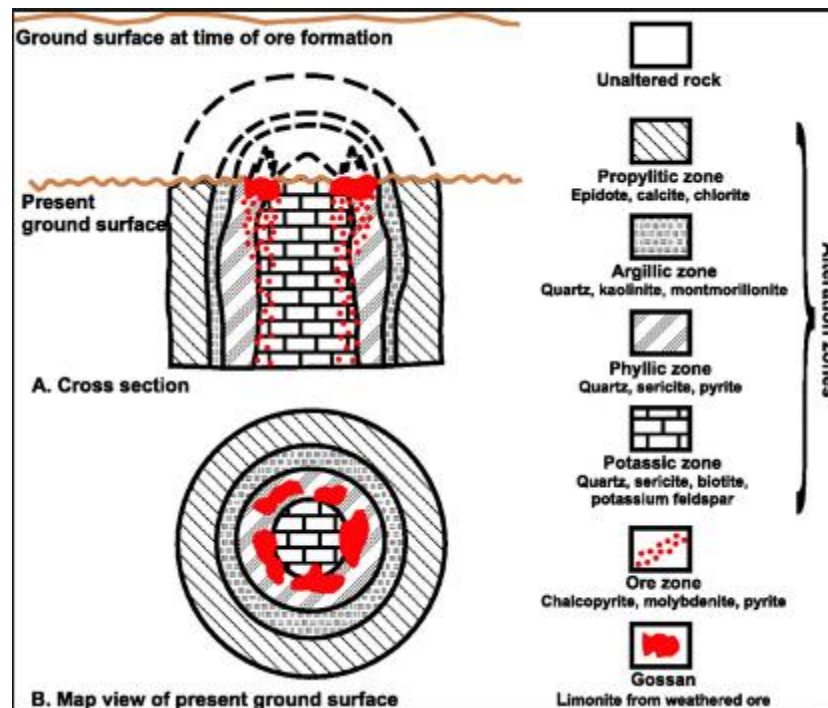


Figure 8. The Lowell and Guilbert 1970 Model.

4.4. Wavelength Mapping

The initiation of the Hyperspectral python (HypPy) programme was an efficient and well-guided approach in having an overview of the alteration patterns as they exist in the study area using the hyperspectral image. It calculated the wavelength positions of the deepest absorption features and then combined the interpolated wavelength image with the interpolated depth image (Bakker et al, 2011). This produced a visualization of the absorption band map that reflected the alteration in the area (Figure 9). The 2.1 – 2.4 μm spectra range was used as target region in the SWIR because most of the minerals associated with hydrothermal alterations have their characteristic features within this range. This attempt produced a summary result of minerals having their deepest absorption spectral features falling between (a) 2.19 - 2.23 μm (b) 2.28 – 2.360 μm . The first wavelength image as summarised in figure 9a, shows a colour pattern varying from cyan through yellow to red; with the cyan near the 2.200 μm AlOH absorption feature characteristic of illite and muscovite. The higher end of the range still falls within the wavelength position class of these phyllosilicate minerals. The second image summarised in figure 9b, shows a colour variation from green through yellow, orange to red. The cyan is having wavelength value near 2.310 μm which is characteristic of actinolite; yellow near 2.325 μm for chlorite mineral. Longer wavelength endmembers tend to reveal overlapping tendencies between MgOH and CaCO_3 features.

The mineral groups exhibited the phyllosilicate features (AlOH minerals) with wavelength ranging from 2.180 μm - 2.228 μm ; also diagnostic FeOH with wavelength position near 2.230 μm - 2.250 μm is present. These are seen to be pronounced in the upper north-central to north-eastern portion of the study area, where mineralisation has been observed. Other minerals have their deepest absorption features within the ranges 2.160 - 2.180 μm (sulphate) and 2.320 - 2.360 μm (MgOH).

Most of the feature depths characterising this study area are above 16% and attaining a maximum value of 24%, hence significantly well represented on the images (Figure 9a & b). Regions without diagnostic features within this wavelength range remain completely black in the images.

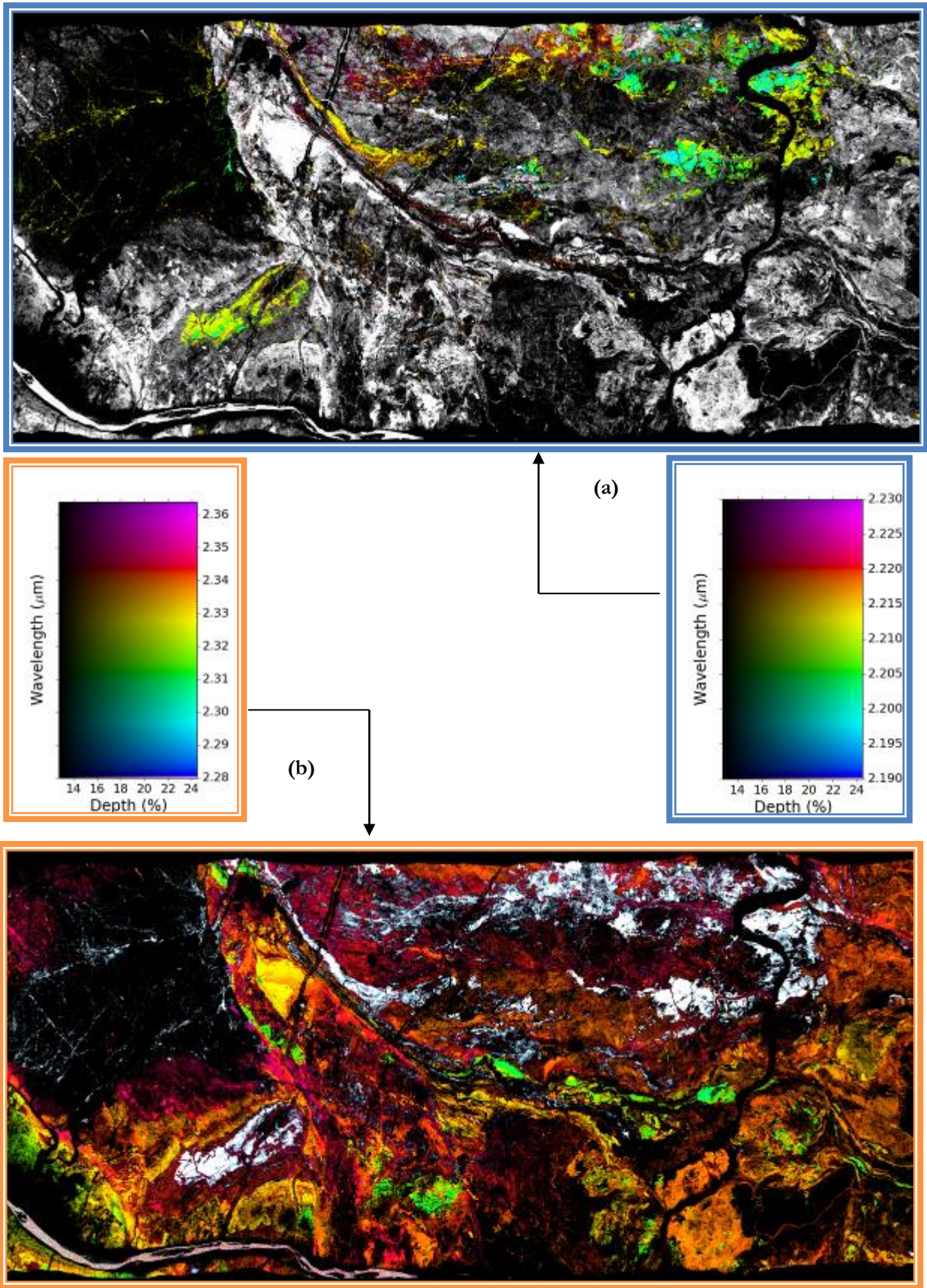


Figure 9. A wavelength map as produced with the HypPy software with ranges (a) 2.19 – 2.23 μm (b) 2.28 – 2.36 μm.

4.5. Empirical Analytical Approach

4.5.1. Spectral hourglass analytical method

The spectral hourglass analytical approach was adopted in the processing and analysing of the hyperspectral data in order to extract detail mineralogical information. One of the advantages of applying this procedure is to reduce the processing time of the large HyMap data and at the same time remove noisy bands that affect the final output result. The four scenes of 126 bands each covering the entire study area were mosaicked together using the image encoding data type, Band Sequential (BSQ). This was followed by geometric correction with the .glt file. This was subset to an area approximately 135sq. Km. The apparent reflectance was calculated using the Fast Line-of-sight Atmospheric Analysis of Spectral Hypercubes (FLAASH) and the band maths tools. The Minimum Noise Fraction (MNF) tool was used to reduce the dimensionality of the data and improve the signal to noise ratio. The higher data variance as revealed in the MNF eigenvalues plots was segregation from the noise floor. Hence, the most information as it pertains to the intrinsic endmembers is contained in the lower MNF bands. This step was followed by the Pixel Purity Index (PPI) projection which extracted the most extreme pixels from the image data cube. 10000 iterations were used in this calculation. This process produced all the purest pixels associated with the hyperspectral image. The identification by spectral matching of the unknown endmembers with the USGS spectral library was done with the n-D visualizer and spectral analyst tools, where the mean spectral of clustered pixels were used for the matching. The spectral library was built containing characteristic spectral signatures. The stepwise analytical approach is summarised in the chart below (Figure 10).

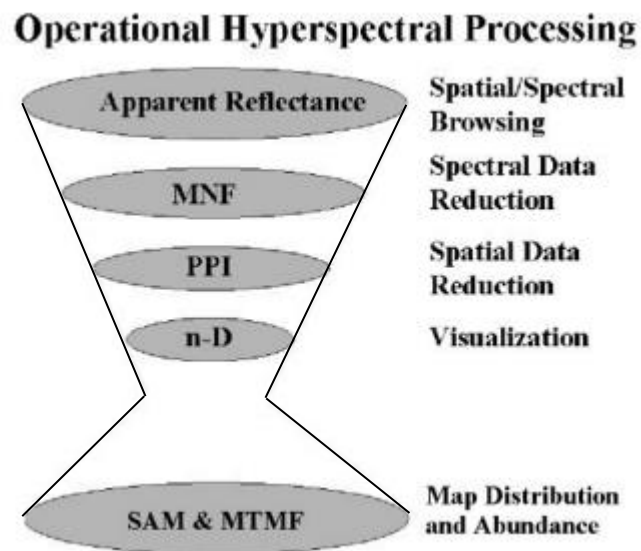


Figure 10. Procedural steps deployed on the HyMap data (Kruse et al, 2003).

4.5.2. Field and laboratory data acquisition

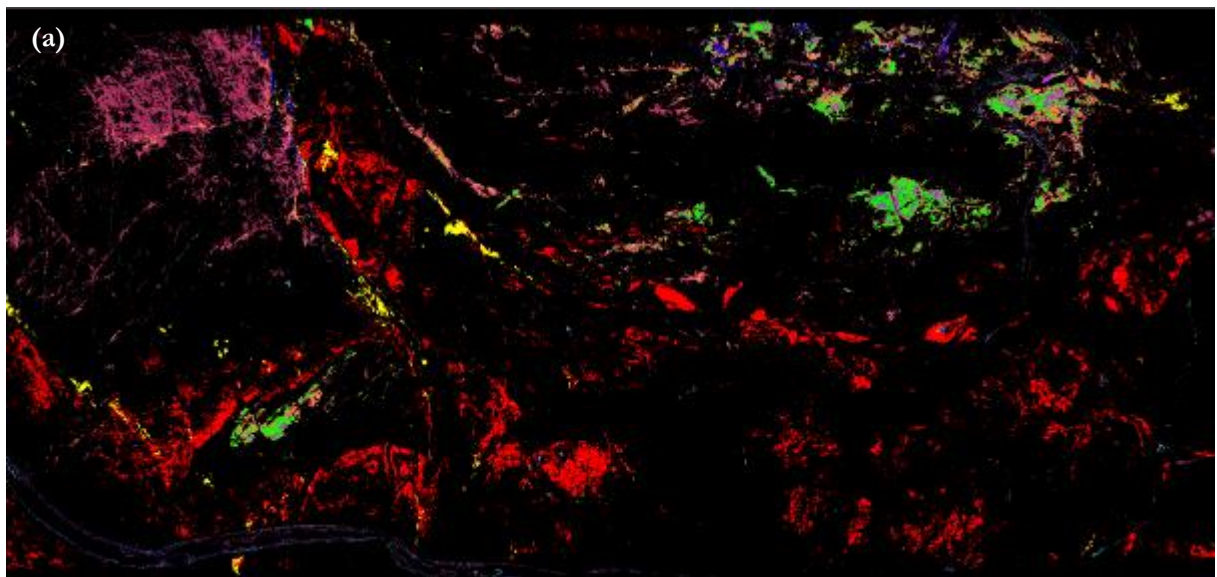
The ground-truthing and laboratory phase of this research was carried out to enhance data validation and possibly to reconstruct the model that is peculiar to the Haib. This procedural phase was achieved by acquiring both the reflectance and geochemical data from the mapped lithological units based on extent of alteration captured by sampling. The Spectral Evolution (SE) device was used to measure 23 rock samples and 203 spectral signatures were acquired and stored as text files (ASCII). The hull correction was applied

to the spectra to account for the influence of out-of-range absorptions which affects the continuum of the spectrum. This to an extent led to the separation of bad and unmatchable spectra from the spectral database, although a smoothening was deployed which corrected and made most noisy spectra diagnosable. The class of endmembers generated from the analysis of the field spectral signatures were compiled (Table 2).

The portable Niton XL 3t Gold+ (XRF) device was used to estimate the concentration of some heavy metals in the rock samples, of particular interest are the radioelements (K, Th and U), copper and iron. It is worth noting that the Rare Earth (REE) and the lighter elements cannot be detected by the portable device. And any concentration value below 10ppm was disregarded, this is due to the standardization setting used in the Geochemical Laboratory of the Geological Survey of Namibia.

4.6. Spectral Angle Mapper

All the endmembers obtained after successfully using the n-D visualizer to extract the purest pixels from the hyperspectral image was built into a spectral library. A total number of ten (10) endmembers were satisfactorily derived from the procedure (Figure 10) above. These ten endmembers are summarised into eight (8) classes of minerals because the montmorillonite and the illite tending to phengite are of two categorises each. This is due to the differences in their feature depths (Table 1). The spectral analyst tool was used in identifying the minerals constituting the pixels in the image. The newly developed spectral library was used as a training set (group of spectra) to which the image pixel clusters was compared using the Spectral Angle Mapper (SAM) tool in a supervised classification method. This tool related the training set with the image spectra by comparing the two spectra for a perfect match. The angular relationship between them must be close to zero in order to match, hence an image is created on a pixel basis. Each spectral is treated as a vector and SAM makes use of the vector direction instead of the length (Kruse et al, 1993). The final classification image using SAM alongside the rule image classifier settings and spectra signature patterns typical of the Haib are included below (Figure 11a-c).



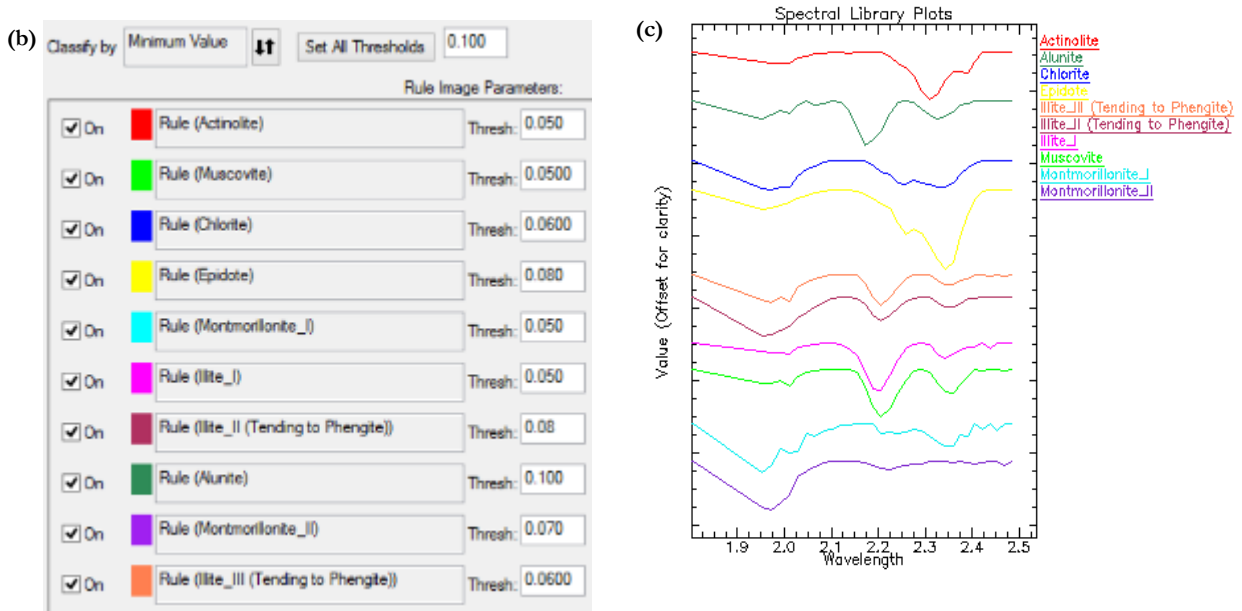


Figure 11. SAM HyMap Classification (a) The mineral map of the Haib (b) Rule image settings (c) Spectra signatures.

4.7. Linear spectral unmixing

It has been well documented that in order to correctly unmix an image as complexly-banded as the hyperspectral image, the unmixing algorithm makes use of a mixing model to carry out the inverse operation. For instance, if k represents spectral bands and the i th spectrum for endmembers is denoted as s_i , while the fractional abundance of the i th spectrum is assigned a_i , therefore, the mapped spectrum from the pixelated image is expressed as equation (1) below (Keshava, 2003).

$$\begin{aligned}
 x &= a_1s_1 + a_2s_2 + \dots + a_ms_m + w \\
 &= \sum_{i=1}^M a_i s_i + w = S_a + w
 \end{aligned}$$

Equation (1)

where M represents the endmembers count, S stands for the matrix and w is for the error (which includes forms of noise, etc.)

The inverse operation of trying to retrieve endmembers as constituents of the hyperspectral image, as well as the fractional abundance of each pixel was executed with the Linear Spectral Unmixing (LSU) technique. This was per pixel basis. Although based on both remote sensing and field observations, it can be categorically deduced that the Haib is more associated with a non-linear mixing model, which is a complex scenario of an unorderedly arrangement of materials. The final result is evaluated with the aid of the Root Mean Square (RMS) image (Figure 12h), where image pixels with bright colours (white) symbolises high errors and darker portions represent low errors (Gong and Zhang, 1999).

The final output produced series of gray-scale images representing each correctly assigned endmember and an RMS image which depicts the error status of the process, hence can be used to detect wrongly chosen endmember (Figure 12a-h). The LSU served as a validation tool for the SAM in this context.

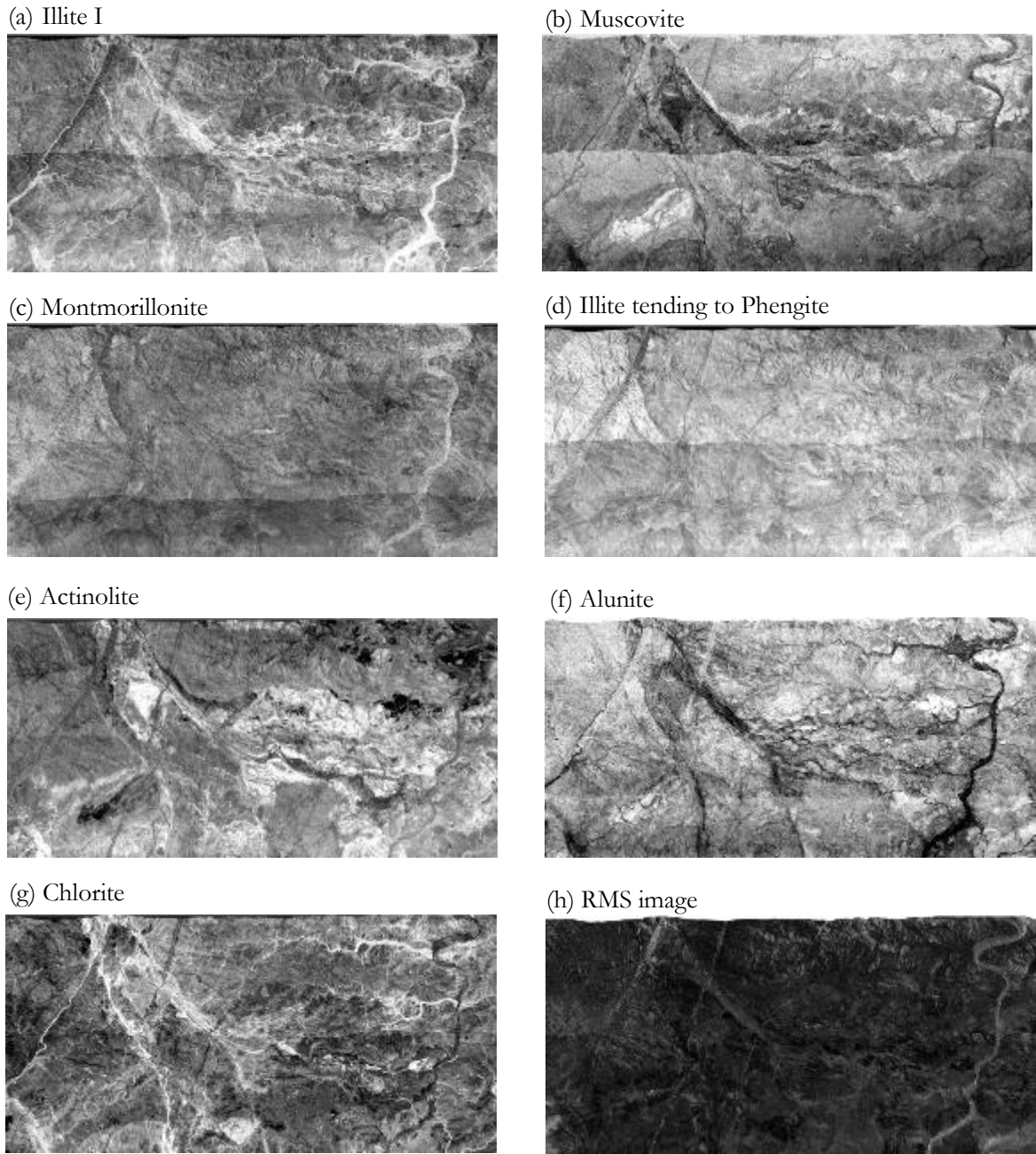


Figure 12. LSU Outputs images (a)-(g) abundance fraction (h) RMS image.

Table 1. Endmembers generated from the Hyperspectral data.

S/N	HyMap
1.	Muscovite
2.	Illite I
3.	Illite II (tending to Phengite)
4.	Montmorillonite II
5.	Chlorite
6.	Actinolite
7.	Epidote
8.	Alunite

4.8. Comparison of SAM with EnGeoMAP

The EnGeoMAP 2.0 algorithm was recently used to produce a mineral map of part of the Haib area (Mielke et al, 2016). The inferences reflected in the output images were compared with the SAM classification produced in this research. It was discovered from the expert system image classified the amphibolite unit as predominantly made up of calcite (Figure 13); this result differs from the output of SAM which brought out actinolite endmember (amphibole group). Although Gossan was also discovered by the used algorithm, it was not able to clarify if it was economic, false or barren type.

It is worth noting that goethite (brown), hematite (red) and limonite (yellow) minerals collectively known as gossan were noticed in the field, but this was not found associated with the box work texture which has never been reported in the area. It has been documented that not all gossans are of economic importance (Taylor and Eggleton, 2001).

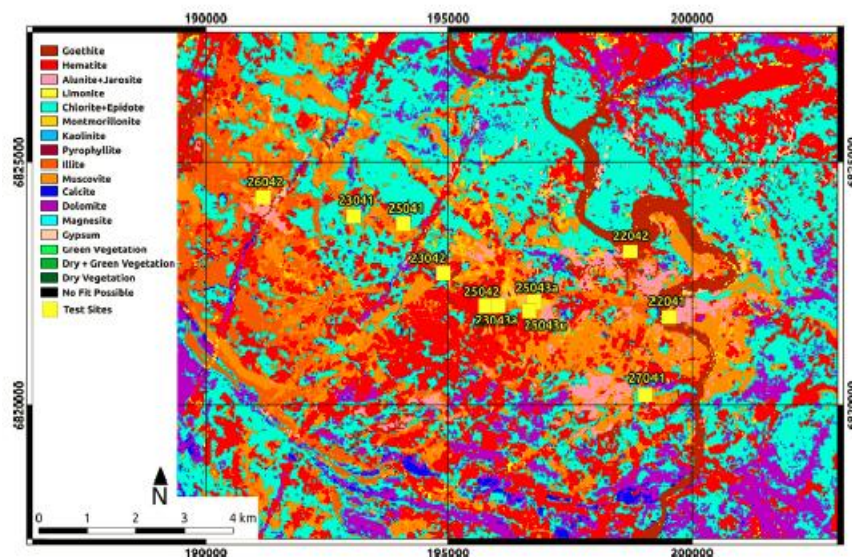


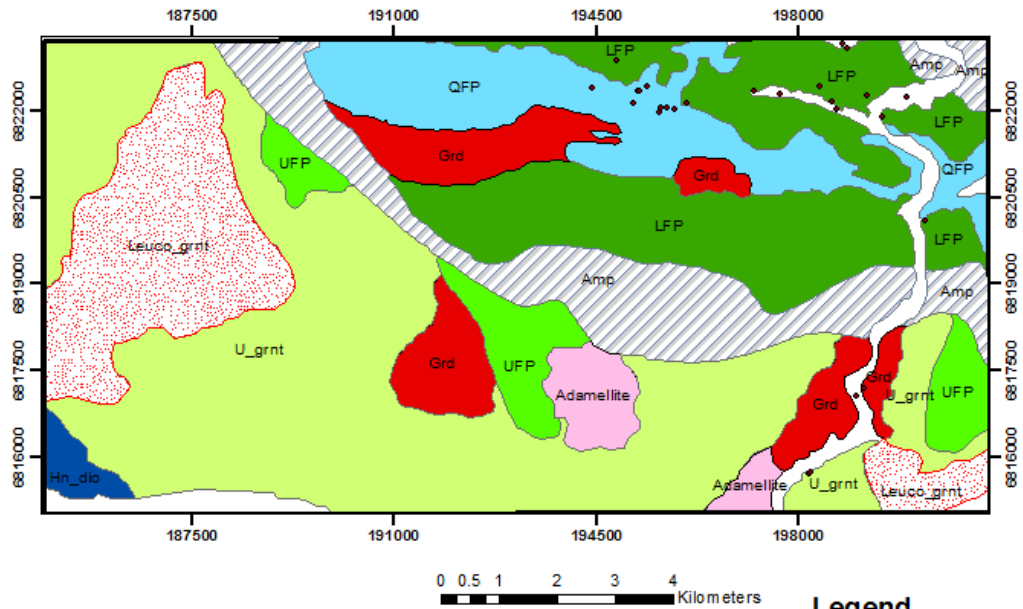
Figure 13. EnGeoMap 2.0 mineral map output (produced by Mielke et al, 2016).

4.9. The alteration mineralogy against the geology

The alteration minerals derived from the SAM supervised classification was draped over the geology to visualize rock relationship with alterations. The entire rock types as found in the area yielded different alteration minerals in variable proportions (Figure 14). A zoom in on blocks A and B summarises the spatial extent of the alterations with respect to the lithological units (Figure 15).

The quartz feldspar porphyry (QFP) was variably altered to montmorillonite, illite tending to phengite (ItP) and chlorite with some traces of muscovite and epidote; the lower feldspar porphyry (LFP) has ItP, chlorite, muscovite, illite I, montmorillonite and some actinolite; the upper feldspar porphyry (UFP) is basically altered to montmorillonite and actinolite with minor chlorite; granodiorite also shows montmorillonite, ItP, muscovite, some illite I, chlorite and epidote; amphibolite showed significantly actinolite, ItP and minor chlorite; while a greater portion of the leucogranite is more of montmorillonite with minor inclusions of ItP.

The mineralogical compositions of the rocks alongside the influence of the hydrothermal fluids have greatly contributed to the formation of the alteration minerals as detected within study area. Most of the rocks are enriched in both plagioclase feldspar and K-feldspar minerals in different proportions, the alteration of which produces complex mixtures of clay minerals and other silicate products. The ItP results from Mg-Fe substitutes for Al in the silicates to tend towards phengite.



Amp= Amphibolite, Grd= Granodiorite, Hn_dio= Hornblendite Diorite, LFP= Lower Feldspar Porphyry, Leuco_grnt= Leucocratic Granite, QFP= Quartz Feldspar Porphyry, UFP= Upper Feldspar Porphyry, U_grnt= Undifferentiated granitoid, Adamellite.

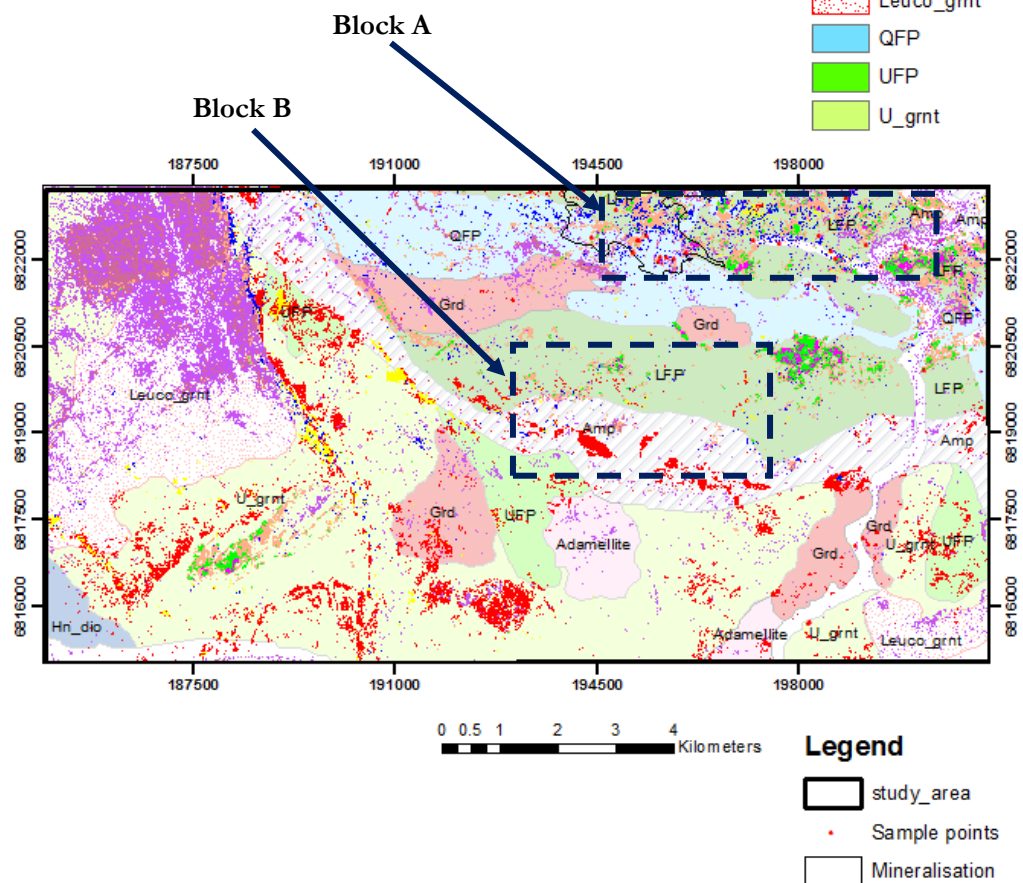


Figure 14. Mineral map on the geology (at 75% transparency).

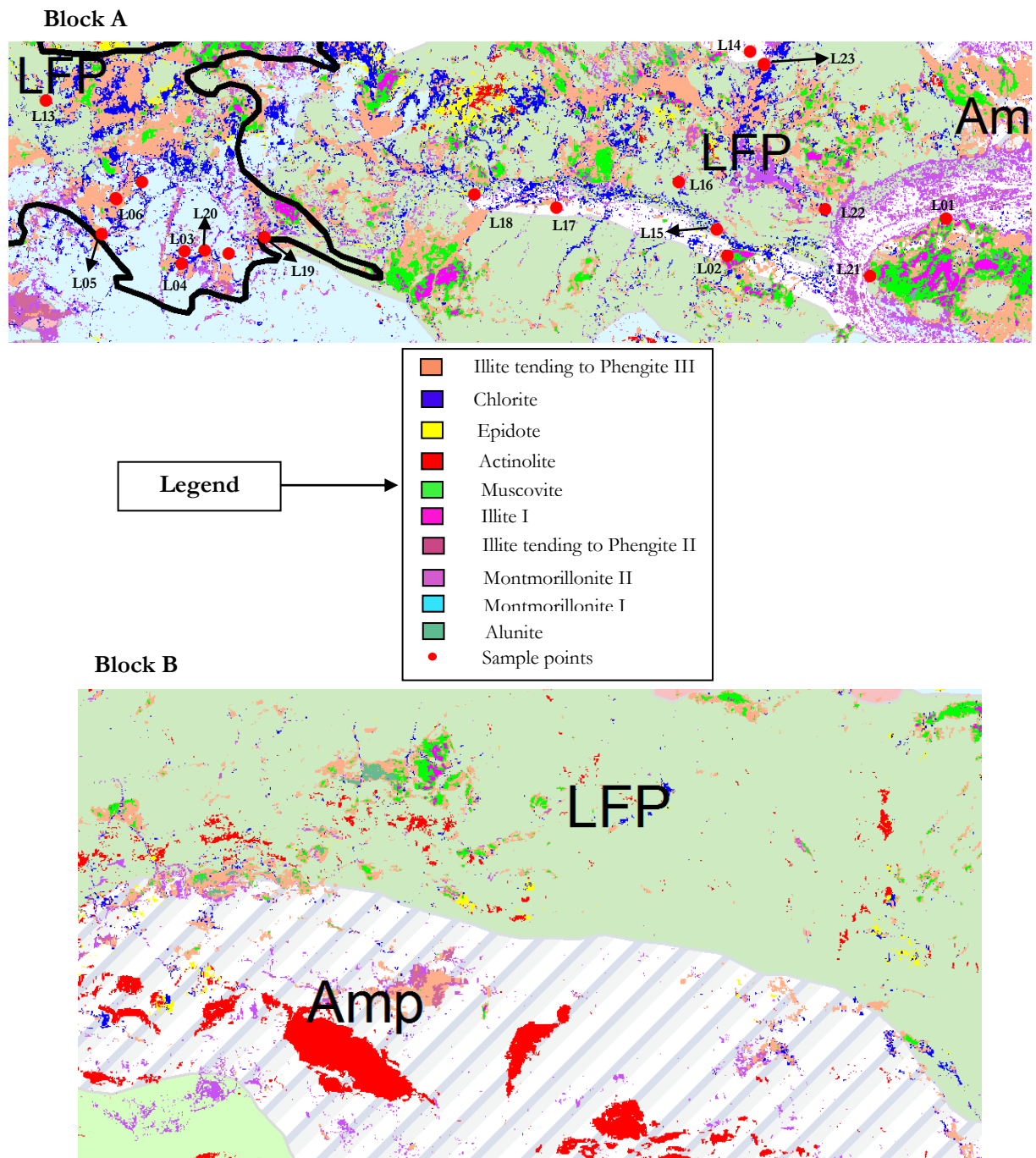


Figure 15. Blocks A and B subset view of the mineral map over geology.

4.10. Field reflectance data

4.10.1. Processing stage

The reflectance spectra data measured from some of the rock samples were indistinguishable due to the noise introduced during the data capturing phase. This prompted the subsection of the data into corrective operations aimed at enhancing the spectral signature. The smoothing algorithm was deployed to remove the noise. This was scaled by a factor of 5 and where applicable 10 depending on the extent of noise in the data being corrected. This is solely to ease and enable diagnosing the spectra. The proper identification of

the spectra was achieved by matching with the USGS spectral library and at the same time critically looking at the signature forms in tandem with the wavelength positions of absorption features. The GMEX Spectral interpretation field manual was of great use during this work. Complexly noisy portions of the wave signal were removed, for instance, channels 0 - 100, 388 - 504 and 976 - 1024 of the entire library was removed as a smoothing was applied (Figure 16).

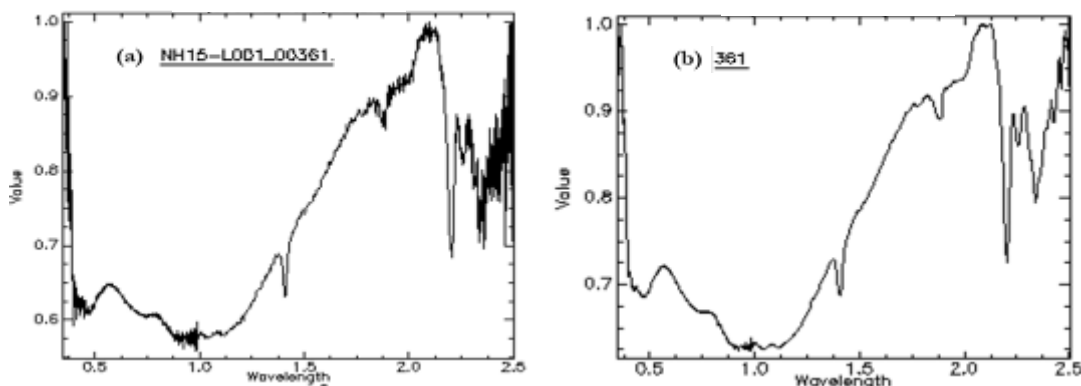


Figure 16. A typical field spectra (a) noisy (b) after correction (Msw - Muscovite + silica (water)).

4.11. Result from field reflectance data

The field reflectance data as acquired with the Spectral Evolution (SE) device was processed from noisy backgrounds and compiled in relation to the sample locations. On careful examination based on the distinguishable wavelength positions of deepest absorption features and also in association with other characteristic diagnostic features the spectra were named appropriately (Table 2). From the spectra analysis, the high crystallinity muscovite which tends to show spectral similarity with high crystallinity illite was detected, showing a signature pattern associated with silica plus water inclusions. The illite mineral found was categorised into two main types, the illite I and illite II. The illite I is characterised by its high crystallinity while the illite II is defined as the low crystallinity type. The index of demarcation between the two illite minerals is based on the sharpness of the AlOH feature in relation to the depth of the water feature at 1.9 μm ; high crystallinity is equated to shallow water depth feature as the AlOH signature sharpens down. This further led to the categorisation of the illite II class of minerals. The AlOH, H₂O and CO₃ features were used in the decomposition process, hence producing the Illite-Carbonate-Smectite (ICS), Illite tending to Phengite (ItP), Illite-Smectite-Carbonate (ISC) and Illite-Smectite (IS) minerals. The smectite group also showed variable association with CO₃ and AlOH features producing Smectite-Carbonate-Illite (SCI), Smectite-Illite (SI) and Smectite-Illite-Carbonate (SIC) minerals. Another class of smectite combination is the Carbonate-Illite-Smectite (CIS) mineral. The chlorite group is summarised into two types, namely the Mg-Fe type (m-f C) and the Mg type (m C). The Jarosite and the Epidote minerals were also detected and included with the spectral library.

All these minerals can be basically categorised under the alteration facies propylitic, argillic and phyllic. In other words, the potassic alteration mineral was not spectrally detected on the surface. The dominating illite mineral has its AlOH diagnostic absorption feature at wavelength range from 2.180 to 2.225 μm , where the lower wavelength end is more of the paragonitic or sodium rich illite, while the longer end is of the phengitic or iron-magnesium rich Illite. The paragonitic endmember was not detected from the field spectra. Intermediate to these two end members is the 2.20 μm normal potassic illite which shows similar composition to muscovite. A problem of illite looking spectrally similar to muscovite was encountered during the course of the mineralogical definition. In this case particularly, illite has a spectral match with

the silica + water rich muscovite. The illite mineral specifically demonstrated variation in crystallinity across the study area. This spectral analysis was able to differentiate the low crystallinity from the high type. Although the smectite spectrum is well identifiable with the water features at 1.4 μm and 1.9 μm , it displayed differential mixture with illite and carbonate minerals. Epidote which is characterised by features near 1.54 μm , 2.24 μm and 2.335 was of little occurrence from the spectral result. This is also applicable with chlorite, where the Mg-Fe Chlorite was distinguished with the 2.34 μm absorption feature. The Jarosite mineral was clearly revealed near the 2.26 μm wavelength position even as a perfect spectral match was found via the spectral library.

Table 2. List of alteration minerals detected from the Field samples.

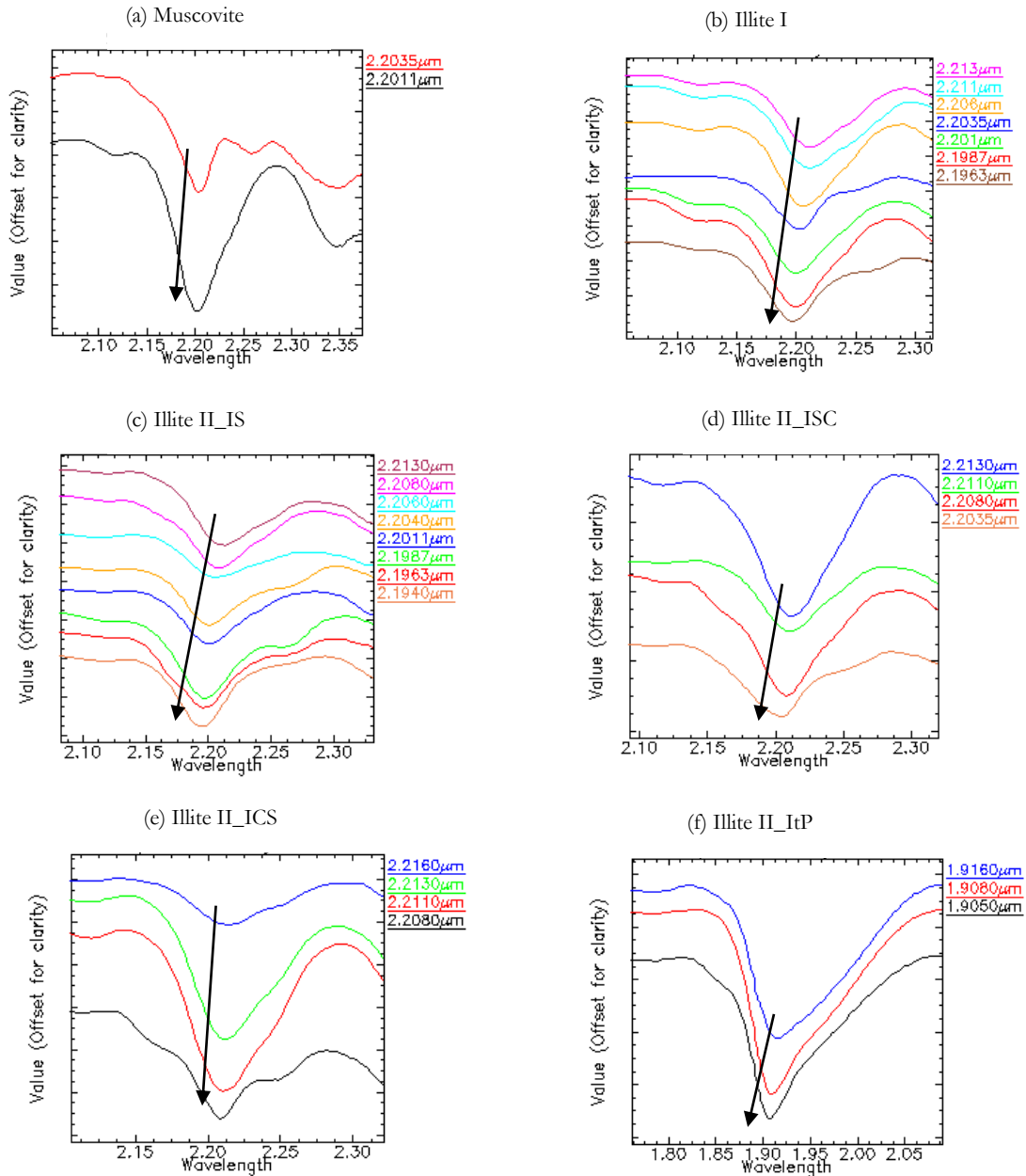
S/no.	Field Spectra	Code
1	Muscovite-Silica (water)	Msw
2	Illite I	Illite I
3	Illite II (Illite-Carbonate-Smectite)	Illite II_ICS
4	Illite II (Illite tending to Phengite)	Illite II_ItP
5	Illite II (Illite-Smectite-Carbonate)	Illite II_ISC
6	Illite II (Illite-Smectite)	Illite II_IS
7	Smectite-Carbonate-Illite	SCI
8	Smectite-Illite	SI
9	Smectite-Illite-Carbonate	SIC
10	Carbonate-Illite-Smectite	CIS
11	Mg-Fe Chlorite	m-f C
12	Mg Chlorite	m C
13	Jarosite	Jar
14	Epidote	Epi

4.12. Compositional variations in the field spectra

The field acquired spectra distinctly revealed compositional variations in the collected rock samples; this is reflected by the shift in the wavelength positions of the deepest absorption feature (Figure 17). All the alteration minerals displayed this quality at different intensities. The captured Muscovite displayed this compositional variation in two (2) different wavelength positions (Figure 17a). It varies from the shorter wavelength position 2.2011 μm to the longer end member 2.2035 μm . Illite I which exhibited high crystallinity also shows this wavelength shift from 2.1963 – 2.2130 μm (Figure 17b). In the illite II category of minerals, herein referred to as the low crystallinity illite, revealed shift positions in Illite-Smectite (IS) from 2.1940 – 2.2130 μm ; ISC showed a shift from 2.2035 – 2.2130 μm ; ICS from 2.2080 – 2.2160 μm ; although the ItP AlOH feature position maintained at 2.2100 μm for illite tending to phengite based on Mg-Fe substitution, the deepest H₂O feature at 1.900 μm displayed positional shifts from 1.9050 – 1.9160 μm (Figure 17c-f). The smectite group members also exhibited positional shift in wavelength, although at times within close ranges: SCI (1.9050 – 1.9080 μm), SI (1.9070 – 1.9400 μm) and SIC (1.9050 – 1.9270 μm) (Figure 16k-m). Jarosite (2.2610 – 2.2680 μm), epidote (2.3300 – 2.3370 μm), Mg-Fe chlorite (2.3300 – 2.3400 μm), Mg chlorite (2.3020 – 2.3230 μm) and CIS (2.3400 – 2.3450 μm) still maintained this shifting trends which has a lot to do with the intensity of alterations in the study area (Figure 17a-n).

4.13. Coverage of spectra datasets

The apparent reflectance output of the HyMap summarises the entire four (4) scenes of the study area, the sampling points obtained from field mapping represented spectral data from the mineralisation region (upper north-central, marginal to the north-east quadrangle of the study area); this also extends from the north-east flank down through the accessible dry drainage path to the southern axis where it terminates at the Orange River. This river actually demarcates the Namibian country from the Republic of South Africa. The major limitation associated with obtaining the field spectra data is the rugged and extremely high topographic features dominating the area, from the central to the south-western parts.



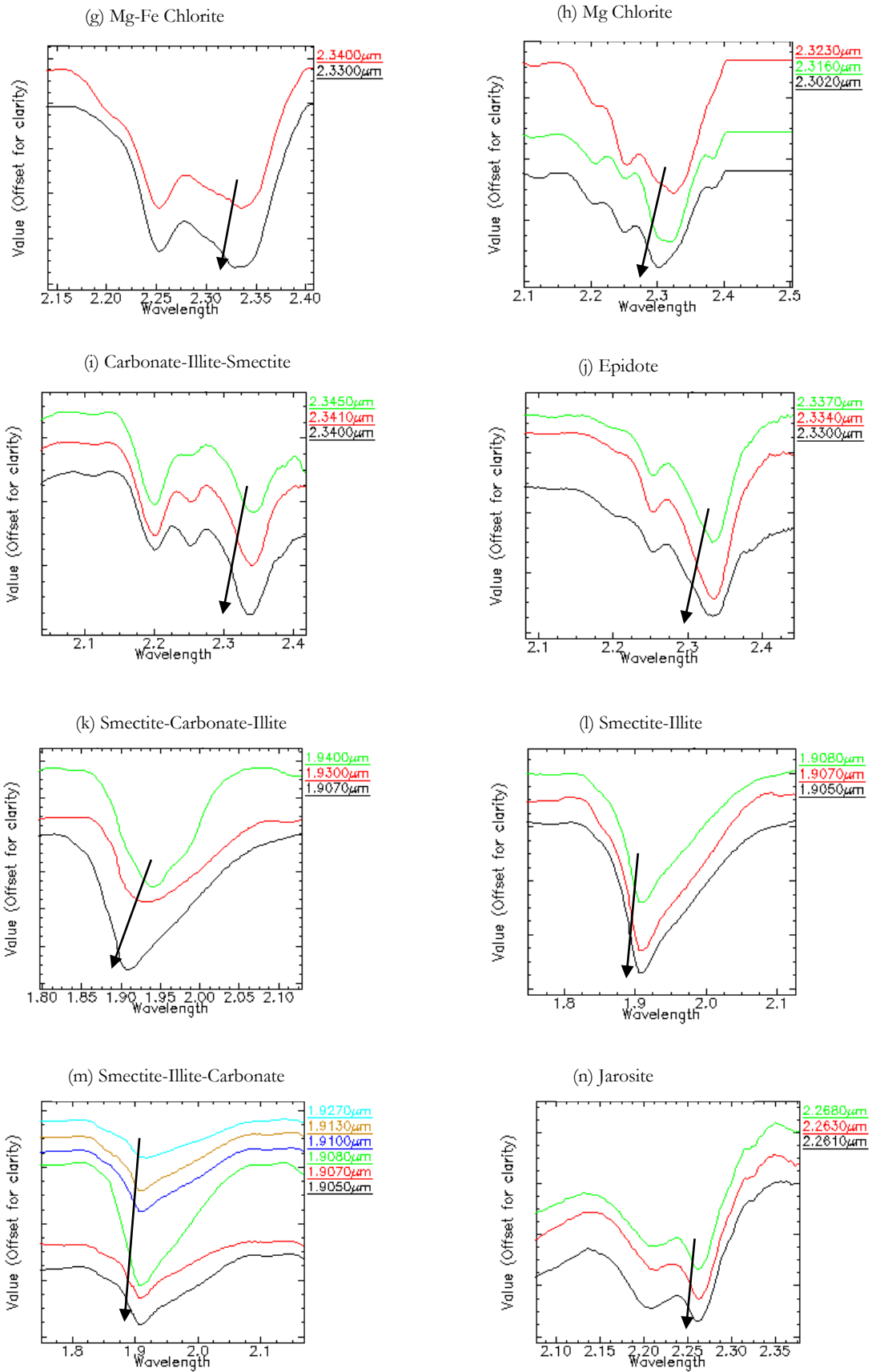


Figure 17. The wavelength position shift pattern in the alteration minerals acquired from the field spectra (a) – (n).

The alteration minerals detected from the sampled points gave more details when compared with the hyperspectral imagery. Apart from the fact that the resolution of the SE device was on a much finer scale, another dimension of data capture was included. This output is further summarised with respect to the sample locations and the mineralisation zone (Table 3).

Table 3. Summary of field alteration minerals with respect to their locations.

		ALTERATION MINERALS													
		Illite I	Msw	Illite II_JCS	Illite II_IS	Illite II_ISC	Illite II_IrP	SCI	SI	SIC	Jar	Epi	m-f Chl	m Chl	CIS
SAMPLE POINTS	L1	X	X		X	X									
	L2	X													
	L3							X		X					
	L4			X					X	X					
	L5			X		X				X					
	L6					X	X			X					
	L7													X	
	L8												X		
	L9			X											
	L10														X
	L11											X			
	L12			X		X	X								
	L13	X		X											
	L14	X			X										
	L15				X										
	L16											X			
	L17				X										
	L18				X										
	L19	X													
	L20														
	L21	X			X					X					
	L22	X	X		X										
	L23				X	X									

Legend

	Undetected Alteration Mineral
X	Detected Alteration Mineral
X	Detected alteration mineral associated with Cu mineralisation zone

4.14. Graphical Analysis of the field spectra

A summary of the wavelength position shifts by the endmembers generated from the reflectance field data is graphically represented. The range of shift in the wavelength positions of deepest absorption feature is used with respect to the alteration mineral (Figure 18). This can be related to the extent of compositional variation across the study area, but that is beyond the scope of this work.

4.15. Geochemistry

The field spectra were compared with the geochemical data measured with the XRF device. The concentrations of the radioelements (K, Th and U), Fe and Cu were considered in this research to further understand K distribution patterns with respect to the alteration minerals. The concentration of K is seen as high in the illite minerals when compared with other alterations (Figure 19). The highest value is found in the low crystallinity Illite (Illite-Carbonate-Smectite), while the lowest value is found in the Jarosite. It is also observed that the mean concentration of K in the Illite minerals is higher than the highest value of other alterations. The Illites, muscovite and smectite group of minerals generally show significant radioelement concentrations even as Jarosite, Chlorite, Epidote and Carbonate-Illite-Smectite show no record of some radioelements such as thorium (Figure 20). This pattern of signature is also repeated in the

uranium distribution in the mapped area (Figure 21). The distribution of Fe was also studied in the alterations and discovered to be of significant spread in the Illite tending to Phengite (ItP) as the rock gets more enriched in Mg-Fe, making it more Phengitic. The Smectite-Illite (SI) exhibited the greatest spread and highest concentration in Fe (Figure 22).

It is worth noting here that the mineral map makes use of the absorption features of alteration minerals (materials) in its discrimination; an understandable pixel image is therefore produced when the spatial information is incorporated with it. The radioelement distribution map relies on the elemental concentrations as it relates to the underlying rock unit.

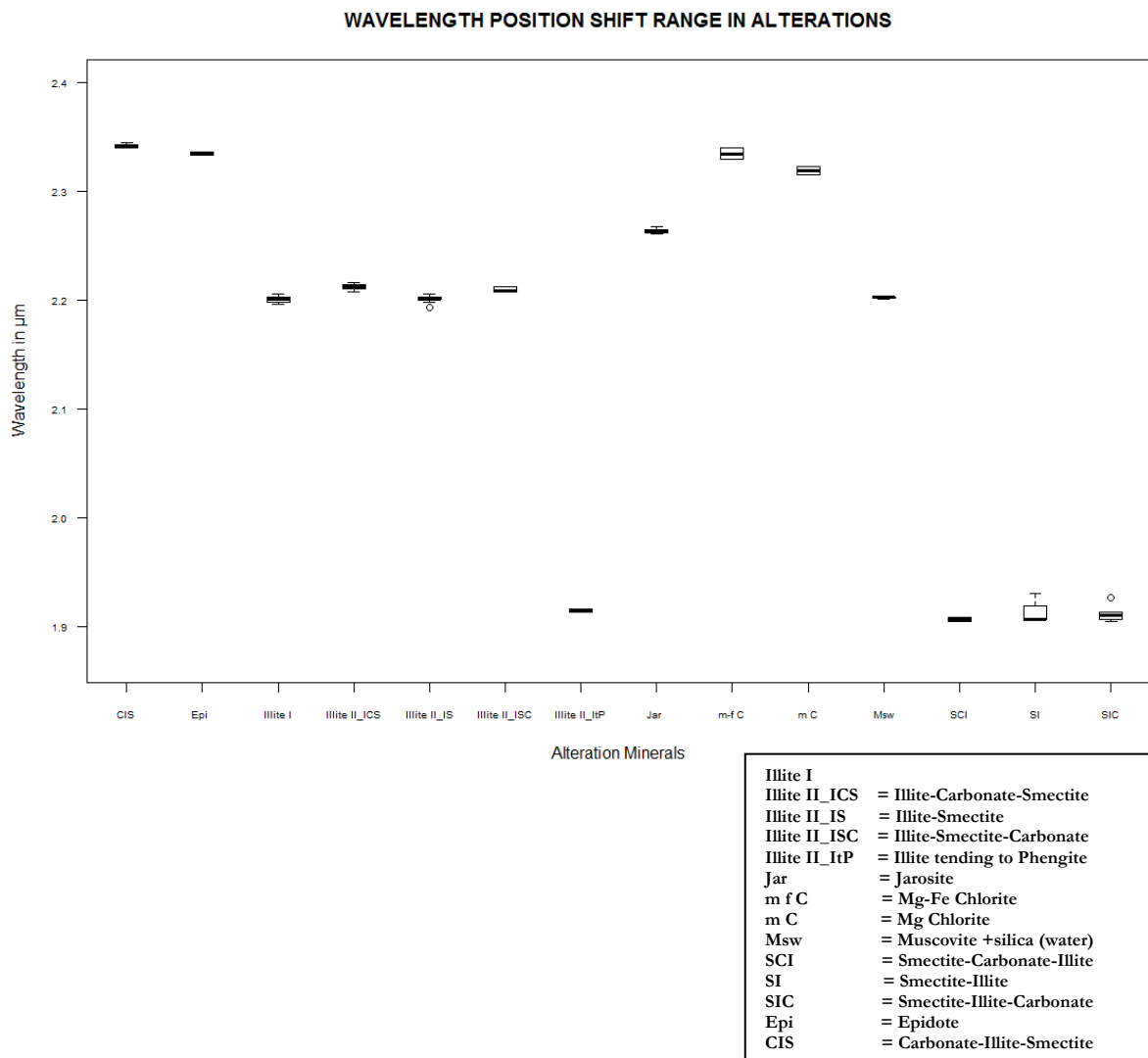


Figure 18. Wavelength position shift range against alteration minerals.

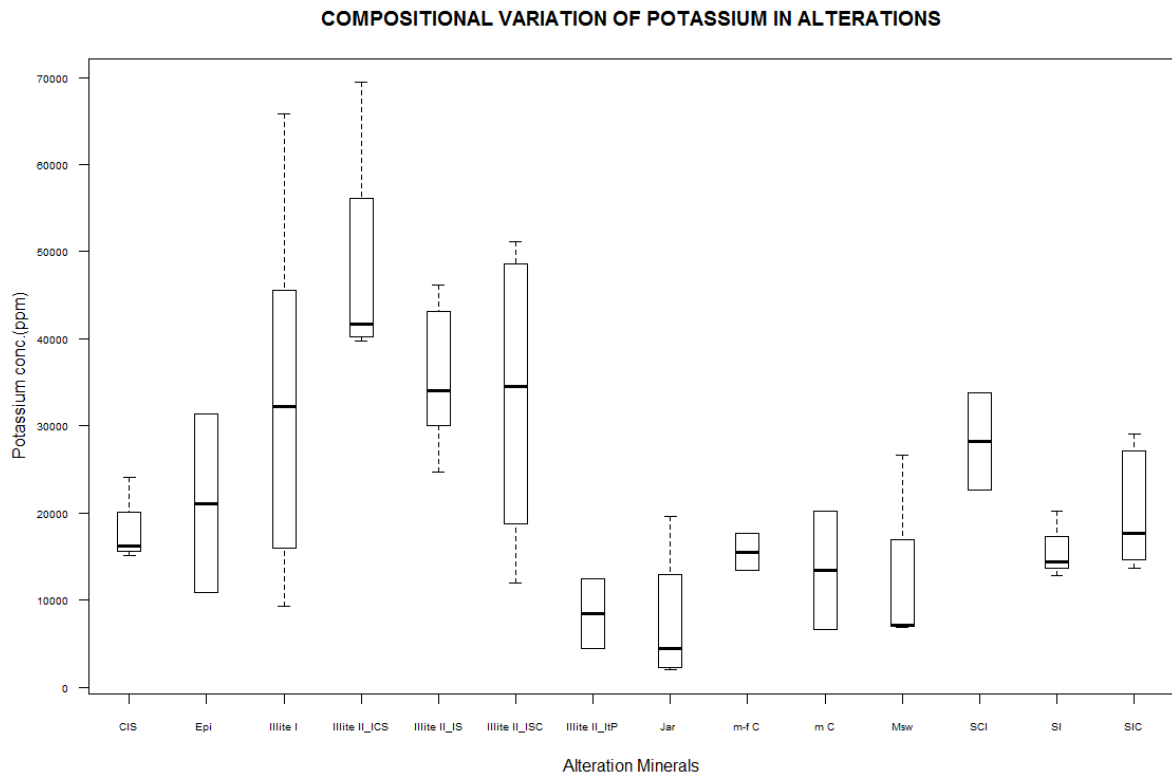


Figure 19. Potassium concentration across alteration zones.

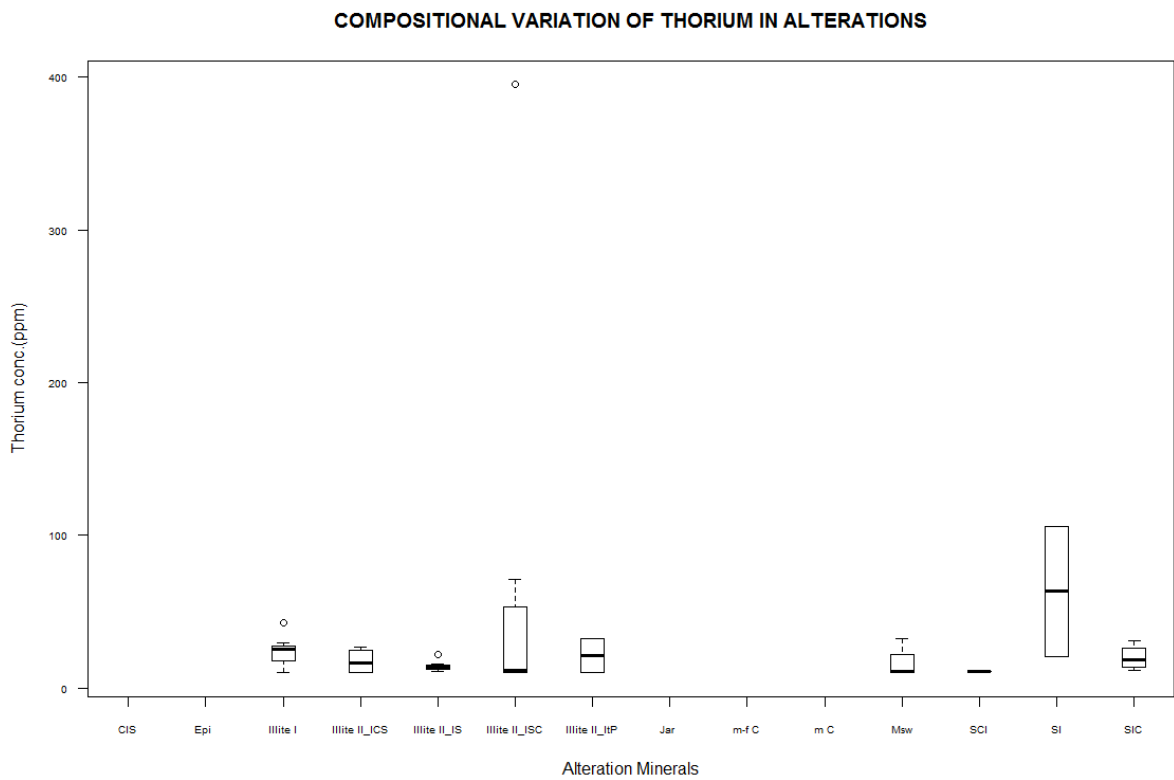


Figure 20. Thorium concentration across alteration zones.

COMPOSITIONAL VARIATION OF URANIUM IN ALTERATIONS

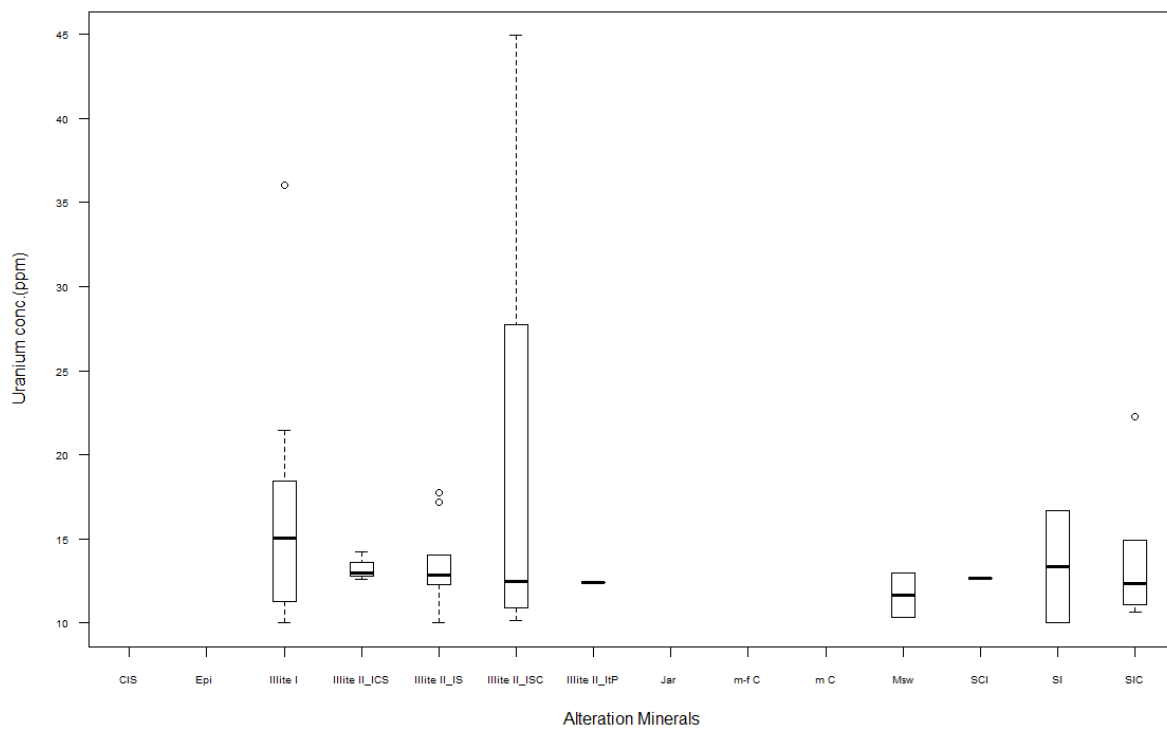


Figure 21. Uranium concentration across alteration zones.

COMPOSITIONAL VARIATION OF IRON IN ALTERATIONS

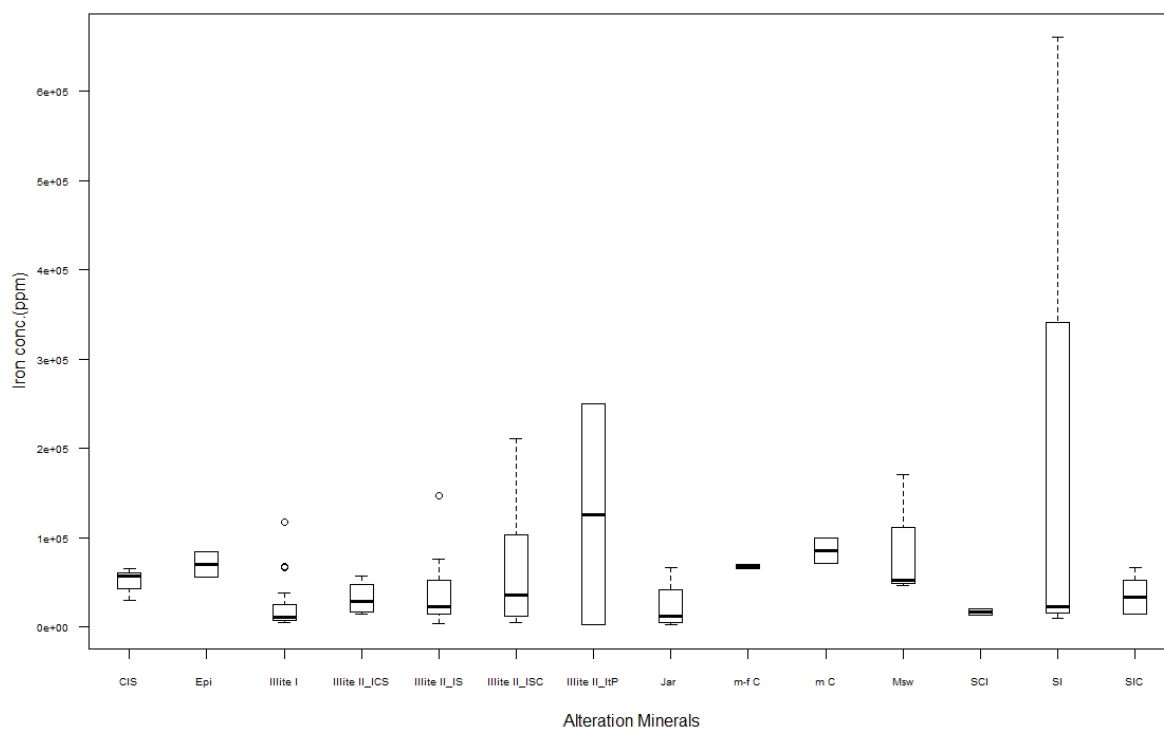


Figure 22. Iron concentration across alteration zones.

The copper concentration was also investigated and found to be pronouncedly related to the smectite group, most of the low crystallinity illites minerals except the IS. Also interestingly, the illite I shows no association with Cu mineralisation (Figure 23).

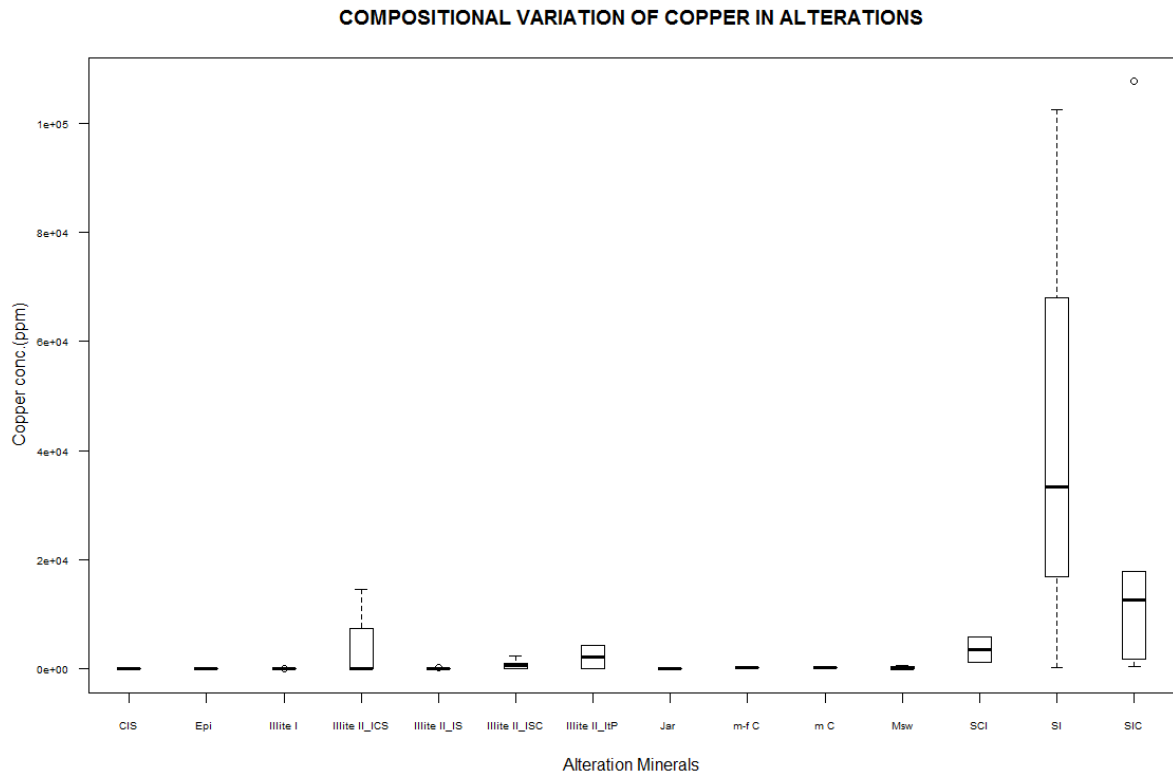


Figure 23. Copper concentration across alteration zones.

4.16. Metamorphic grade

The minerals extracted from the HyMap imagery and the field spectra were studied to further decipher how they relate with metamorphism in the terrane. An idea of the prevalent pressure and temperature conditions during the emplacement of the rock can easily be known by detecting some specific minerals. Using the subset views (Blocks A and B) as portrayed in figure 14, actinolite and epidote displayed low pixelation north of the Volstruis creek, with the epidote displaying minute cluster near the northern margin of the mineralisation. Chlorite seems to be ubiquitous within block A, found along, north of creek and within mineralisation zone. Patches of muscovite are also occurring within mineralisation zone. As already stated, the wider spatial coverage HyMap mapped the actinolite, chlorite, muscovite and epidote while the field reflectance inclusively captured Jarosite in its fourteen (14) endmembers list. The enrichment of rocks with this class of minerals is indicative of low to medium grade metamorphism (Berry et al, 2004). This mineral assemblage has been described and equated to the propylitic hydrothermal alteration in the Haib (Minnitt, 1986).

5. CHAPTER FIVE

5.1. Radiometric data and result presentation

5.1.1. Introduction

In recent times, the paucity of valued geochemical data to analyse the compositional variations of the earth surface is a vacuum in the field of geochemistry (Darnley, 1996). The gamma ray spectrometric data constitutes an important component needed in carrying out geochemical surveys.

It has been summarised that the top 30cm of the surface of the earth is always subjected to the influence of agents of denudation. This tends to cause weathering which leads to variation in the concentration of radioelements such as potassium (K), uranium (U) and thorium (Th). These elements are lost in all rock types when undergoing this surficial process (Dickson and Scott, 1997). The signatures resulting from these geochemical variations are easily detected by airborne gamma-ray mapping technique. This research is focused on potassium and the influence of hydrothermal alterations which increases its content in rocks associated with porphyry copper mineralisation. The alteration pattern in the Haib is further studied by integrating the radiometric data with the hyperspectral imagery result.

The airborne gamma-ray survey was flown in a north-south direction and 83 flight lines actually covered the study area while 4 tie-lines are in the east-west direction. The flight height of the survey was 80m. The measurement of the spectrometric data is achieved by observing four (4) spectral windows which are centred on the 1.46 MeV, 1.76 MeV and 2.61 MeV photopeaks, representing potassium (K), uranium (U) and thorium (Th) respectively (Figure 24). For the radiometric data to be useful for analysis, appropriate corrections were done on the raw data. Basically, at the initial stage of the corrections, the radio-elemental count is obtained after adjusting the dead time, energy drift and background radiation (Minty et al, 1997). These count rates are eventually reduced to the actual concentration on the ground by correcting for detector terrain clearance variations. These corrections have already been done to the raw data before its acquisition for this research.

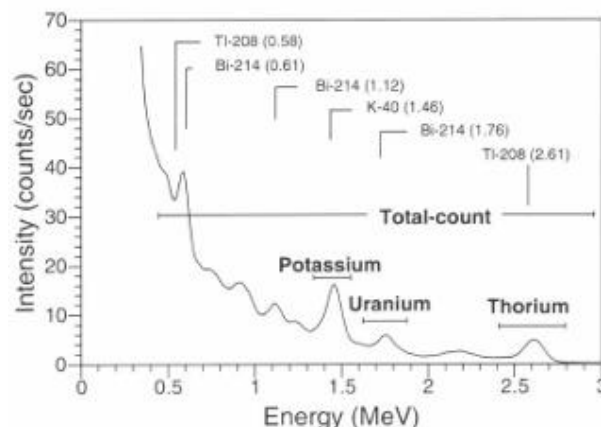


Figure 24. The conventional four (4) spectral windows and photopeaks used in airborne gamma-ray spectrometer (modified after IAEA, 1991).

5.2. Geochemistry of Radioelements

Potassium is a monovalent and volatile element under normal atmospheric conditions. Its average abundance is about 2.3 wt% in the upper crust of the earth, occurring mostly as alkali feldspar and micas in granitoids, and having an average of 3.5 wt. %. It is always found to be of a low concentration in mafic

and ultramafic rocks varying from 0.58 – 0.75%. The categories of rocks majorly harbouring K in metamorphic rocks include the feldsparoids (leucite and nepheline), feldspar mineral series and micas biotite and muscovite. Hornblende also contains about 1 wt.% K (IAEA, 2003).

Thorium tends to occur naturally as an actinide which gets easily dissolved in acid solutions; having a very low average abundance of about 12 ppm in the crust. It usually occurs as accessory minerals along with monazite, zircon, apatite, sphene, etc (IAEA, 2003).

The average crustal abundance of uranium ranges between 2-3 ppm. It has similar crystallo-chemical properties with thorium and Light Rare Earth Elements (LREE), which explains their coherent chemistry in igneous rock units (Bea, 1999). This affinity is disrupted under surficial weathering process and hydrothermal conditions where uranium is oxidized either completely or partially to U^{6+} , forming soluble complexes with carbonate, sulphate and phosphate anions (Langmuir and Hermans, 1980).

5.3. Methodology

The procedural approach in the analysis of this data is divided into: Data presentation and enhancement, Data integration, Anomaly identification and Interpretation and result synthesis. A flow chart summarising this steps is found below (Figure 25).

- (a) **Data Presentation and Enhancement:** This stage enabled the creation of the ternary map using the three (3) radioelements (K, Th and U) to reflect their compositional variation in the different rock types that make up the study area. The K distribution as it characterises the area was also produced using the gridding tool. A typical stacked airborne gamma ray spectrometric profile showing the discrimination patterns between the radioelements was constructed.
- (b) **Data Integration:** In order to obtain a logically acceptable result output, the radiometric data is never interpreted independently; hence, its integration with other complementary datasets is inevitable. The output of the data enhancement stage is incomplete without the geological dataset. In other words, the compositional variation in radioelement concentrations is related with the underlying geology. The visual interpretation of different combination was carefully studied for better inference.
- (c) **Data Interpretation and Result Synthesis:** The final interpretation and synthesis of the radiometric data is done after incorporating the field acquired XRF complementary dataset which highlights the anomaly related aspect of the composite datasets.

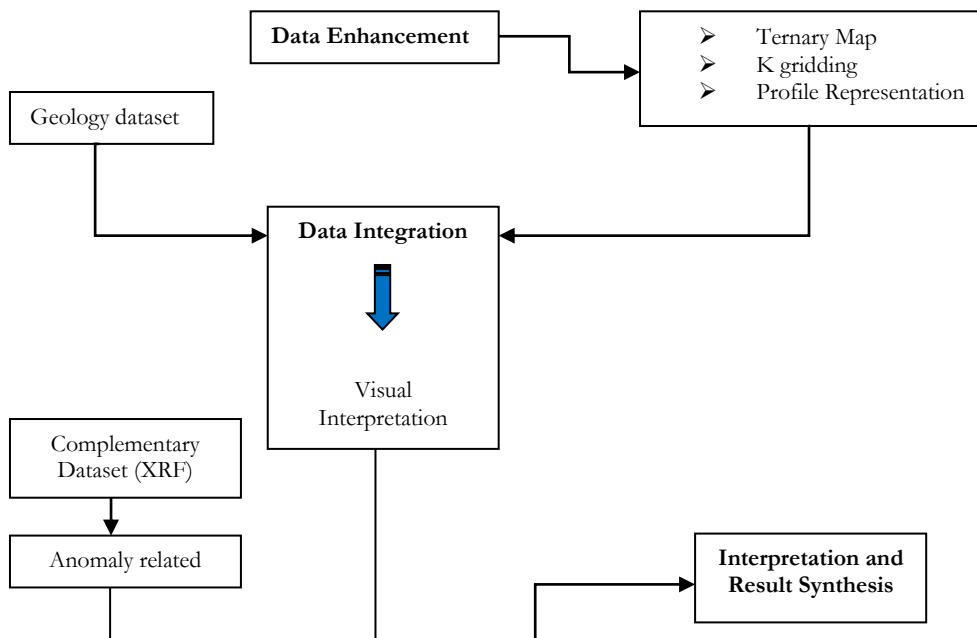


Figure 25. Flow chart on the radiometric data methodology.

5.3.1. Data presentation and Enhancement

The Red, Green and Blue (RGB) colour ramp was used to produce the ternary image proportionate to the radioelement concentration values. It was also draped with the geological map using the geological boundary across the study area (Figure 26). This tends to show some similarities between the radioelements distribution and the lithological units. The combination of the three (3) radioelements tends to reveal compositional variation patterns in the rock types. This results from the differences in concentration of the radioelements as they tend to vary with rock type. The potassium concentration distribution map across study area is shown in figure 27.

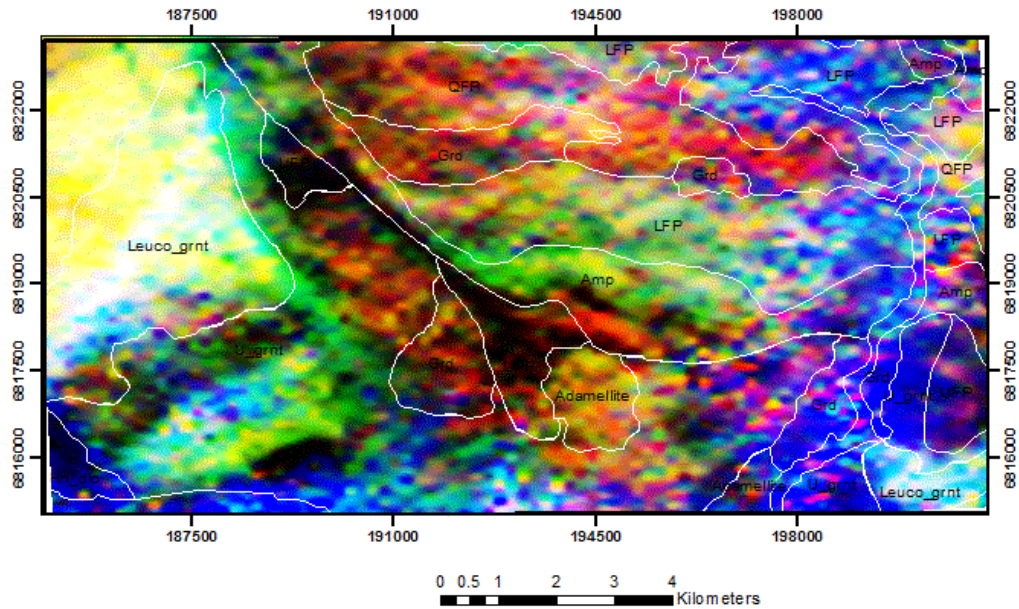


Figure 26. Ternary image draped with the geological boundary of the study area.

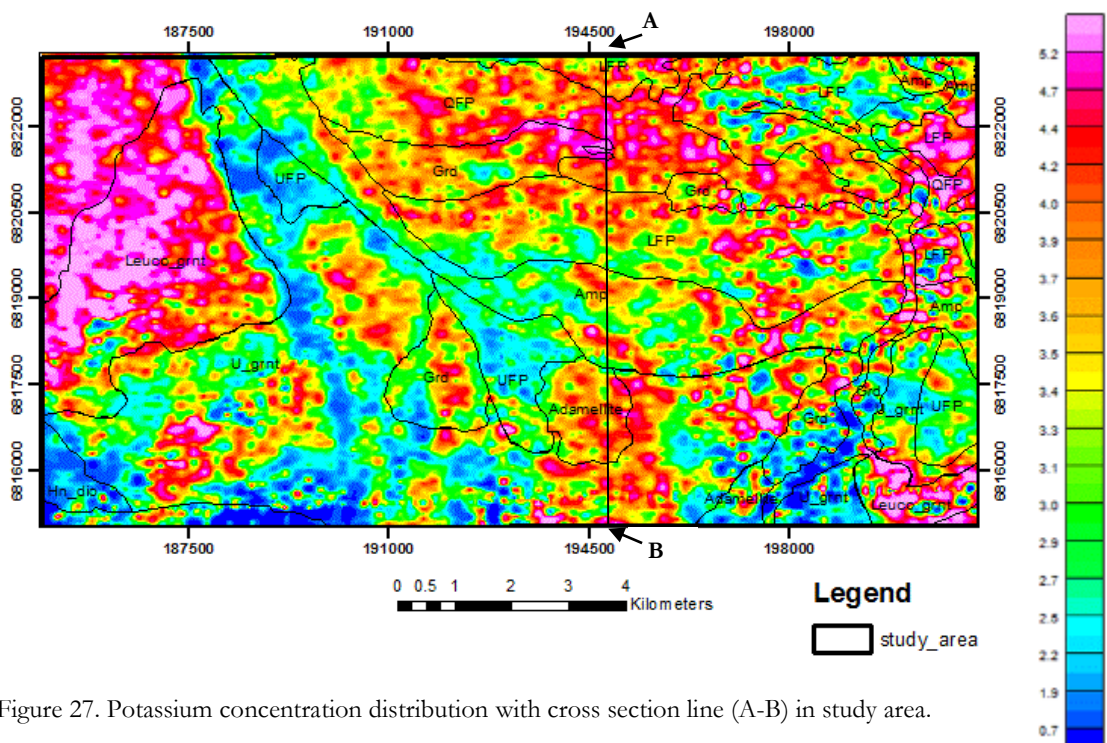


Figure 27. Potassium concentration distribution with cross section line (A-B) in study area.

The concentration distribution of potassium in the rock types was calculated with the zonal statistics tool in the ArcMap platform, by draping the geologic boundary over the potassium radiometric raster image. This evaluated the potassium content as it varies in the different rock units found in the study area (Table 4). The highest K concentration occurs in the amphibolite which extends from the north-west quadrangle through the central portion towards the east although disrupted by the Haib river channel (Figure 27). The overall concentration distribution of the element is graphically represented in figure 28; from this output, the majority of the values are well distributed in the undifferentiated granitoids. The average ranges in values reflected in the separate rock units reveal a significant overlap, which fully supports that from the global point of view the use of radioelement content for classification is not possible (IAEA, 2003). The geological setting in the area tends to portray a prevalent co-genetic magmatic source. Thorium has its highest concentration in the leucocratic granite as it shows a more distinctive variation pattern from other rock units; having also some significant spread of values in the undifferentiated granitoids (Figure 29). K also shows significant concentration in the leucocratic granite (Figure 28) as well as uranium (Figure 30). The summary statistics table for the airborne gamma ray data is presented in Appendix III.

Table 4. Zonal statistical summary result on the airborne gamma ray data concentration of potassium in the rock units.

S/N	Rock type	Min	Max	Range	Mean	St. D.
1	QFP	-0.54	6.83	7.37	3.86	0.67
2	Grd	-4.06	6.49	10.55	3.44	0.89
3	LFP	-0.48	8.51	8.99	3.51	0.74
4	UFP	1.10	6.38	5.28	2.66	0.58
5	Amp	0.47	9.39	8.91	3.29	0.74
6	U_grnt	-3.27	8.04	11.31	3.21	1.12
7	Leuco_grnt	-2.33	8.65	10.98	4.47	1.12
8	Adamellite	-1.79	5.70	7.49	3.42	0.83
9	Hn_dio	-0.96	4.93	5.89	1.86	0.66

Amp= Amphibolite, **Grd**= Granodiorite, **Hn_dio**= Hornblendite Diorite, **LFP**= Lower Feldspar Porphyry, **Leuco_grnt**= Leucocratic Granite, **QFP**= Quartz Feldspar Porphyry, **UFP**= Upper Feldspar Porphyry, **U_grnt**= Undifferentiated granitoid, Adamellite.

POTASSIUM VARIATION IN ROCK UNITS

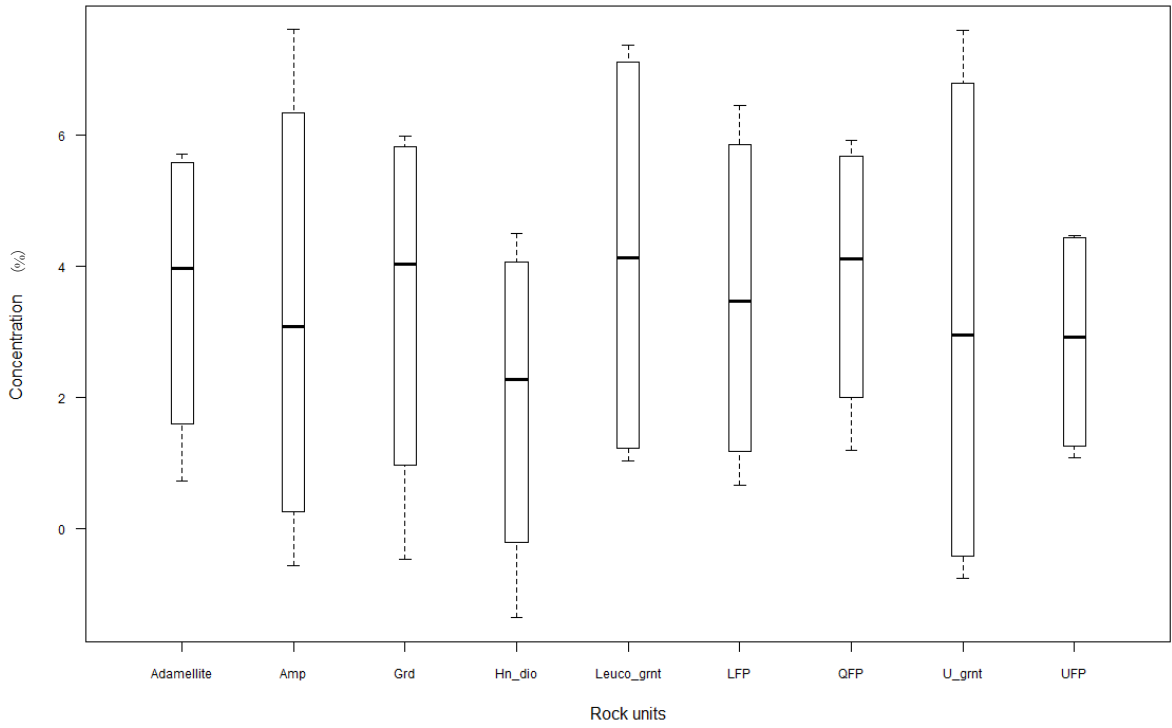


Figure 28. Variation in potassium across geology. Amp= Amphibolite, Grd= Granodiorite, Hn_dio= Hornblendite Diorite, LFP= Lower Feldspar Porphyry, Leuco_grnt= Leucocratic Granite, QFP= Quartz Feldspar Porphyry, UFP= Upper Feldspar Porphyry, U_grnt= Undifferentiated granitoid, Adamellite.

THORIUM VARIATION IN ROCK UNITS

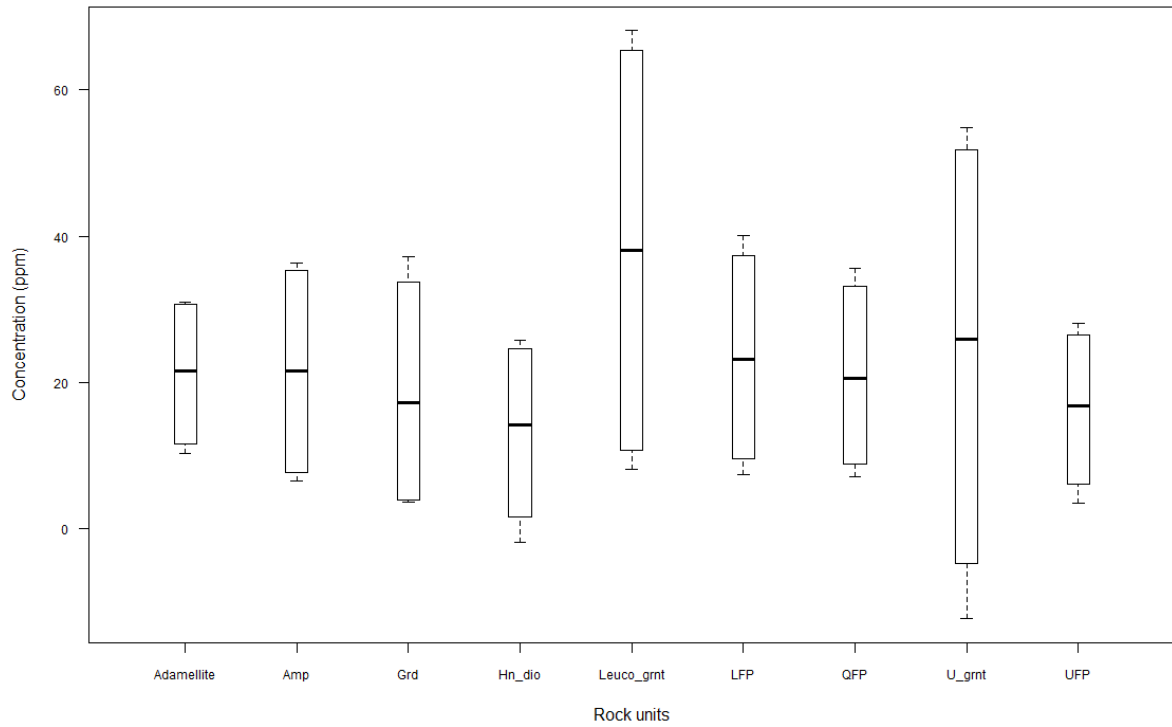


Figure 29. Variation of thorium across geology.

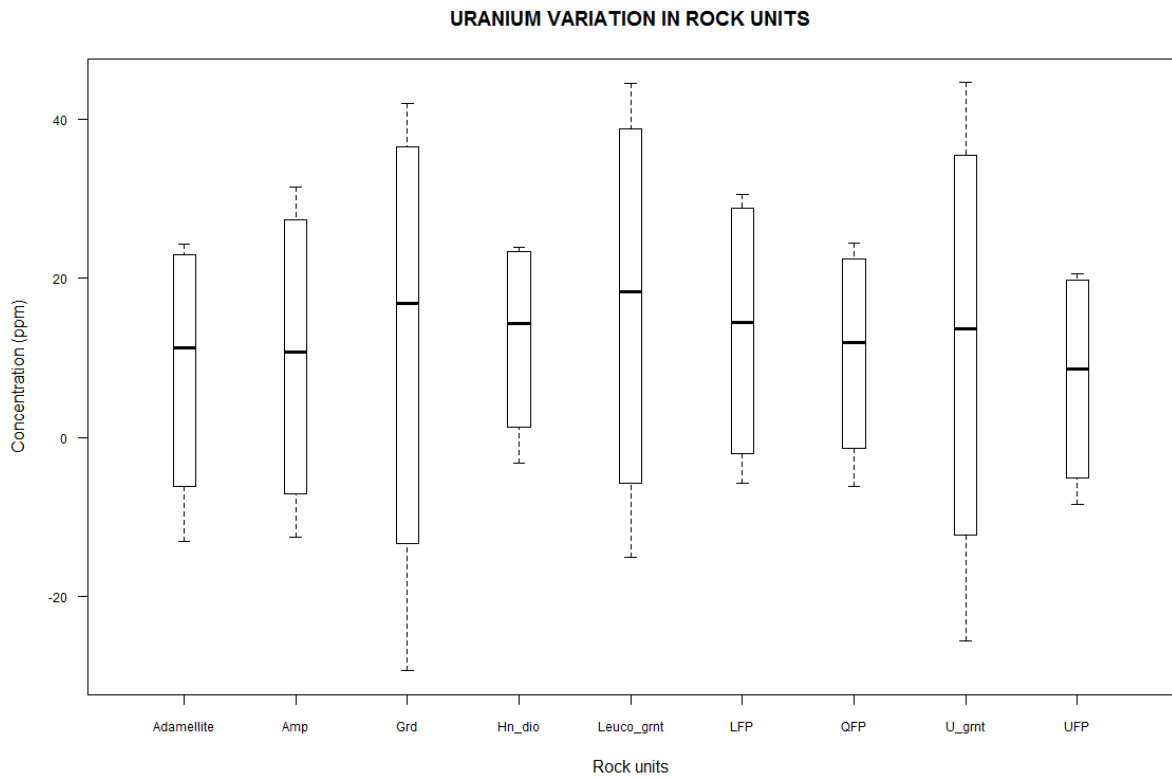


Figure 30. Variation of uranium across geology. Amp= Amphibolite, Grd= Granodiorite, Hn_dio= Hornblendite Diorite, LFP= Lower Feldspar Porphyry, Leuco_grnt= Leucocratic Granite, QFP= Quartz Feldspar Porphyry, UFP= Upper Feldspar Porphyry, U_grnt= Undifferentiated granitoid, Adamellite.

The radioelements concentration variance pattern across different rock units were compared using a stacked profiles (figure 31). The cross-section line A-B as shown in figure 27 is parallel and geospatially located on part of the flight line 374320 running in a north-south direction of study area. The variance between K, Th and U is also related with the topographic relief along this path. The QFP and the granodiorite reflected the highest K concentration while the amphibolite recorded the least concentration along this profile. Th and U also tend to show slight similarity with K concentration across the rock in this profile, although there are different peaking points.

Cross-section A - B

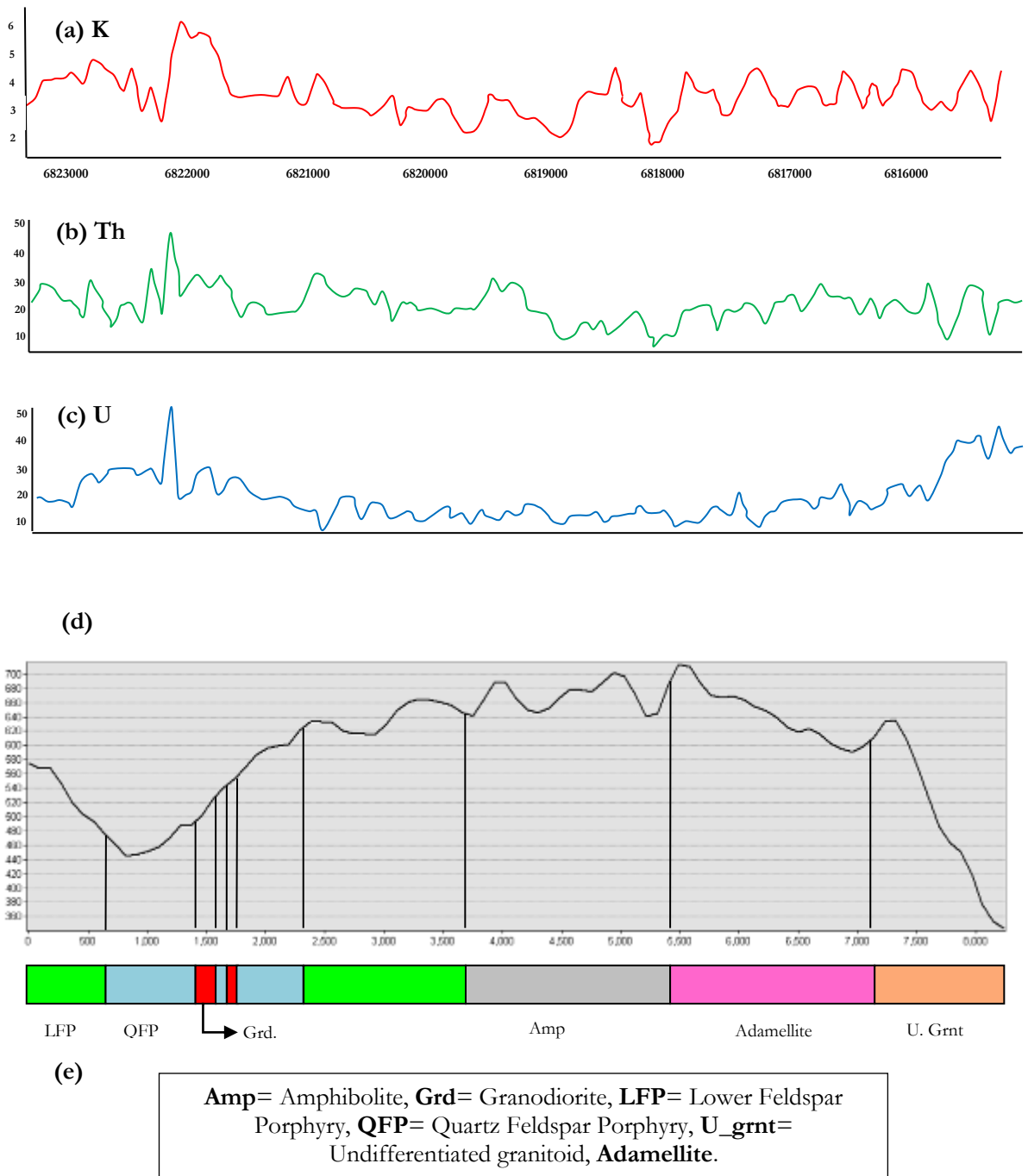


Figure 31. Stacked profiles orienting from north-south of study area (a) Potassium airborne gamma data concentration variation along flight line 374320 (cross section A-B in figure 5.4) (b) Thorium concentration (c) Uranium concentration (d) topographical relief.

5.3.2. Data integration

(a) Geochemical data with XRF

In an attempt to detect anomalous values due to the high K concentrations, the statistical approach was deployed in relating K with Cu. Already Cu has shown some remarkable variation trends in some alteration zones (Figure 23). A linear relationship test is further used to assess the correlation between K and Cu. The correlation calculation of Cu against K resulted in a value of -0.16 according to Pearson's method. This is viewed in the scatter plot of Cu against K (Figure 32) below; hence, there is no correlation between Cu and K. The samples were re-examined based on their Cu and corresponding K concentrations (Table 5). The result showed that Cu concentration value of ~668ppm and above fall within the mineralisation zone (Table 5). The highest concentration of copper (NH15-L04c) with a value ~10% plotted within the delineated mineralisation zone as seen in figure 33. This zone overlaps part of the Volstruis creek and extends to the northern flank. The L04c concentration is associated with a potassium concentration of ~1.9% while location 3 (NH15-L03c) with a Cu percentage equivalent to 0.5%, had K content of ~2.3%; this further confirms the non-correlation in concentration between Cu and K within the study area. Further evidence supporting this statement is repeated in the table, sample NH15-L06a which reflects a Cu content of about 0.07% and a K content ~3.7%, also plotting within the same mineralised region. The scatter plot was further modified by converting concentration values to logarithmic form purposely to cluster all sample points that plot within the mineralisation zone (Figure 33).

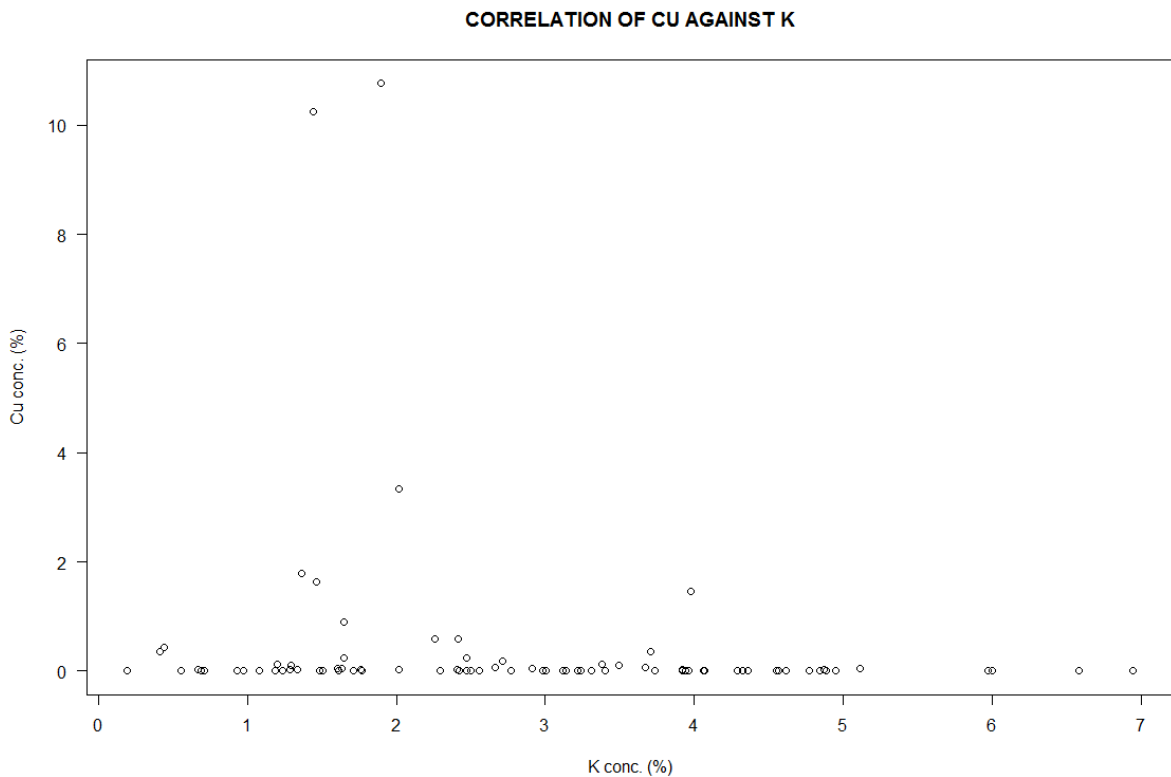


Figure 32. The non-correlation relationship between Cu and K.

Table 5. Variation in the concentration of the Copper with respect to Potassium over the Mineralisation zone.

S/N	LOCATION /SAMPLE CODE	Cu (ppm)	K (ppm)
1.	NH15-L04c	107593.70	18947.37
2.	NH15-L04b	102447.10	14435.01
3.	NH15-L04a	33411.81	20192.07
4.	NH15-L03b	17854.59	13645.26
5.	NH15-L04e	16339.64	14637.04
6.	NH15-L04d	14666.04	39734.06
7.	NH15-L03a	8995.31	16473.40
8.	NH15-L03c	5963.91	22603.15
9.	NH15-L05b	5952.00	24155.31
10.	NH15-L06b	4333.53	4433.13
11.	NH15-L13b	3488.79	4167.04
12.	NH15-L20a	3650.07	37024.14
13.	NH15-L05a	2471.53	16483.58
14.	NH15-L05c	1782.91	27150.89
15.	NH15-L03d	1294.37	33763.90
16.	NH15-L20b	1104.84	34899.00
17.	NH15-L06a	667.98	36712.77

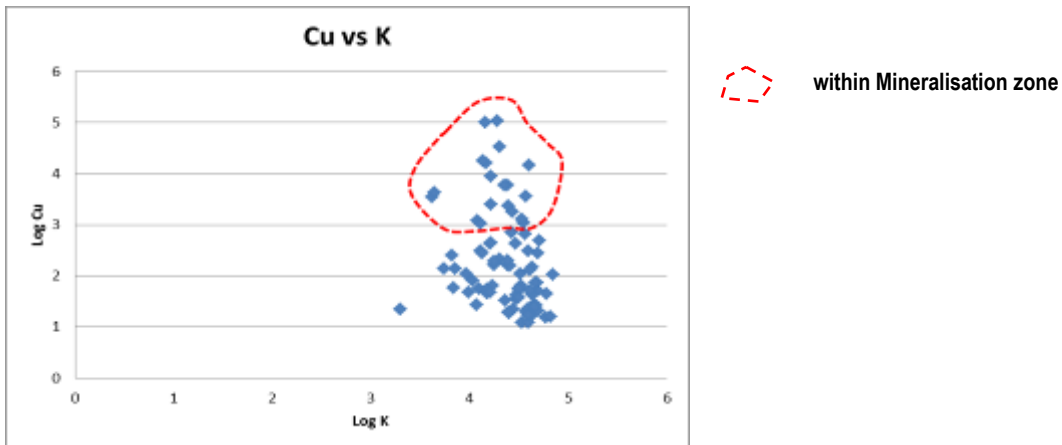


Figure 33. A log plot of Cu vs K concentrations showing all samples within the mineralisation zone.

The concentration of the Cu as measured in the Haib for this research was plotted with graduated circles using ~0.25% as the mean concentration value; this resulted in highlighting the mineralised zone as demarcated from the Volstruis creek (Figure 34a). K was also plotted and its concentration tends to extend outside the mineralised zone in the study area (Figure 34b).

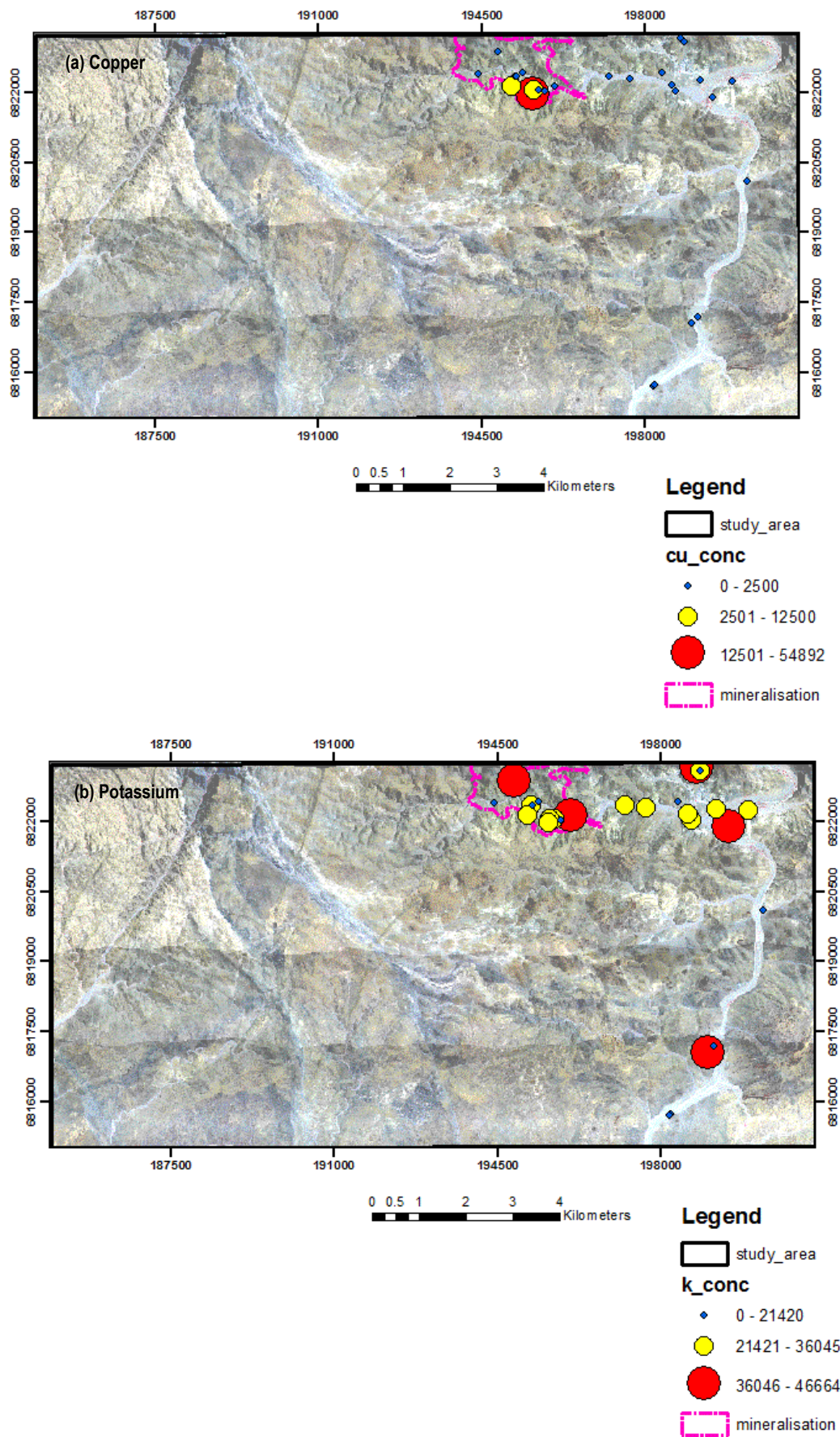


Figure 34. XRF Concentration plot using graduated circles (a) for Copper (b) for Potassium.

(b) Geological structures

The influence of structures to the present state of a rock exposure cannot be underestimated. The cumulative effect of the interconnectivity of these structures can lead to changes on both the local and the regional scales. Although tracing out the orientation of most local scaled structures may not be possible from the regional point of view, the effects are observed on the regional scale (Figure 35). Joints, fractures and faults are pathways through which hydrothermal fluids interact with the mineralogy of the rock. This interaction tends to bring about mineral composition changes that can eventually produce another rock. This is reflected in the degree or extent of change which the rock has undergone. The Haib area is typically characterised by these in the form of micro-joints, micro-fractures and faults which are not detected by images (Figure 36). Field samples description are shown in Appendix IV.

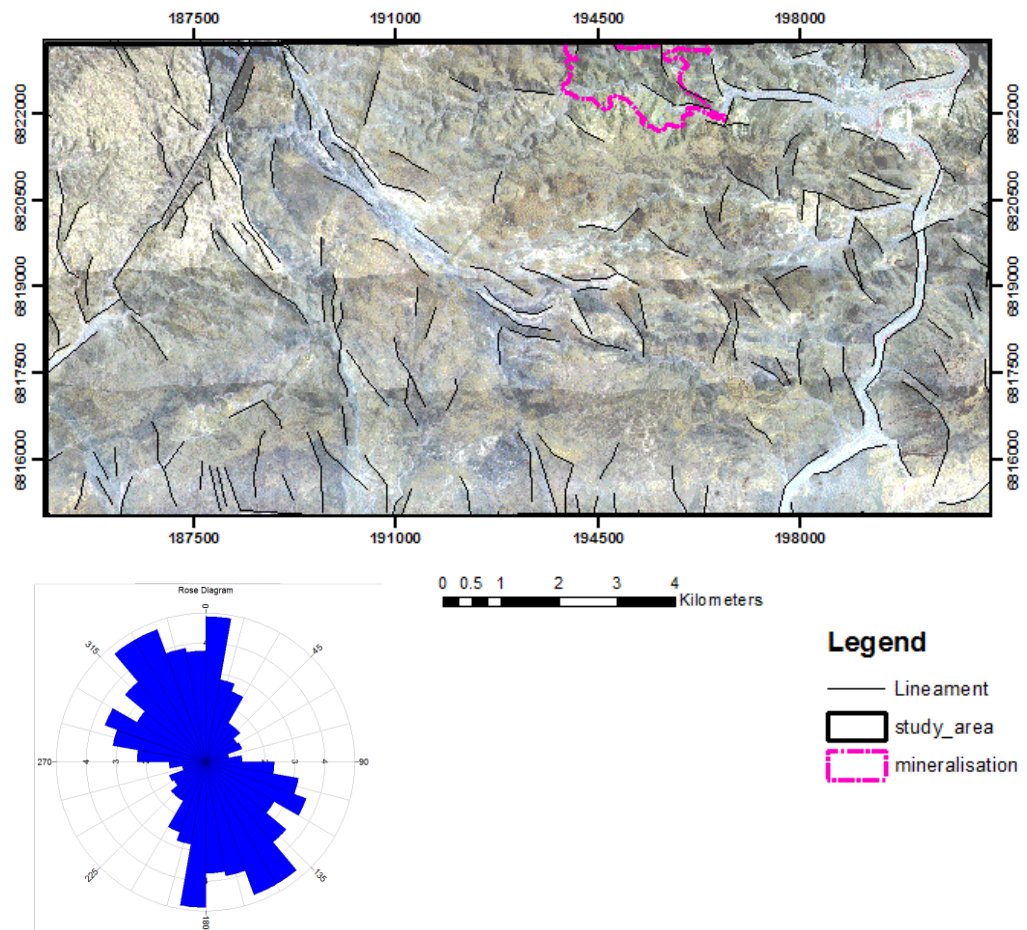


Figure 35. A rose diagram showing the dominating NW-SE structural trend in the Haib.

All sample points that exhibited alterations are closely related to the intensity of structures dissecting and cross-cutting the exposure. L01 as the first point of call displayed this variably across the rock (Figure 36a); these randomly oriented structures are closely associated with the different colouration observed in the rock phase. Ranging from creamy white at the base to yellowish red, brown and reddish brown colours, the textures of the rocks also tend to change to fine clayey materials (Figure 36d and e). The sericite alteration in the Haib has been described as having networks of interconnected fractures and joints which aid fluid transmission through rock (Minnitt, 1986).

Evidence of movement is also revealed in the fault displacement type. The dextral (Figure 36b) and sinistral (Figure 36c) fault displacements hints on the tectonic movements that once prevailed in the environment. Field sample descriptions are found in Appendix IV.

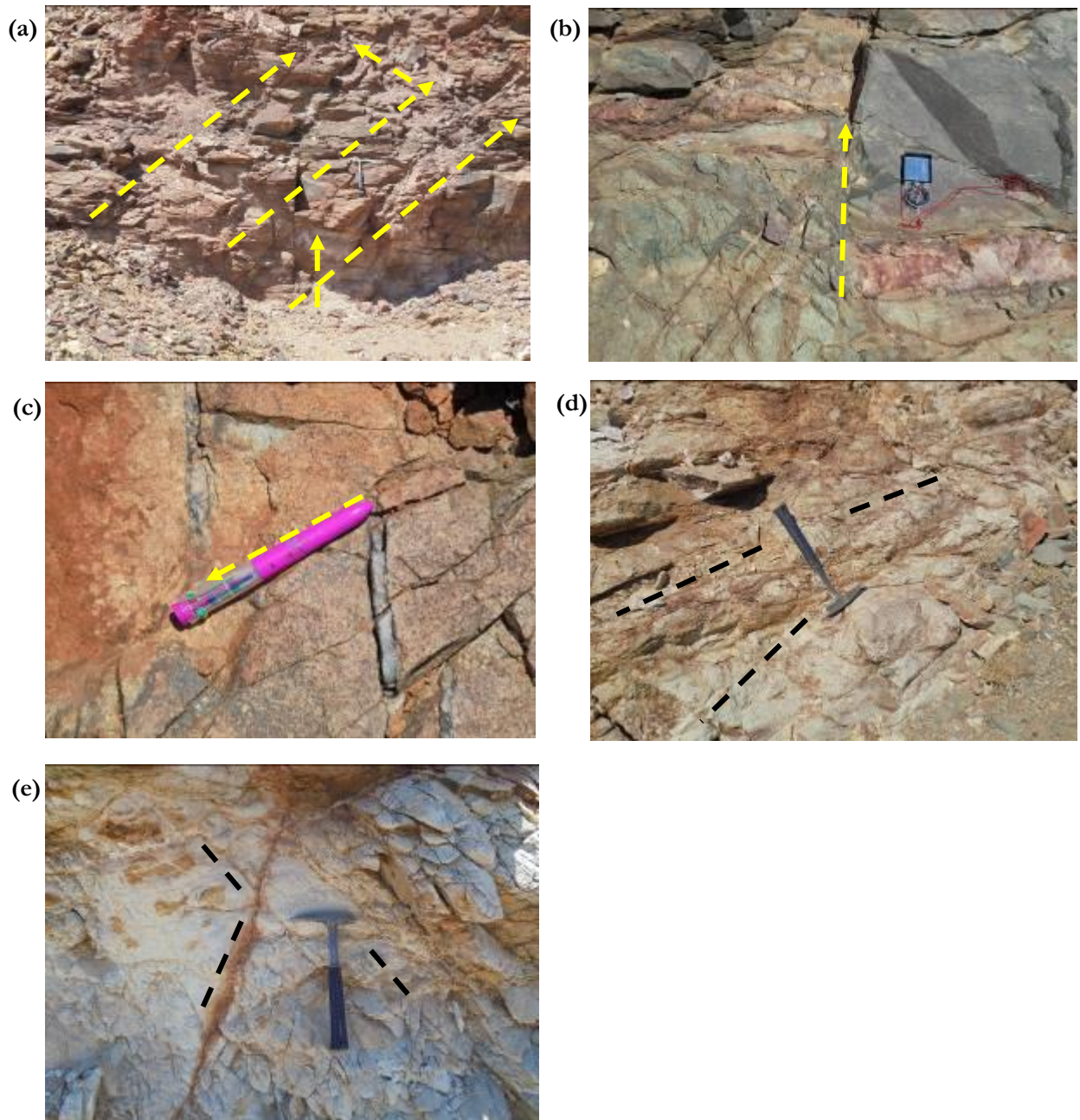


Figure 36. Geological structures and orientations (a) fractures randomly distributed with respect to alterations at L01 (b) Dextral fault displacement at L01 (c) Sinistral fault displacement at L05 (d) Jointing (healed with reddish brown minerals) at L02 (e) Fractures and joints in a sericitised rock exposure at L15.

5.3.3. Data interpretation and result synthesis

From the integration of the XRF data, the QFP rock unit was sampled and the Cu mineralisation zone was discovered through the anomaly-related concentration as found in the samples. The sample points L03, L04, L05, L06, L13 and L20 listed in table 5 all plotted within the mineralisation zone as delineated from the literature (Minnitt, 1979). Also from the K concentration plot across the geology (Figure 28), it can be inferred that using the concentration of K in detecting anomaly is impossible; this is because the average concentration values tend to overlap in all the rock units.

6. CHAPTER SIX

6.1. Validation

The validation phase of this research was conducted on the output results obtained from the remotely acquired datasets. The hyperspectral and radiometric datasets were validated with field acquired data which was carried out by ground-truthing. The rock samples collected were measured for both reflectance and geochemical data; while the measured reflectance data from the rock samples was compared with for the hyperspectral, the computational result from the geochemical (XRF) was equated with the radiometric data. This is solely to confirm the authenticity of the results.

6.2. Hyperspectral data

The reconfirmation of the calculated hypopy wavelength map led to the creation of the mineral map using the Spectral Angle Mapper (SAM) image classification method. The SAM in turn was verified with the Linear Spectral Unmixing (LSU) tool through the RMS error image which confirms the accuracy of the generated endmembers which were used as training sets. The ground reflectance data was plotted on the SAM image classification for correlation check via the sample points. With the 5-metre resolution hyperspectral image, eight (8) endmembers were well decomposed out of the image using training sets derived from the image.

From the image generated endmembers, the illite alteration minerals observed are categorised into two classes; the high and low crystallinity illites are both existing in the Haib study area. While the high crystallinity illite predominates in the sericitic alteration zone with the muscovite, the low crystallinity type is found associated with the smectite variably alongside traces of carbonate which may be affected by its coefficient of absorption.

The field spectra were compared with the HyMap alteration output. Although the number of endmembers generated from the field reflectance data was 14, there is a correlation between the two datasets. For instance, the location 1 (NH15-L01), which had four samples revealed muscovite, illite I and illite II minerals captured by the Hymap data. The location 3 which plotted close to the illite tending to Phengite also showed proximity with the smectite. The SAM classification revealed spectra features that are having surficial relevance which is because the hyperspectral sensor tends to capture what is directly on the surface of the earth. The advantage of field spectra measurement revealed some subsurface alteration patterns. The Haib field database (Appendix V) compiled the ground spectra and geochemical concentrations used for this research (Figure 37); location 2 (NH15-L02) which showed just a slightly lesser crystallinity than location 1, is of illitic composition, this also plots on illite and muscovite clusters on the image; location 5 (NH15-L05) sample which was categorised under the illite II group of the ground reflectance spectra and tagged as comprising of differential mixtures of the smectite-illite-carbonate (SIC) and illite-smectite-carbonate (ISC), with some minor chlorite plots on the illite tending to phengite (ItP) class of the SAM classification; NH15-L06 which majorly measures illite content and traces of ItP plots on ItP portion of the image; NH15-L04, also under illite II is defined as varying in composition from smectite-illite (SI) to smectite-illite-carbonate (SIC) and falls on the montmorillonite II of the image; the location 17B (NH15-L17B) displayed weak clay feature alongside pronounced water feature at 1.9 μm , which plots on the montmorillonite II and with some proximity with ItP. NH15-L03, a variety of illite II, having different degrees of SIC plots close to ItP; NH15-L09 defined by the water feature (smectite) and some weak clay features plots close to the montmorillonite II; this similar trait is also exhibited by NH15-L10 as this variation in the water and clay feature plots on the montmorillonite II region (Figure 37).

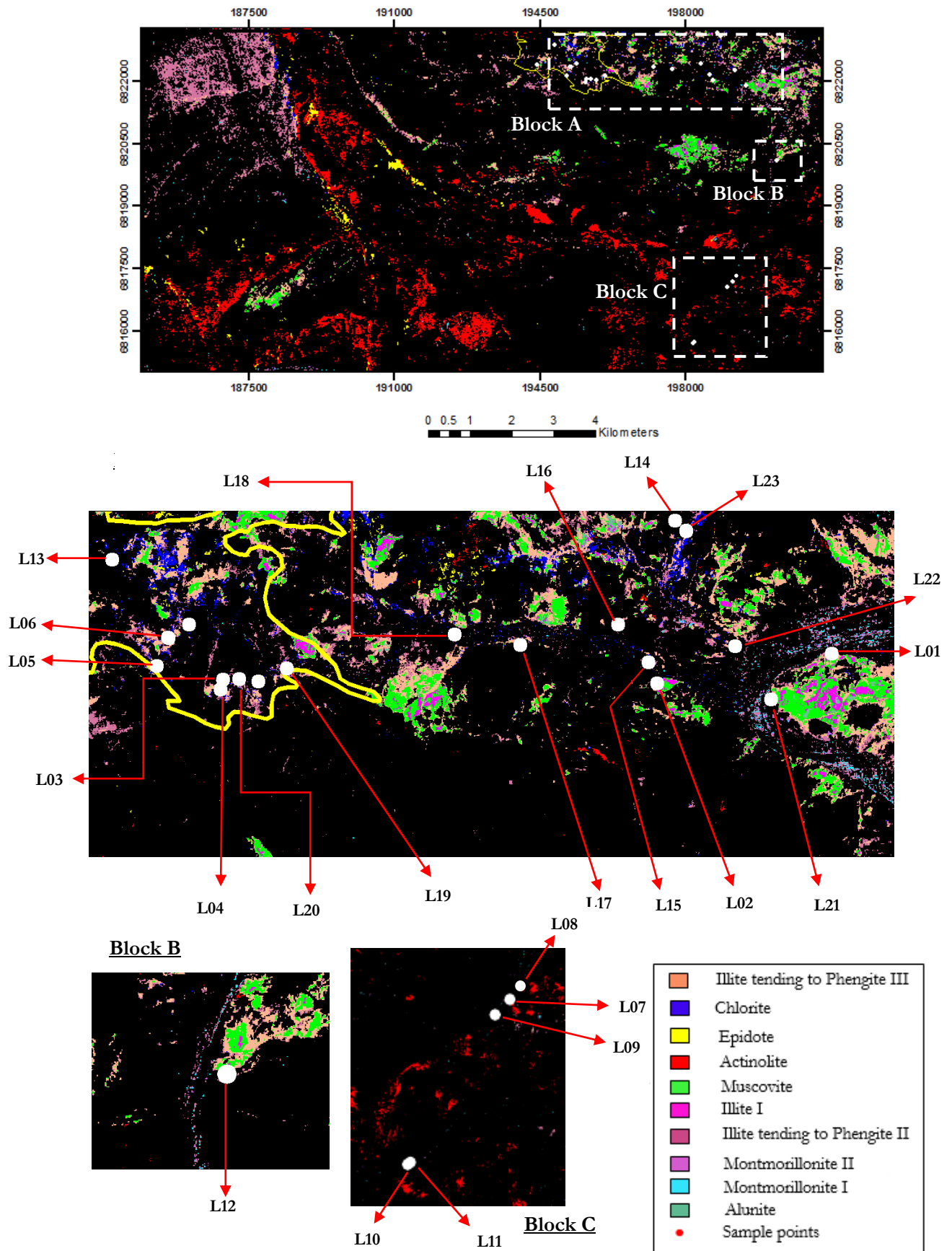


Figure 37. Field reflectance sampling points against HyMap (SAM) output.

6.3. Radiometric data

The strength of the linear relationship between the concentrations of K value acquired with the XRF scientific equipment was correlated with that obtained from the airborne gamma ray data (Figure 38). Data values measured with the XRF equipment that could not represent the K concentration relative to the signal measurement position of the airborne gamma sensor were not included in the correlation relationship. The two numerical variables produced a positive medium correlation (0.73) despite the limited sampling points used in this aspect of the research. The limitations that can be ascribed to this test is in the resolution difference between the two sensors and the sampled phase. The table 6 lists the sample locations and corresponding concentration values from the two different data sources.

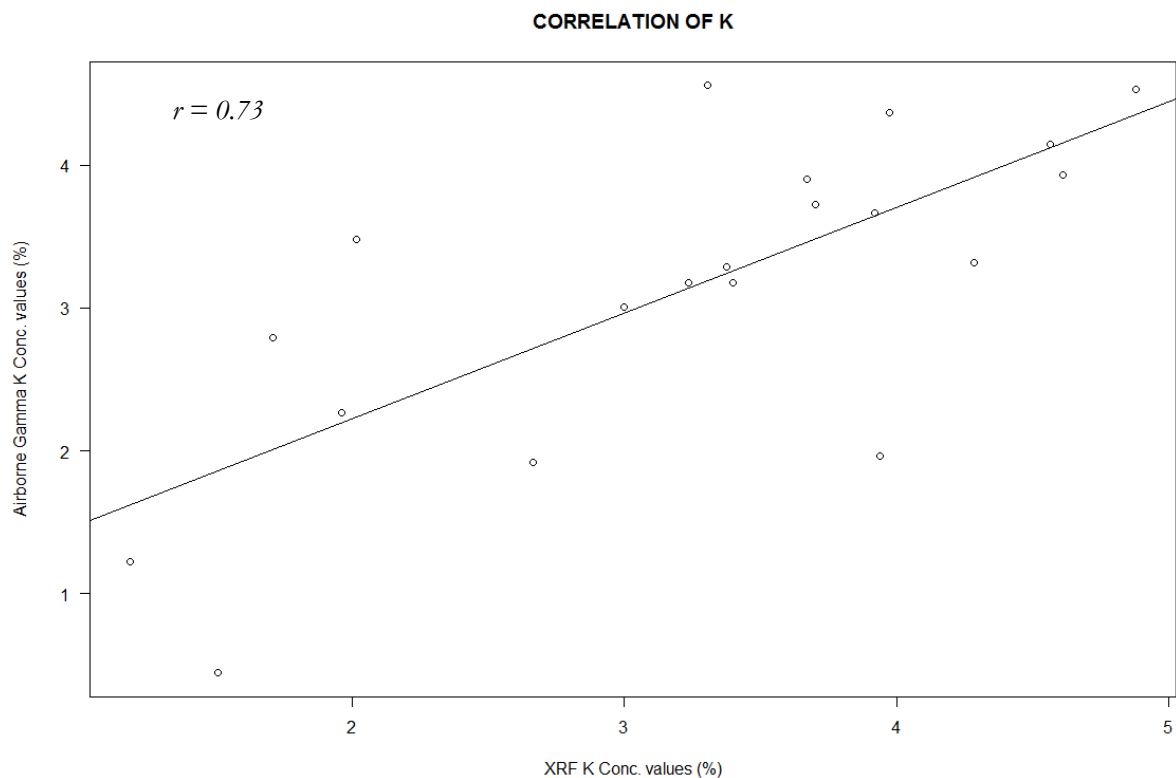


Figure 38. Graph showing the correlation relationship between the K concentration values as obtained from both the XRF and the airborne gamma ray data.

6.4. Inferences

From field observations (Figure 39a & b) and XRF laboratory results (Table 5), the Cu mineralisation detected (particularly L03 & L04) is as a result of supergene enrichment below the paleo-water table once prevalent in geologic past. The QFP rock unit is primarily rich in chalcopyrite (golden to brassy-yellow colour-like), when subjected to fracturing and meteoric water invasion, leaching takes place downward to the oxidation zone; further transportation to a reducing level below the water table to emplace the secondary Cu mineral (cyan, bluish-green or greenish coloured) as shown in figure 39. The effect of weathering is observed as playing a key role in this case to produce secondary Cu mineralisation in the Haib (Herrington et al, 2007).

Table 6. K concentration values from airborne gamma ray and XRF.

Sample no.	K_gamma(%)	K_XRF (%)
NH15-L01	1.22	1.19
NH15-L02	2.79	2.29
NH15-L13	3.32	4.28
NH15-L14	3.18	3.40
NH15-L19	4.15	4.56
NH15-L18	4.56	3.31
NH15-L21	3.67	3.92
NH15-L15	3.01	3.00
NH15-L22	1.92	2.67
NH15-L04	4.37	3.97
NH15-L23	3.18	3.24
NH15-L06	3.90	3.67
NH15-L20	5.22	2.72
NH15-L07	3.73	3.70
NH15-L17	3.48	2.02
NH15-L03	3.93	4.61
NH15-L09	3.29	3.38
NH15-L16	1.96	3.94
NH15-L10	2.27	1.96
NH15-L12	4.53	4.88

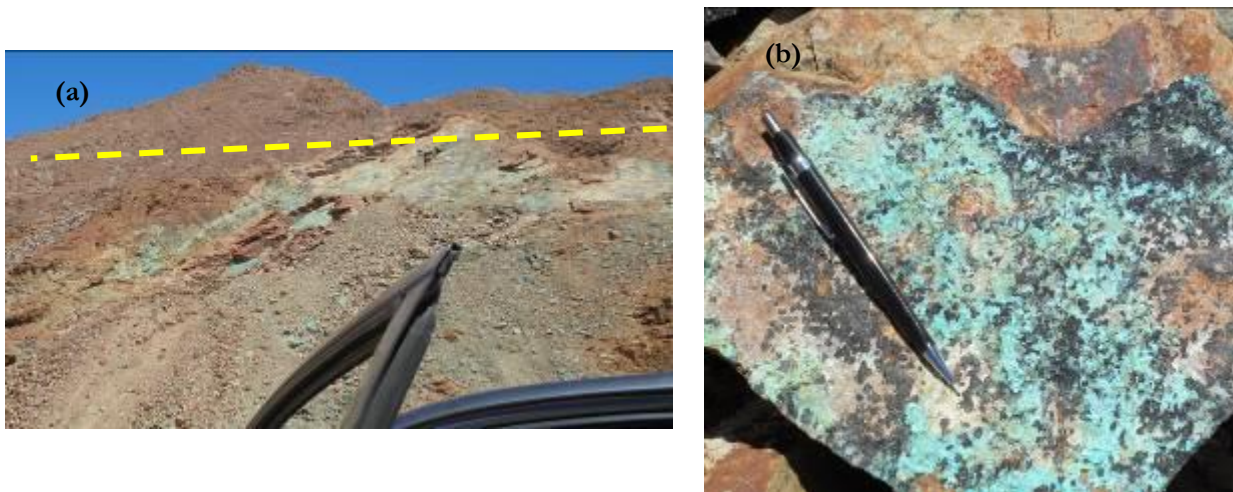


Figure 39. Field observation (a) inferred paleo-water table in yellow dash line (b) supergene Cu enrichment.

7. CHAPTER SEVEN

7.1. Discussion of results

From the analysis derived from surface geology, spectral and laboratory measurements, a new alteration model is reconstructed defined by the initiation of magmatic activity that resulted in the emplacement of the QFP unit (Figure 40); this unit is accompanied by disseminated Cu mineralisation which on subjection to leaching through fractures and water infiltration produced the secondary Cu mineralisation below the paleo-water table; this is confirmed by the incorporation of water feature as detected via ground reflectance spectra (illite II and smectite group minerals); the complex setting also reveals the influence of convective fluid circulation that contributed to the sericitic alteration which is at a much higher temperature compared to the argillic alteration that is closer to the secondary mineralisation; the second magma chamber was proposed just to highlight proximity to a more direct heat source to drive the influencing fluid and putting the effects of structural features into consideration such as faults, fractures, etc; it was noted that the sericitic alteration is more pronounced in the LFP unit compared to the QFP; the intervention of the propylitic alteration minerals in the form of epidote and chlorite further reveals the differentiation of the present alteration pattern from the Lowell and Guilbert model.

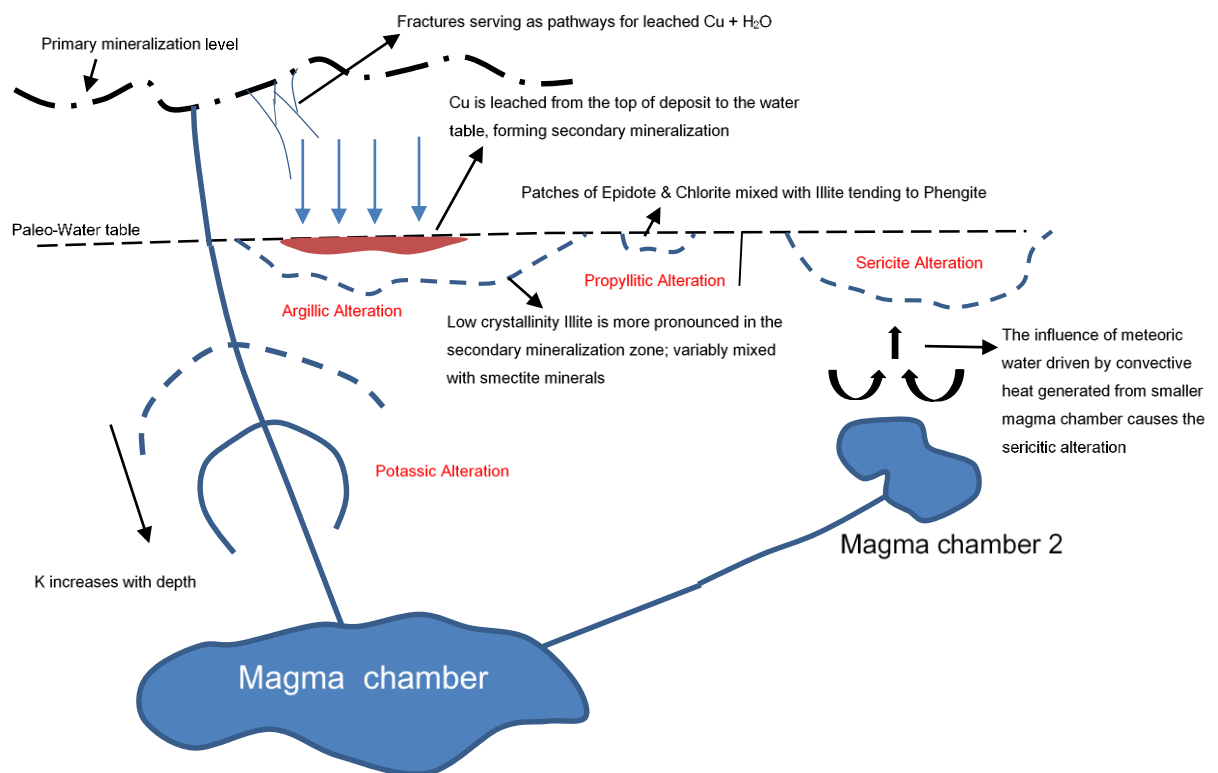


Figure 40. The newly reconstructed alteration model of the Haib study area.

7.2. Conclusions

In line with the research questions outlined in chapter one of this report, the inferences that can be deduced are as follows:

- The hyperspectral dataset was used to distinctly extract the minerals associated with the porphyry copper deposit in the Haib; although eight (8) classes of endmembers were listed for the HyMap (Chapter 4, page 26-28), the field reflectance data revealed fourteen (14) endmembers based on

scale and phase of sampling; most of the samples associated with the Cu mineralisation are also mixed with the low crystallinity illite (illite II); while illite I is more pronounced in the sericitic alteration zone than in the Cu mineralisation (Chapter 4, pages 32-33).

- The alteration minerals are now complexly mixed and zoned, hence not actually complying with the Lowell and Guilbert model; the potassic alteration that characterises the central core of the Lowell and Guilbert model was not discovered on the surface during this research; it is inferred as increasing with depth as documented in literature (Chapter 7, page 58).
- The geology characterizing the study area yielded different alteration mineral combinations due to the mineralogical composition of the rock (Chapter 4, pages 29-31); the radiometric data was not able to delineate an anomaly in the area because of the pervasive concentration of K in the rock units; the average range in K concentration tend to overlap in all the rocks (Chapter 5, pages 44-45). The XRF measurement brought out Cu anomaly-related values based on its excessively high concentration coincidentally within the delineated mineralisation regions; the L04 Cu value vary from 3.3% to above 10% which is suspected to be higher than the low grade type Cu mineralisation, hence tagged as a secondary Cu mineralisation zone; the infiltration of water down fractures in the QFP host rock seems like the only process that resulted in the formation of this secondary mineralisation below the inferred paleo-water table; most of the sampling points (L03, L04, L05, L06 and L13) associated with the Cu mineralisation have undergone alteration to smectite minerals, complexly mixed with illite and carbonate minerals. The argillic alteration zone is proximal to Cu secondary mineralisation in study area.
- The radioelement K measured in the laboratory was related with the alteration minerals mapped with the field spectra (Chapter 4, pages 36-39). The parameters of absorption features are put into consideration when producing the mineral maps, which is as a result of the interaction of a rock unit with hydrothermal fluid; while the radiometric data relies on the elemental composition in relation to the rock (Chapter 4, page 40).
- The entire area displayed complexly dissecting geological structures both on a macro and micro scales, hence suspected to be of significant influence during the alteration process (Chapter 5, page 51).
- An extent of metamorphism was detected from the mineral assemblage. The epidote, chlorite and actinolite detected classify the terrane to have undergone low to medium metamorphism (Chapter 4, page 40).

7.3. Recommendations

The restriction of the six (6) research questions posed in this work to a fifty-page document is a limitation to the volume of information that can be made available via this report. In other words, more work can still be done to further advance knowledge on the Haib porphyry copper deposit. The foundation to this starts from the proper planning for the field work phase which should include earmarking substantial duration for data collection. This can forestall the limitation of inaccessibility to some extent. More structural data can still be captured to further understand the trend relationship with respect to geological timing. The integration of another dimension to the already acquired surface information by using borehole data is advisable. Spectral data measurement of drill cores can be carried out. This is to adequately acquire enough information and data that will enhance data interpretation. Any algorithm output image should be draped over the geology of the study area for consistency check. Laboratory experiments such as fluid inclusions study and detailed petrographic analysis can also flavour this work.

LIST OF REFERENCES

- Aleks, K., & Oliver, S. (2004). ASTER Mineral Index Processing Manual. Remote Sensing Applications Geoscience Australia, (October 2004).
- ASTER. (2001). Land Processes Distributed Active Archive Center (LP DAAC), 2001, ASTER Level 1B Registered Radiance at the Sensor. Version 3. NASA. EOSDIS Land Processes DAAC, USGS Earth Resources Observation and Science (EROS) Center.
- Bakker, W. H., Ruitenbeek, F. J. A. van, & van der Werff, H. M. A. (2011). Hyperspectral image mapping by automatic color coding of absorption features. In 7th EARSeL Workshop of the Special Interest Group in Imaging Spectroscopy, 11-13th April 2011, Edinburgh (pp. 56 – 57).
- Barr, J.M. & Reid, D. L. (1993). Hydrothermal alteration at the Haib porphyry copper deposit, Namibia: Stable isotope and fluid inclusion patterns. *Communs Geol. Surv. Namibia*, 8, pp. 23–35.
- Baskaran, M. (2011). Handbook of Environmental Isotope Geochemistry, *Advances in Isotope Geochemistry*. Springer Berlin Heidelberg.
- Bea, F. (1999). Uranium. In *Encyclopedia of Geochemistry*, Marshall, C.P and Fairbridge, R.W. (editors), (Kluwer Academic Publishers, London), 712.
- Beane & Bodnar. (1995). Hydrothermal Fluids and Hydrothermal Alteration in Porphyry Copper Deposits. In Pierce, F. W. and Bohm, J.G., *Porphyry Copper Deposits of the American Cordillera Arizona Geological Society Digest 20*, Tucson, AZ, pp. 83–93.
- Beane, R. E., & Bodnar, R. J. (1995). Hydrothermal fluids and hydrothermal alteration in porphyry copper deposits. *Arizona Geological Society Digest*.
- Berger, B.R., Ayuso, R.A., Wynn, J.C., Seal, R. R. (2008). Preliminary model of porphyry copper deposits. United States Geological Survey (USGS) open File Report 2008-1321.
- Berry, L. G., Mason, B., & Dietrich, R. V. (2004). *Mineralogy: Concepts, Descriptions, Determinations* (Second.). CBS Publishers.
- Darnley, A. G. (1996). “Uranium exploration data and global geochemical baselines: The need for coordinated action,” In *Uranium Exploration Data and Techniques Applied to the Preparation of Radioelement Maps*. IAEA-TECDOC-980, IAEA, Vienna.
- De Villiers, J. and Sohnge, P. G. (1975). The geology of the Richtersveld, 48, pp. 295.
- Dickson, B. L., & Scott, K. M. (1997). Interpretation of aerial gamma-ray surveys - adding the geochemical factors. *AGSO Journal of Australian Geology and Geophysics*, 17(2), pp. 187–200.
- Eglinton, B. M. (2006). Evolution of the Namaqua-Natal Belt, southern Africa - A geochronological and isotope geochemical review. *Journal of African Earth Sciences*, 46(1-2), pp. 93–111.
- Gong, P., & Zhang, A. (1999). Noise Effect on Linear Spectral Unmixing. *Annals of GIS*, 5, pp. 52–57.
- Guilbert, J.M., Park, C. P. (1986). *The geology of ore deposits*. W. H. Freeman, New York.
- Herrington, R., Boni, M., Skarpelis, N., & Large, D. (2007). Palaeoclimate, weathering and ore deposits—a European perspective. *Proceedings of the Ninth Biennial SGA Meeting*.
- Holliday, J. R., & Cooke, D. R. (2007). Advances in Geological Models and Exploration Methods for Copper ± Gold Porphyry Deposits. *Proceedings of Exploration 07: Fifth Decennial International Conference on Mineral Exploration*, pp. 791–809.
- IAEA. (2003). Guidelines for radioelement mapping using gamma ray spectrometry data, IAEA-TECDOC-1363, Vienna-Austria., (July), pp. 6–7.
- John, D. A., Ayuso, R. A., Barton, M. D., Bodnar, R. J., Dilles, J. H., Gray, F., ... Vikre, P. G. (2010). Porphyry Copper Deposit Model Scientific Investigations. USGS Scientific Investigations, (Report 2010 – 5070 – B), pp. 13–14.
- Kearey, P., E. (1993). *The encyclopedia of the solid earth sciences*. Oxford, Uk, Blackwell Scientific.
- Keshava, N. (2003). A Survey of Spectral Unmixing Algorithms. *Lincoln Laboratory Journal*, 14(1), pp. 55–78.
- Kesler, S. E., & Wilkinson, B. H. (2007). Earth’s copper resources estimated from tectonic diffusion of porphyry copper deposits, pp. 255–258.
- Kruse, F. a. (1994). Imaging spectrometer data analysis. A Tutorial, 12.
- Kruse, F.A., Lefkoff, A.B., Boardman, J.W., Heidebrecht, K.B., Shapiro, A.T., Barloon, P.J., Goetz, A. F. H. (1993). The Spectral Image-Processing System (SIPS) - Interactive Visualization and Analysis of Imaging Spectrometer Data. *Remote Sens. Environ.*, 44, pp. 145–163.
- Langmuir, D. and Hermans, J. S. (1980). The mobility of thorium in natural waters at low temperatures. *Geochimica et Cosmochimica Acta*, v. 44, pp. 1753 – 1766.

- Le Bas, M. J. (2000). IUGS reclassification of the high-Mg and picritic volcanic rocks. *Journal of Petrology*, 41, pp. 1467–1470.
- Le Bas, M.J., Le Maitre, R.W., Streckeisen, A., Zanettin, B. (1986). A chemical classification of volcanic rocks based on the total alkali-silica diagram. *Journal of Petrology*, 27, pp. 745–750.
- Lusty, P. A. J., & Gunn, A. G. (2015). Challenges to global mineral resource security and options for future supply, pp. 265–276.
- Meer, F. Van Der, & Jong, S. De. (2003). Spectral Mapping Methods : Many Problems, Some Solutions, (May), 13–16, pp. 146 - 162.
- Middlemost, E. A. K. (1985). *Magma and magmatic rocks: An introduction to igneous petrology*. London, UK, Longman, 266 p.
- Mielke, C., Rogass, C., Boesche, N., Segl, K., & Altenberger, U. (2016). EnGeoMAP 2.0—Automated Hyperspectral Mineral Identification for the German EnMAP Space Mission. *Remote Sensing*, 8(2), 127.
- Minnitt, R. C. A. (1979). The geological setting of the porphyry copper mineralization in the Haib River area, South West Africa (Ph.D.). Univ. Witwatersrand, Johannesburg.
- Minnitt, R. C. A. (1986). *Porphyry Copper-Molybdenum Mineralization at Haib River, South West Africa/Namibia*. Geological Society of South Africa, Johannesburg.
- Minty, B. R. S., Luyendyk, A. P. J., & Brodie, R. C. (1997). Calibration and data processing for airborne gamma-ray spectrometry. *Journal of Australian Geology & Geophysics*, 17(2), pp. 51–62.
- Nironen, M., & Csongradi, J. (1984). Characteristics of the Proterozoic porphyry-type Cu occurrence at Tienpaa, Halsua, western Finland. *Bulletin of the Geological Society of Finland*, 56(1-2), pp. 89–97.
- Patrick, R. A. D. (1993). *Ore Geology and Industrial Minerals*, third edition, by A. H. Evans. Blackwell Scientific, Oxford. (A. H. Evans, Ed.) *Geological Journal* (Third., Vol. 29). Blackwell Scientific.
- Pirajno, F. (2008). *Hydrothermal Processes and Mineral Systems*, 1282.
- Reid, D. L. (1977). Geochemistry of Precambrian igneous rocks in the lower Orange River Region. *Bull. Precamb. Res. Unit. Univ. Cape Town*, 22, 397 pp.
- Reid, D. L. (1979). Total-rock Rb-Sr and U-Th-Pb isotopic study of the Precambrian metavolcanic rocks in the lower Orange River region, southern Africa, 42, pp. 368 – 378.
- Reid, D. L. (1982). Age relationships within the Vioolsdrift batholith, lower Orange River region. II. A two-stage emplacement history and the extent of the Kibaran overprinting, 85, pp. 105 – 110.
- Richards, J.P., Noble, S.R., Pringle, M. S. (1999). A revised late Eocene age of porphyry Cu magmatism in the Escondida area, 94, pp. 1231–1247.
- Robb, L. (2009). *Introduction to Ore-Forming Processes*. Wiley.
- Rohrlach, B.D., Loucks, R. R. (2005). Multi-million-year cyclic ramp-up of volatiles in a lower crustal magma reservoir trapped below the Tampakan copper-gold deposit by Mio-pliocene crustal compression in the Southern Philippines, 2, pp. 369–407.
- Salisbury, J. W. (1998). *Spectral measurements field guide*. International Institute for Aerospace Survey and Earth Sciences, 1–91.
- Sasha. (1997). *Spectral Interpretation Field Manual G-MEX*, 1, 153.
- Sheth, H. C., Torres-Alvarado, I. S., & Verma, S. P. (2002). What Is the “Calc-alkaline Rock Series”? *International Geology Review*, 44(8), pp. 686–701.
- Sillitoe, R. H. (1993). Gold-rich porphyry copper deposits: Geological model and exploration implications (pp. 465–478). *Geological Association of Canada Special Paper* 40.
- Sillitoe, R. H. (2010). *Porphyry Copper Systems*. Society of Economic Geologists, Inc., *Economic Geology*, 105, pp. 3–41.
- Sinclair, W. D. (2007). *Porphyry Deposits*. Geological Survey of Canada, (Special Publication No. 5), pp. 223–243.
- Stein, H.J, Markey, R.J., Morgan, J.W., Hannah, J.L., Schersten, A. (2001). The remarkable Re-Os chronometer in molybdenite: how and why it works, pp. 479–486.
- Taylor, G., & Eggleton, R. A. (2001). *Regolith Geology and Geomorphology*. Wiley.
- Thomas, R. J., Agenbacht, a. L. D., Cornell, D. H., & Moore, J. M. (1994). The Kibaran of southern Africa: Tectonic evolution and metallogeny. *Ore Geology Reviews*, 9(2), pp. 131–160.
- Titley, S. R. (1982). The style and progress of mineralization and alteration in porphyry copper systems, pp. 93–116.
- Van Ruitenbeek, F. J. A., Bakker, W. H., van der Werff, H. M. A., Zegers, T. E., Oosthoek, J. H. P., Omer, Z. A., ... van der Meer, F. D. (2013). Mapping the wavelength position of deepest absorption features to explore mineral diversity in hyperspectral images. *Planetary and Space Science*, 101, pp.

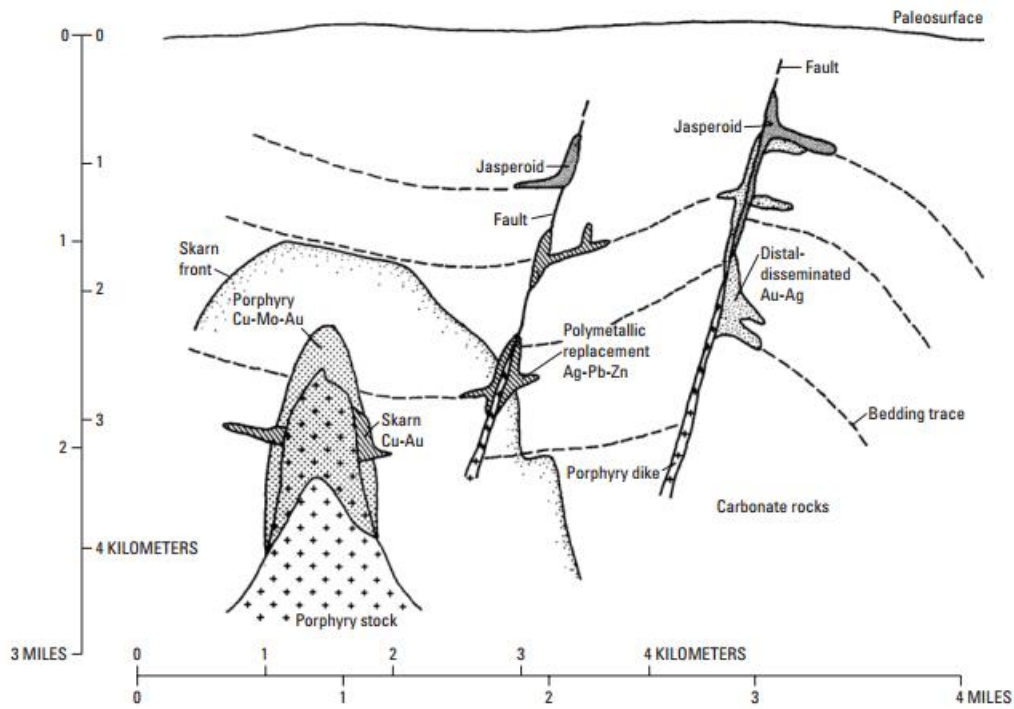
108–117.

Wilkinson, J.F. (1968). The petrography of basaltic rocks. In Hess, H. H., and Poldervaart, A., Eds., Basalts, v. 1: New York, NY, Wiley Interscience, pp. 163–214.

Wilson, M. (1996). Igneous petrogenesis (2nd ed.: L.). Chapman & Hall.

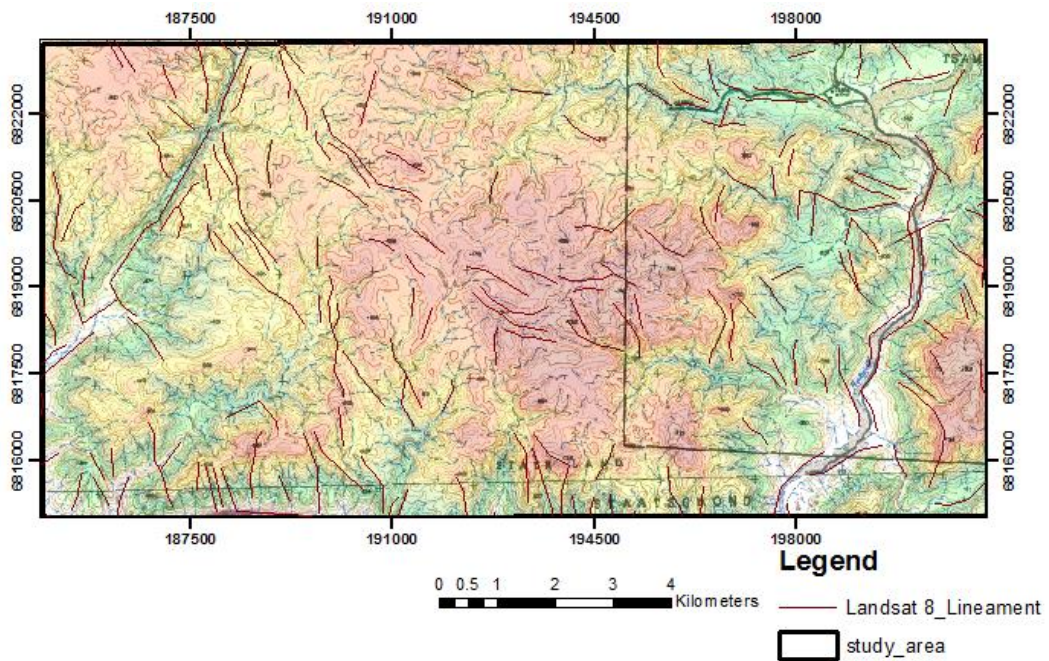
Wilson, A.J, Cooke, D.R., Stein, H.J., Fanning, C.M., Holliday, J.R., Tedder, I. J. (2007). U-Pb and Re-Os geochronologic evidence for two alkalic porphyry ore-forming events in the Cadia district, New South Wales, Australia, 102, pp. 1–26.

APPENDIX I



General setting of porphyry copper and associated deposit types (modified from Sillitoe and Bonham, 1990)

APPENDIX II



Topographic map draped with SRTM and lineament extracted from Landsat 8 imagery

APPENDIX III: Statistical summary of the airborne gamma ray radioelement concentrations

Rock unit	K_Conc. (ppm)	Th_Conc. (ppm)	U_Conc. (ppm)
QFP	1.19	10.53	3.34
QFP	5.93	35.69	24.38
QFP	2.81	30.60	20.40
QFP	5.43	7.17	-6.12
Grd	-0.46	4.20	2.64
Grd	5.98	37.19	41.92
Grd	2.42	30.20	31.10
Grd	5.65	3.60	-29.30
LFP	0.67	7.41	1.66
LFP	6.46	40.09	30.46
LFP	5.26	34.48	27.20
LFP	1.69	11.78	-5.70
UFP	1.43	8.69	-1.82
UFP	4.47	28.09	18.93
UFP	4.41	24.96	20.50
UFP	1.08	3.54	-8.40
Amp	1.09	8.85	-1.78
Amp	7.61	36.27	31.39
Amp	5.08	34.40	23.30
Amp	-0.55	6.48	-12.50
U_grnt	-0.07	2.98	1.10
U_grnt	7.59	54.86	44.53
U_grnt	5.99	48.86	26.30
U_grnt	-0.75	-12.30	-25.50
Leuco_grnt	1.03	13.47	3.56
Leuco_grnt	7.38	62.67	44.47
Leuco_grnt	6.85	68.10	33.00
Leuco_grnt	1.42	8.16	-15.00
Adamellite	0.74	10.36	0.85
Adamellite	5.45	30.24	24.27
Adamellite	5.71	31.03	21.60
Adamellite	2.48	12.89	-13.10
Hn_dio	0.93	5.22	5.80
Hn_dio	4.51	25.82	23.82
Hn_dio	3.63	23.33	22.80
Hn_dio	-1.35	-1.88	-3.20

APPENDIX IV: Haib Field Description

S/N	Sample Location Code	Description of Rock Type/Sample
1	NH15-L01A	Dark to grey, fine grained mafic volcanic at the base of the outcrop; associated with reddish stained quartz veins which exhibits a dextral displacement; Variably faulted and jointed;
2	NH15-L01B	Creamy white, brown to yellowish colouration, fine to medium grained, jointed and Sericitic.
3	NH15-L01C	Creamy white with yellowish patches and spots; Sericitic.
4	NH15-L01D	Dark to reddish colouration, fine grained; jointed; the alteration patterns in location 1 discriminates from reddish tints, brown, yellow to whitish colourations.
5	NH15-L02	Creamy white, light brown to yellowish colouration with some dark red to reddish tints, leucocratic exposure at the base of the Quartz feldspar porphyry (QFP), Joints parallel to the orientation of the QFP, Sericitic in nature
6	NH15-L03	Dark patches to green, on the medium to coarse grained granitic rock; Secondary mineralisation.
7	NH15-L04	Dark patches to greenish colouration and medium to coarse grained.
8	NH15-L05	Greenish granitic with reddish and dark patches, coarse grained; sinistral fault displacement and jointed.
9	NH15-L06	Brown, yellow, dark red, fine to medium grained and Sericitic
10	NH15-L07	Greenish on fresh side; bouldery and fragmented rock
11	NH15-L08	Greenish tinted to dark, fine to medium grained mafic rock
12	NH15-L09	Dark brown, coarse grained granitic
13	NH15-L10	Felsic and mafic, coarse grained porphyritic
14	NH15-L11	Brown to greenish, fine grained rock
15	NH15-L12	Whitish with specks of mafic minerals, fine grained texture.
16	NH15-L13	Greyish to white with reddish inclusions, fine grained and Sericitic.
17	NH15-L14A	Whitish and fine grained
18	NH15-L14B	Dark brown to green colour, glassy textured mainly altered Talc.
19	NH15-L15A	Mafic coloured, fine to medium grained
20	NH15-L15B	Grey, white to reddish shades, medium grained
21	NH15-L16A	Reddish to greyish, fine to medium grained, quartzitic
22	NH15-L16B	Reddish to white with some inclusions of brown mineralisation, medium grained and quartzitic
23	NH15-L17A	Greyish with pinkish and greenish brown, medium grained
24	NH15-L17B	Dark brown to pinkish, medium grained
25	NH15-L18	Whitish with yellowish to dark brown colouration, fine to medium grained and Sericitic
26	NH15-L19	Whitish fine to medium grained with greyish tints
27	NH15-L20	Grey to dark, surgary with specks of golden mineralisation
28	NH15-L21A	Whitish to greyish, fine grained
29	NH15-L21B	Reddish to dark red, fine grained
30	NH15-L22	Whitish to reddish with dark inclusions and Sericitic
31	NH15-L23	Reddish to dark brown, fine to medium grained

APPENDIX V: Haib Field Spectra and Geochemical Database

Reading No.	Location Code	Wavelength	Alteration Mineral	K (ppm)	Cu (ppm)	Th (ppm)	U (ppm)	Fe (ppm)
361	L1A	2.2035	Muscovite + Silica (Water)	6905.39	58.17	11.14	10.31	46519.38
362	L1A	2.2035	Muscovite + Silica (Water)	7122.95	135.68	10		52164.4
363	L1A	2.2035	Muscovite + Silica (Water)					
364	L1A	2.2035	Muscovite + Silica (Water)					
365	L1B			57610.4		18.05	18.2	13273.42
366	L1B	2.201	Illite I	59683	15.38	26.95	15.97	11117.83
367	L1B	2.1987	Illite I					
368	L1B	2.1987	Illite I					
369	L1B	2.1987	Illite I					
370	L1C	2.1963	Illite I	37310.5	20.07			67790.2
371	L1C	2.1963	Illite I					
372	L1C	2.1987	Illite II_IS					
373	L1C	2.1963	Illite II_IS					
374	L1D	2.2035	Illite I	9773.95	47.71	28.32	14.93	67035.37
375	L1D	2.2035	Illite I	9291.34	109.13	29.59	10.38	117720.3
376	L1D	2.2035	Illite I	11856.54	27.16	43.12	10	38511.04
377	L1D	2.2035	Illite I					
378	L1D							
379	L1D	2.2035	Illite II_ISC					
380	L2	2.1987	Illite I	22908.9	33.14	11.55		5326.15
381	L2	2.1963	Illite I	17105.38	64.25	18.71		12445.74
382	L2	2.1963	Illite I	43568.76	17.5	16.84		5409.78
383	L2	2.1963	Illite I					
384	L2	2.1963	Illite I					
385	L2	2.1963	Illite I					
386	L3	1.907	SIC	16473.4	8995.31	21.96	14.92	51397.59
387	L3	1.913	SIC	13645.26	17854.59		22.24	66395.02

388	L3	1.905	SCI		22603.15	5963.91	11.24	12.64	20670.38
389	L3	1.908	SCI		33763.9	1294.37			13371.33
390	L3	1.91	SIC						
391	L3	1.907	SCI						
392	L3								
393	L3	1.905	SIC						
394	L4	1.907	SI		20192.07	33411.81	20.95	10	9631.36
395	L4	1.907	SI		14435.01	102447.1		16.69	22733.12
396	L4	1.905	SIC		18947.37	107593.7		12.32	14421.15
397	L4	2.208	Ilite II_ICS		39734.06	14666.04	26.88	14.2	56555.29
398	L4	1.908	SIC		14637.04	16339.64	30.69	10.64	51831.87
399	L4	1.905	SCI						
400	L4	1.908	SCI						
401	L4	1.908	SIC						
402	L5				16483.58	2471.53		16.85	68774.13
403	L5				24155.31	5952	12.65		96471.4
404	L5	1.927	SIC		27150.89	1782.91	15.68	12.37	15292.37
405	L5	2.216	Ilite II_ICS						
406	L5	2.213	Ilite II_ICS						
407	L5	2.213	Ilite II_ICS						
408	L6A	2.213	Ilite II_ICS		24686.61	2311.51	10.18	11.67	49428.74
409	L6A	2.213	Ilite II_ICS		51115.73	484.54	11.33	18.64	10410.63
410	L6A	2.213	Ilite II_ICS		36712.77	667.98		10.15	12677.04
411	L6A	2.213	Ilite II_ICS						
412	L6A	1.905	Ilite II_IrP						
413	L6B	1.916	Ilite II_IrP		4433.13	4333.53	10.19		249417.3
414	L6B	1.913	SIC		29089.68	425.14	11.33	11.07	14066.06
415	L6B	1.908	Ilite II_IrP						
416	L6B	1.908	Ilite II_IrP						
417	L6B	1.905	Ilite II_IrP						

418	L7	2.323	Mg Chlorite	20154.93	212.19			70938.78
419	L7	2.316	Mg Chlorite	6670.69	254.62			100098.5
420	L7	2.323	Mg Chlorite					
421	L7	2.323	Mg Chlorite					
422	L7	2.323	Mg Chlorite					
423	L7	2.302	Mg Chlorite					
424	L7	2.33	Mg Chlorite					
425	L8	2.33	Mg-Fe Chlorite	13370.67	280.26			65202.5
426	L8	2.34	Mg-Fe Chlorite	17650.81	189.49			69725.84
427	L8	2.34	Mg-Fe Chlorite					
428	L8	2.33	Mg-Fe Chlorite					
429	L9			40680.13	127.81	10.73		15805.64
430	L9	2.216	Illite II蒋CS	40628.87	50.3	10	12.95	14713.8
431	L9			39409.42	16.71		10.74	17075.93
432	L9	2.213	Illite II蒋CS					
433	L9							
434	L10	2.341	ClS	15067.09	53.57			56543.32
435	L10	2.345	ClS	24063.53	201.66			65477.13
436	L10	2.34	ClS	16162.16	46.99			29346.05
437	L10							
438	L10							
439	L11	2.334	Epidote	31355.3	38.11			84152.93
440	L11	2.337	Epidote	10809.02	81.16			55494.51
441	L11	2.337	Epidote					
442	L11	2.337	Epidote					
443	L11	2.337	Epidote					
444	L11	2.33	Epidote					
445	L11	2.33	Epidote					
446	L12	1.913	Illite II蒋IP	12397.05	57	32.14	12.43	2208.26
447	L12	2.21	Illite II蒋CS	48805.05	49.94	34.73	11.18	4512.35

478	L15B	2.2011	Ilite II_IS	30006.38	35.15	10.77	12.33	22903.86
479	L15B	2.2011	Ilite II_IS	24712.59	19.41	10.95	14.02	15022.19
480	L15B	2.2011	Ilite II_IS	39611.6	22.81		13.04	52458.04
481	L15B	2.2011	Ilite II_IS					
482	L15B	2.2011	Ilite II_IS					
483	L15B	2.2011	Ilite II_IS					
484	L15B	2.2011	Ilite II_IS					
485	L16B	2.263	Jarosite					
486	L16B	2.263	Jarosite					
487	L16B	2.263	Jarosite					
488	L16B	2.263	Jarosite					
489	L16B	2.263	Jarosite					
490	L16B							
491	L16B	2.263	Jarosite					
492	L16A	2.268	Jarosite	19624.49				66597.63
493	L16A	2.261	Jarosite	1963.49	21.95			3089.11
494	L16A	2.263	Jarosite	6295.93				16176.41
495	L16A	2.263	Jarosite	2520.64				7573.89
496	L16A							
497	L17A	2.204	Ilite II_IS	29803.38	42.2	14.5	10.05	147544.7
498	L17A	2.201	Ilite II_IS	31200.13	56.76		12.24	28032.37
499	L17A	2.201	Ilite II_IS	46116.12	72.79	13.76	17.76	46073.3
500	L17A	2.1987	Ilite II_IS					
501	L17A	2.201	Ilite II_IS					
502	L17A	2.201	Ilite II_IS					
503	L17A	2.1987	Ilite II_IS					
504	L17B			16034.52	435.05	27.65		77757.16
505	L17B			5546.8	136.92	12.11		25601.72
506	L17B			17681.49	162.43	19.65	10.48	60096.38
507	L17B							

538	L21B	1.93	SI		12857.56	311.57	105.83		660008.8
539	L21B	2.206	Illite II_IS		45490.86	24.12		12.87	17237.5
540	L21B	2.2035	Illite II_IS		43198.79	43.29	13.44	14.01	16547.68
541	L21B	2.2035	Illite II_IS						
542	L21B	2.2035	Illite I						
543	L21B	2.206	Illite I						
544	L21B	2.2035	Illite I						
545	L21B	2.206	Illite I						
546	L21B	2.2035	Illite I						
547	L22	2.2011	Muscovite + Silica (Water)		26651.05	712.7	32.71	12.97	171032.8
548	L22	2.2011	Illite II_IS		39195.63	311.75	21.88	17.16	75948.91
549	L22	2.2011	Illite I		32197.95	51.67	25.26	16.84	11479.07
550	L22	2.2011	Illite I						
551	L22	2.1987	Illite I						
552	L22	2.1987	Illite I						
553	L22	1.94	SI						
554	L22	2.1963	Illite II_IS						
555	L23	2.208	Illite II_ISC		48435.46	73.26	10.5	13.27	52895.38
556	L23	2.208	Illite II_ISC		32374.06	109.31	10	10.67	21844.14
557	L23	2.208	Illite II_ISC		11999.04	1205.09	395.01	36.78	211357.9
558	L23	2.208	Illite II_ISC		12930.92	1040.5	71.38	44.92	153610.8
559	L23								
560	L23	2.208	Illite II_IS						
561	L23	2.213	Illite II_IS						
562	L23	2.208	Illite II_IS						